Title	Investigation of implosion stability with x-ray spectroscopic method
Author(s)	Fujita, Kazuhisa
Citation	大阪大学, 1998, 博士論文
Version Type	VoR
URL	https://doi.org/10.11501/3143932
rights	
Note	

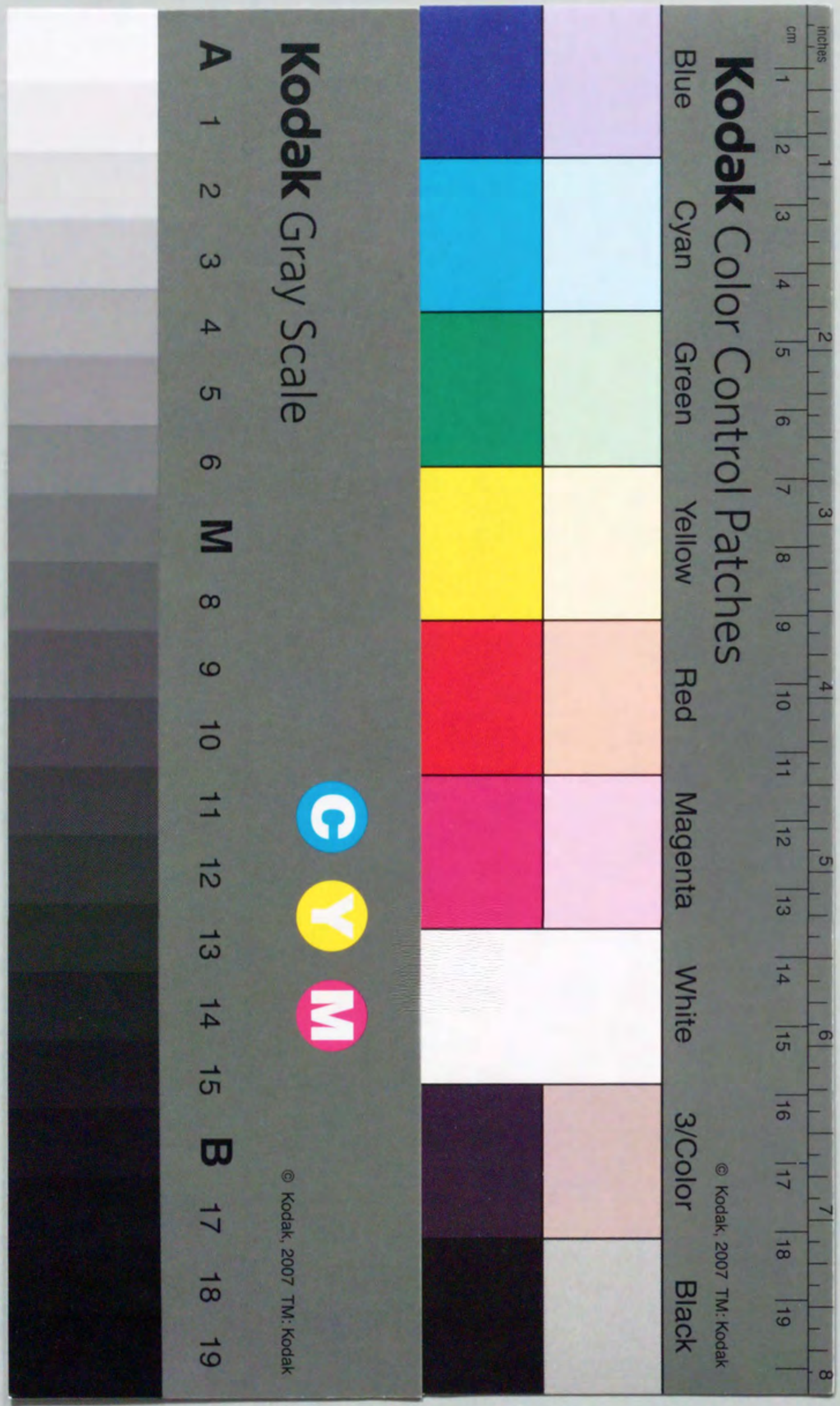

Investigation of implosion stability with x-ray spectroscopic method

（X線分光法による爆縮安定性の研究）

January 1998

Kazuhisa Fujita

①

Investigation of implosion stability with x-ray spectroscopic method

（X線分光法による爆縮安定性の研究）

January 1998

Kazuhisa Fujita

内容梗概

本論文は筆者が大阪大学大学院工学研究科電気工学専攻博士課程在学中に大阪大学レーザー核融合研究センターにて行った、「X線分光法による爆縮安定性の研究」についてまとめたものである。

レーザー核融合における点火・燃焼の実証に向けての研究は、過去２０年以上に渡り実験・理論の両面から精力的に行われてきた。その点火方式として最も研究が進んでいるのが、中心点火方式である。球状の核融合燃料ペレットをレーザー照射により発生するアブレーション圧力を用いて均一に圧縮する。このとき中心に高温部（ホットスパーク）を形成して核融合点火を行い、それを取り巻く低温の高密度部（主燃料）を燃焼させ、高利得を得るものである。主燃料の高密度圧縮はすでに実証されており、残る課題はホットスパークの加熱である。

ホットスパークの加熱の成否は、圧縮の不均一性に大きく依存する。したがって、均一圧縮を実現するための高真球度ペレット製作技術やレーザー均一照射技術の開発が進められてきた。さらに圧縮の不均一性を増大させる流体力学的不安定性に関しても、特にその安定化機構を中心として近年大幅に理解が進んでいる。ここで重要なことは、均一圧縮（＝安定した爆縮）に必要な技術開発に並行して爆縮物理の理解を進め、これらの不均一圧縮の要因とホットスパーク加熱の定量的関係を把握し、点火、燃焼、高利得設計に反映させることである。故に、爆縮の安定性診断の手段として、ホットスパークが時間的、空間的にどのように加熱されているかを実験的に観測することが必要となる。

筆者が着目したのは、X線分光法によるホットスパークの診断である。不均一圧縮の際にホットスパークと主燃料が混合(mixing)し、ホットスパークの加熱が妨げられる問題が重要視されていることから、これら両者を分離した診断が容易なX線分光法を選択した。また、従来ホットスパーク加熱の達成度の指数として、核融合反応中性子の発生数やそのスペクトルから得たイオン温度、燃料面密度、及び空間・時間積分されたX線スペクトルより得た電子温度・密度があったが、いずれも加熱のダイナミクスを知るには不十分であった。そこで筆者はスペクトル分解に加え、空間・時間分解能を持たせることのできるユニークな方法をレーザー核融合プラズマの診断に初めて導入した。これがX線モノクロカメラの開発である。このカメラを爆縮実験に導入し、ホットスパーク部と主燃料部を分離した２次元空間分解像の取得に初めて成功した。あわせてスペクトルの時間変化にも注目し、ホットスパークの加熱、冷却のダイナミクスに関して新たな知見を得るに至った。

本論文（英語）は６章から構成されている。

第１章はIntroductionであり、レーザー核融合研究の目的、原理、及び現状と課題に触れ、本研究の目的、意義を明らかにしている。中心点火方式においてはホットスパークと主燃料の安定形成が必要であり、これらを分離する診断法としてX線分光法が有効であることを述べる。

第２章では、X線分光法を用いた爆縮プラズマ診断の原理を述べている。プラズマを衝突・輻射平衡状態にあると仮定し、ホットスパーク部に微量ドープしているアルゴンの発光スペクトルの温度・密度依存性を得て、ホットスパーク診断への利用の可能性を示す。さらに、流体輻射シミュレーションコードを用いてホットスパーク部のアルゴン発光強度の空間・時間変化を予測する。これを実験的に観測することが、温度・密度の空間分布が時間的に変化するホットスパークのダイナミクスの解明に有効であることを述べる。

第３章では、X線分光法を利用したホットスパーク及び主燃料の診断に用いる計測器とその開発について述べる。ホットスパークの加熱のダイナミクスを知るには、スペクトル・空間・時間分解能を同時に合わせ持つ計測器が必要であることに触れる。これを実現するのが、今回開発したトロイダル湾曲完全結晶を用いたX線モノクロカメラであり、その原理、特長、設計、及び性能を明らかにする。また、後の爆縮実験でも用いているスペクトルの時間変化計測が可能なX線分光ストリークカメラの構成、性能についても述べる。

第４章では、開発したX線モノクロカメラを用いた２つのデモ実験に関して述べ、カメラの爆縮実験への適用が実証されたことを示す。１つ目は、ホットスパークの２種の単色X線画像、及びこれらの強度比分布から得た電子温度分布について述べる。得られた結果が他の同時に計測されたデータと矛盾がないことを示し、本計測法の妥当性を明らかにする。さらに、得られた結果は時間積分値であるものの、シミュレーションとの比較により減速相開始時までの圧縮が実現していることを示す。２つ目は、ホットスパークと主燃料それぞれ２種ずつとバックグラウンド取得用１種の計５種の単色画像の取得について述べる。主燃料部の単色画像はホットスパーク部を取り囲むような構造を示しており、目標であったホットスパークと主燃料の同時分離診断が可能になったことを明らかにする。

第５章では、２つの直接照射爆縮実験における爆縮安定性の評価について述べる。１つ目は、ホットスパーク中のアルゴンが輻射する線スペクトルの時間変化を用いた評価と混合モデルとの比較である。実験では、ホットスパークの加熱途上から加熱部分とともに冷却部分が形成されていることを示唆する結果が得られた。さらに、球対称圧縮を仮定した流体輻射シミュレーション結果との比較では、特に最大圧縮近傍で開きがあり、高次モードの不均一圧縮に起因する主燃料（プッシャー）とホットスパークの混合を考慮したモデルでは、一定の範囲までしか説明できないことを示す。２つ目は、アルゴンのスペクトルの時間変化と単色画像計測の結果による安定性の評価、及び低次モード不均一圧縮を考慮に入れた２次元流体輻射シミュレーションとの比較を述べる。このように、ホットスパークの加熱、冷却に関してその空間・時間情報が得られるようになり、目標であったホットスパークの加熱のダイナミクスの解明に貢献できるようになったことを明らかにする。

第６章は結論であり、本研究で得られた成果をまとめ総括を行う。

Preface

This thesis is submitted for the degree of Doctor of Engineering. The research was conducted at the Institute of Laser Engineering in the Department of Electrical Engineering, Graduate School of Engineering, Osaka University. The objective of this research is to study implosion stability with x-ray spectroscopic method.

A considerable number of inertial confinement fusion (ICF) researches for thermonuclear ignition and burn of fusion fuel have been made intentionally for over the past 20 years. The most advanced method for ignition is to ignite the central part of the compressed fuel. Ablation pressure generated by intense laser irradiation compresses a spherical fusion pellet. Uniform compression creates a hot spark at the center as an ignitor and leads to burning a main fuel of cool dense fuel surrounding the hot spark, resulting in high gain. High-temperature heating of the hot spark and high-density compression of the main fuel were demonstrated separately, formation of them at the same time is needed.

Stable compression is essential for simultaneous formation of the hot spark and main fuel. This is why production techniques of uniform fusion capsule and uniform irradiation techniques of drive laser have been developed. Besides, hydrodynamical instabilities enhancing the compression non-uniformity have been well understood, especially for stabilization mechanism in these years. It is important to develop these techniques for stable compression and to understand phenomena in implosion process so as to predict implosion dynamics and make precise designs of ignition and high-gain. Therefore, experimental measurements of spark heating is needed with sufficient resolution for space and time.

X-ray spectroscopic method was utilized to diagnose the hot spark formation in this research. The advantages of the method is to give individual information on the hot spark and main fuel simultaneously, which has a potential for direct measurements of pusher/fuel mixing. What are often used as indicators for the implosion performance are yield of nuclear reaction products, ion temperature of the hot spark determined from a neutron spectrum, areal density of the hot spark from neutron yield ratio of different reactions, electron temperature and density from a x-ray line spectra with time- and space-integrated manner. These methods can not give enough information on implosion dynamics. The author applied a unique method giving spectral, spatial and temporal resolutions to diagnosis for laser fusion plasmas. This is a x-ray monochromatic camera (XMC) using toroidally bent perfect crystals. Using the XMC, two-dimensional images of hot spark and main fuel were obtained separately for the first time. In addition, the author paid attention on temporal variation of x-ray line spectra. These data led to new knowledge of hot spark dynamics.

This thesis consists of six chapters.

Chapter 1 describes introduction of this research. After discussing about the objective, principles, present state, and subjects of ICF research, the objective and meaning of this research are described. It is clarified that stable formation of the hot spark and main fuel is needed for the central ignition method, and that x-ray spectroscopic method is useful to measure them separately.

Chapter 2 describes principles to diagnose the imploded plasma by means of the x-ray spectroscopic method. It is shown that electron temperature and density dependence of line spectra from argon seeded in the fuel gas has a potential to diagnose hot spark, assuming collisional radiative equilibrium. Spatial and temporal variations of argon line emission are predicted by the help of a hydrodynamical radiation code and a spectrum analysis code, it is clarified that experimental measurements for the line x rays with sufficient resolutions is useful to know dynamics of hot spark.

In Chapter 3 development of diagnostics to know dynamics of hot spark and main fuel is described. Development of a x-ray monochromatic camera (XMC) to give spectral, spatial, and temporal resolutions simultaneously are mentioned. Clarified are the principles, features, design, and specification of the XMC with toroidally bent crystals. A x-ray streak spectrometer giving temporal variation of x-ray spectra is also mentioned.

In Chapter 4 demonstration of application of the XMC to implosion experiments is described. It is shown that usefulness of the XMC for fuel temperature mapping and for direct measurements of pusher/fuel mixing is demonstrated.

Chapter 5 discusses dependence of implosion stability on low modal irradiation non-uniformity in direct-drive experiments. Analyses of experimental data and comparison with simulations are described. Clarified is that the XMC developed is useful tool to diagnose the imploded plasma.

Finally, Chapter 6 gives the summary and conclusion of this research.

Contents

Chapter 1

Introduction

1-1 Key issues in inertial confinement fusion (ICF) research

1-1-1 Principles of inertial confinement fusion

Inertial confinement fusion (ICF) research has been extensively made to demonstrate controlled thermonuclear burn with a high power lasers.[1, 2] In this section, principles and study subjects of ICF are described briefly with several remarkable achievements.

The idea of ICF is to create hot (> keV) and dense (~100g/cm^3) fuel confined with inertial force in a short duration (~10^{-11} seconds), yielding thermonuclear fusion energy. Figure 1-1-1 schematically shows a sequence of ICF. The fusion capsule consists of a spherical shell and a fuel gas (Fig. 1-1-1(a)). The shell has a solid fuel at the inner layer and the ablator at the outer layer. The gas fuel turns to be ignitor when the capsule is compressed. Deuterium (D) and tritium (T) are used as the fuel because of largest reaction rate.[3] The D-T reaction is expressed as

$$ {}^2_1D + {}^3_1T \rightarrow {}^4_2He\,(3.5MeV) + {}^1_0n\,(14.1MeV). \qquad \text{Eq. 1-1-1} $$

As shown in Fig. 1-1-1(b), the sequence has four steps:

(1) Energy deposition

When radiation energy incident on the surface of the capsule, it is heated up intensively providing very high ablation pressure. Intense laser light (or soft x rays produced by laser) is used as the driver. Symmetric compression of the fusion capsule is attained only when

---

[1] J. H. Nuckolls et al., Nature (London) **239**, 139 (1972).

[2] K. A. Brueckner and S. Jorna, Rev. Mod. Phys. **46**, 325 (1974).

[3] for example; Inertial Confinement Fusion, J. J. Duderstadt and G. A. Moses, John Wiley & Sons. Inc., N.Y. 1982.

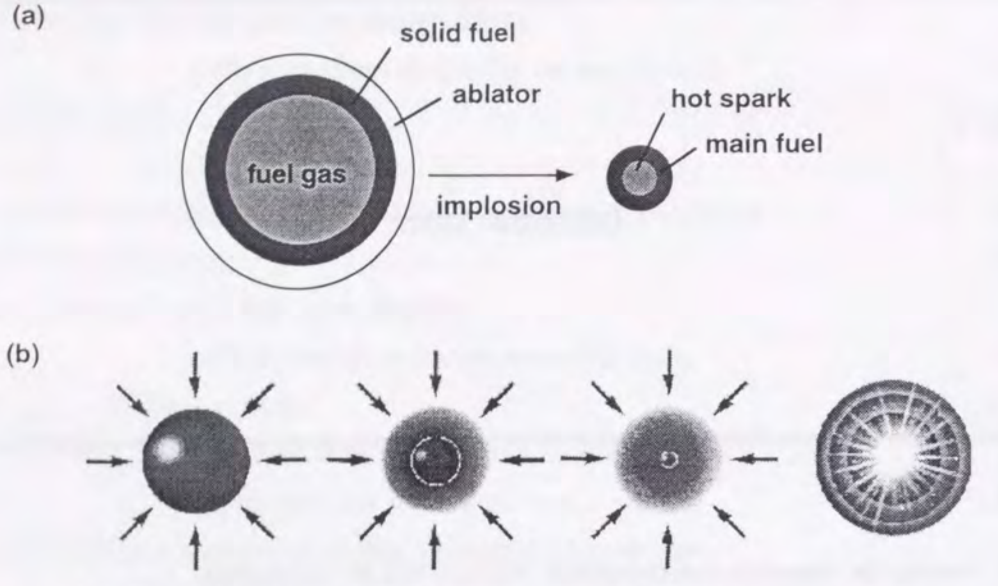

(b-1) Energy deposition (b-2) Compression (b-3) Ignition (b-4) Burn

Figure 1-1-1 (a) Structure of the fusion capsule for inertial confinement fusion (ICF) and (b) a sequence of ICF.

extremely uniform radiation is supplied onto the capsule surface.

(2) Compression

The ablation pressure both accelerates the ablated material outwards and as its reaction the shell inwards. In this way the absorbed driver energy is converted to kinetic energy of the shell via thermal energy of the heated material. The converging shell compresses the gas and main fuels. Radial convergence ratio of the fuel gas reaches 30-40.

(3) Ignition

The fuels are compressed adiabatically so that the central gas fuel forms a hot spark to ignite the main fuel. At this stage, kinetic energy of the shell is finally converted to internal energy of the hot spark. When the size of the hot spark exceeds the mean free path of the alpha particle produced by D-T reaction, the hot spark is rapidly heated by alpha particles, leading to formation of burn wave (ignition). Typical ignition condition is above 5 keV in temperature and 0.3 g/cm^2 in areal density.[4]

(4) Burn

The burn wave propagates through the compressed main fuel layer before the plasma is disassembled, yielding much more energy beyond the input (high gain).

A key to success of the scenario is formation of the hot spark and cold dense main fuel.

---

[4] H. Azechi, Kakuyugo Kenkyu (J. Jpn. Soc. Plasma. Sci. Nucl. Fusion Res.) **68** (supp.), 13 (1991).

Issues to realize the scenario are divided into the following four factors;

(1) demonstration of high-gain,

(2) development of a high-power, efficient, and high-repetition-rate driver,

(3) production of uniform fusion capsule, and

(4) development of ICF reactor engineering.

These four factors are the subjects of ICF research. As far as the first and second factors may concern, a number of studies have been done since the concept of ICF was presented.[1] Most of the studies treated have focused on the issues associated with stable compression of the fusion capsule, and upgrading laser technology for uniform irradiation. As a result, we are almost close to the demonstration of thermonuclear ignition. The fourth factor is important to obtain electricity for civilian use and to diminish the nuclear wastes and radio-active materials.

Figure 1-1-2 schematically shows spatial distributions of temperature and density of the hot spark and the main fuel at the maximum compression. The outstanding achievements in the ICF experiments performed in the recent decade are obtaining hot spark temperature up to 10 keV[5] and main fuel density up to 600 times solid density.[6] Although these temperature and density are close to those required for the ignition, neutron yield was three-orders of magnitude smaller than that predicted by one-dimensional hydro-code simulation in which perfect spherical compression is assumed. It is deduced from the comparison of implosion experiments and the simulation that non-uniform compression of the fusion capsule prevents stable formation of the

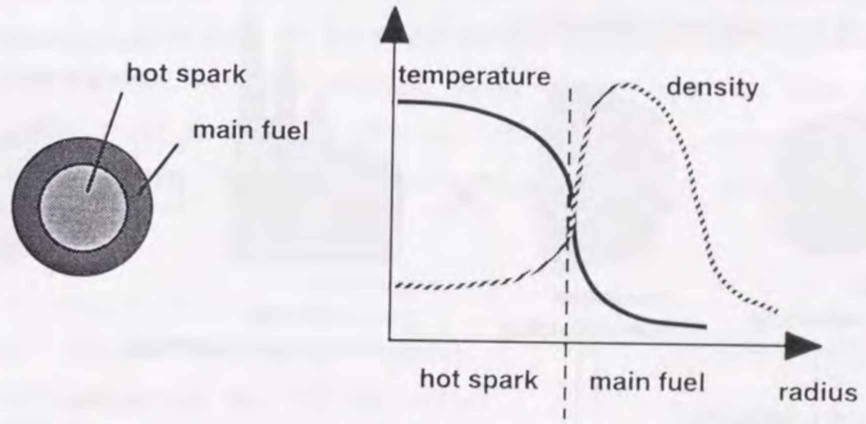

Figure 1-1-2 Structure of hot spark and main fuel. A key to ignition and burn is stable formation of such structure.

---

[5] C. Yamanaka and S. Nakai, Nature **319**, 757 (1986).

[6] H. Azechi et al., Laser and Particle Beams **9**, 193 (1991).

hot spark. Hence, one of important issues for ignition and burn is to ensure the implosion uniformity and to understand implosion dynamics with high accuracy.

1-1-2 Factors of implosion non-uniformity

Sources of non-uniform implosion are inhomogeneity of the fusion target and non-uniform irradiation of the laser. Hydrodynamic instabilities occurring during implosion enhance the non-uniformity. These instabilities, causing perturbations on and in the target, have strong influence on implosion performances due to insufficient compression and pusher/fuel mixing. Described in this section are these factors of implosion non-uniformity.

1. Target

Although, in previous experiments, glass microballoons (GMB) have been used for a fuel container, plastic shells are now commonly used in the laser fusion experiments. The GMBs are inadequate for achieving high-density compression, because of x-ray preheat provided by the silicon in the glass and hydro-instabilities because of density miss-matching between the shell and the fuel. The plastic shells can reduce the radiation preheat and the instability because of its relatively low atomic number and mass density.

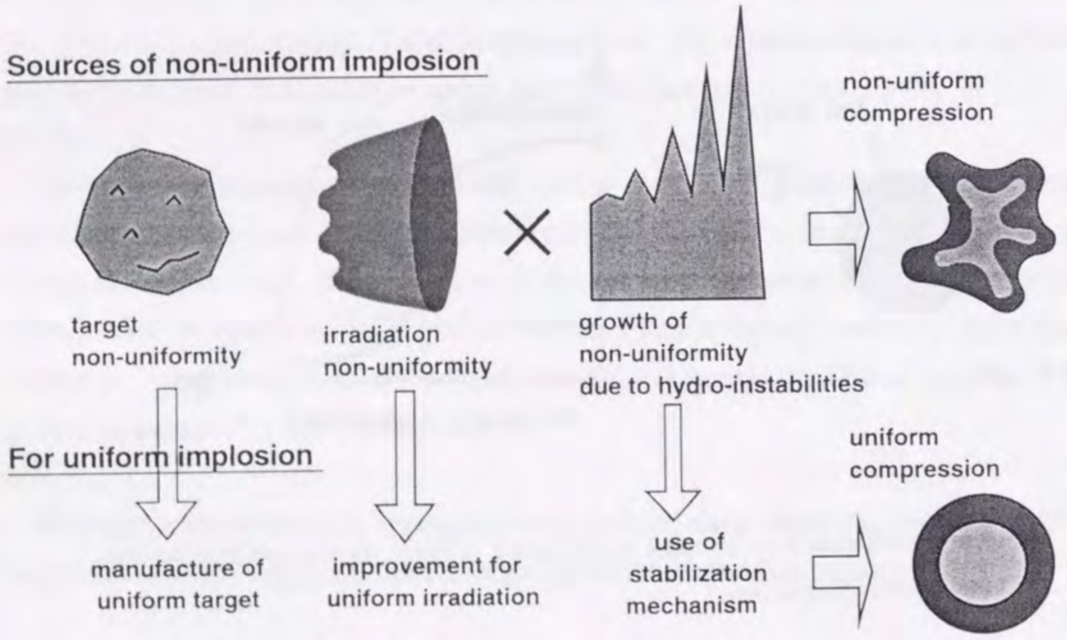

Figure 1-1-3 Three factors determining implosion non-uniformity and improvements for uniform compression.

Uniform plastic shells can be fabricated by using a density-matched emulsion method.[7] Sphericity of 99.8% and wall thickness uniformity of 99.9% have been achieved in the range from 100 to 1500 μm of the diameter and from 3 to 15 μm of the wall thickness of the shell. The surface smoothness of less than 0.1 μm has also been achieved. These values already satisfy the uniformities necessary for reactor use.

2. Laser

Irradiation non-uniformity of multi-beam laser systems in each Legendre mode can be expressed as the product of two factors which depend on, respectively,[8]

(1) geometrical configuration of the laser system, including the number and orientation of the laser beams, and the laser power balance among beams.

(2) energy deposition profile with a single beam. This is determined by the focal position, intensity profile across the beam, and the f-number of focus lens.

Improvements of irradiation uniformity have been made in these two factors. Regarding (1), all laser facilities for ICF experiments are lay-outed spatially symmetric orientation. The laser power balance of 3% at the peak of the pulse has already been achieved in GEKKO XII green laser system at Institute of Laser Engineering (ILE) in Osaka University.[9] These factors make influence mainly on low modal non-uniformity.

Regarding (2), a single beam pattern contributes to moderate and high modal non-uniformities. The envelop of the intensity profile on the target can be controlled with a multi-lens array,[10] a phase plate such as random phase plate (RPP),[11] and a kinoform phase plate.[12] Since interference of laser light on the target surface produces many speckles which have periodic highest intensity in a few microns pitch, coherency of the laser light has been suppressed to smear out the speckles. The smoothing methods proposed are smoothing by spectral dispersion (SSD),[13] induced spatial incoherence (ISI),[14] polarization control plate

---

[7] M.Takagi et al., J. Vac. Sci. Technol. **A 9**, 2145 (1991).

[8] S. Skupsky and K. Lee, J. Appl. Phys. **54**, 3662 (1983).

[9] M. Nakatsuka et al., *proc. of 12th Int. Conf. on Laser Interaction and Related Plasma Phenomena* **2**, (AIP press, New York, 1996) 963.

[10] X. Deng et al., Appl. Opt. **25**, 377 (1986); N. Nishi et al., *Proc.* of SPIE **1870**, 105 (1993).

[11] Y. Kato et al., Phys. Rev. Lett. **53**, 1057 (1984).

[12] S. N. Dixit et al., Opt. Lett. **19**, 417 (1994); Y. Lin et al., Opt. Lett. **20**, 764 (1995).

[13] S. Skupsky et al., J. Appl. Phys. **66**, 3456 (1989).

[14] R. H. Lehmberg and S. P. Obenschain, Opt. Commun. **46**, 27 (1983).

(PCP)[15] and partial coherent light (PCL).[16] At ILE, a drive pulse consisting of PCL as a foot pulse and two-dimensional SSD[17] as a main pulse have been proposed.[18] A 2% level of irradiation non-uniformity with PCL was expected by using a single beam intensity profile.

In case of tangential incidence of laser light onto the target, refraction of light in the surrounding plasma should be taken into account when laser absorption non-uniformity is estimated.[9, 19] This may be controlled by envelop tailoring of a single beam. A technique to measure the absorption non-uniformity on a spherical target has been developed.[20] In addition to such effects of density and temperature gradients in the expanding plasma, converging effects should be also considered to estimate implosion non-uniformity precisely.

3. Hydrodynamic instabilities

Hydrodynamic instabilities in implosion process grow perturbations on and in a target.[21,22] Figure 1-1-4 shows the hydrodynamic instabilities and associated phenomena in the implosion process. There are three phases in the implosion process till the maximum compression. The first phase is the initial phase before the pusher, which compress the main and gas fuels, is accelerated. When the laser irradiates the target surface, perturbations are seeded on the surface due to irradiation non-uniformity. The surface perturbations due to the 'initial imprints,' together with the original target surface roughness, are accompanied by a rippled shock wave before it reaches the inner surface of the shell. The second phase is an acceleration of whole shell. After the shock breakout to the inner surface, the perturbations grown on the outer surface due to Rayleigh-Taylor (RT) instability are fed through on the inner surface. The third phase is a deceleration of the shell due to pressure work from the compressed fuel. The perturbations appearing on the inner surface along with original inner surface roughness are amplified due to R-T instability, resulting in mixing pusher into fuel material.

It is worthwhile to pay attention to the R-T instability providing large growth of perturbations.[21,22] The R-T instability occurs at the interface between low density (ρ_1) and high density (ρ_2) incompressive fluid under gravitational force (Fig. 1-1-5). A small perturbation of wavelength λ at the interface grows due to lateral flow of the fluid driven by the gravitation. The perturbation growth due to R-T instability can be expressed as

$$\xi_k(t) = \xi_{k,t=0} \exp(\gamma_k t), \tag{Eq. 1-1-2}$$

where ξ_k is the perturbation amplitude of the wave number k (=$2\pi/\lambda$), t is the time, and γ_k is the R-T growth rate. The classical growth rate is given as

$$\gamma_k = \sqrt{\alpha_A k g}, \tag{Eq. 1-1-3}$$

where g is the acceleration and α_A is the Atwood number

$$\alpha_A = \sqrt{\frac{\rho_2 - \rho_1}{\rho_2 + \rho_1}}. \tag{Eq. 1-1-4}$$

In case of the R-T instability occurring at outer (ablation) surface of the pusher, the growth rate is modified due to ablation effect as

$$\gamma_k = \sqrt{\frac{kg}{1+kL}} - \beta k \frac{\dot{m}}{\rho_a}, \tag{Eq. 1-1-5}$$

where L is the density scale length at the ablation surface,

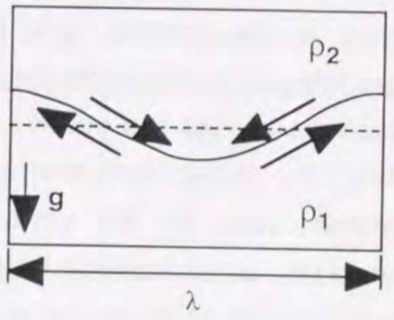

Figure 1-1-5 Schematics of perturbed interface in gravitation. λ is the wavelength of the perturbation

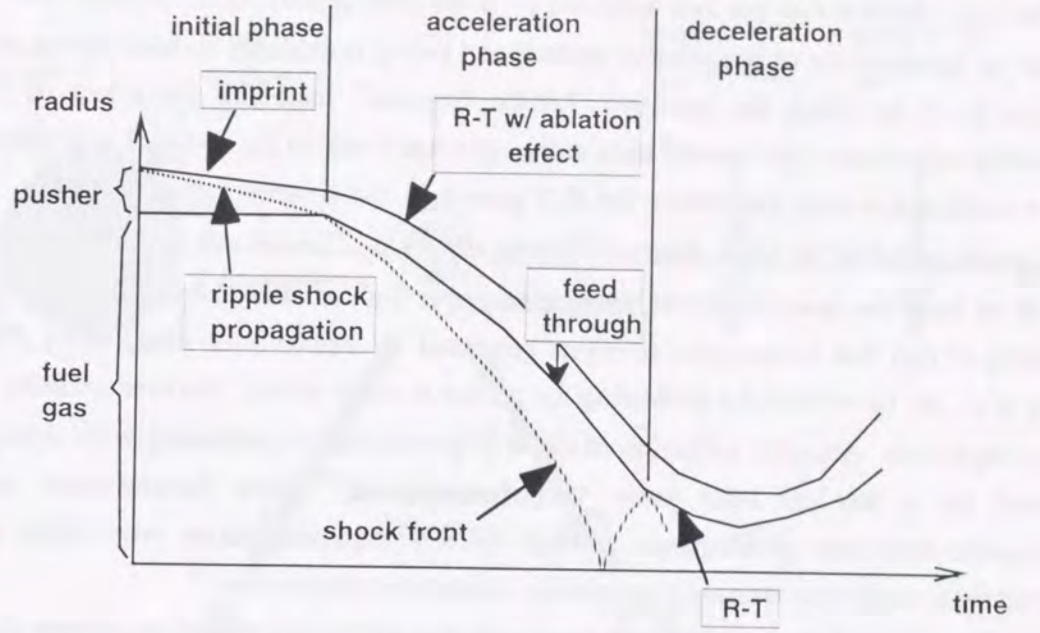

Figure 1-1-4 Hydrodynamic instabilities and associated phenomena in implosion process. Perturbations grown by the instabilities lead to failure to formation of hot spark surrounded by main fuel (pusher).

---

[15] K.Tsubakimoto et al., Opt. Commun. **91**, 9 (1992).

[16] H. Nakano et al., J. Appl. Phys. **73**, 2122 (1993).

[17] S. Matsuoka et al., Appl. Phys. Lett., to be published.

[18] N. Miyanaga et al., presented at ECLIM (1997).

[19] K. Nishihara et al., Phys. Plasmas **1**, 1653 (1994).

[20] H. Honda et al., Fusion Eng. Design **34-35**, 197 (1997); H. Honda et al., Technol. Repts. Osaka Univ., in press.

[21] H. Takabe, J. Plasma and Fusion Research (in Japanese) **73**, 147, 313, and 395 (1997), and references therein.

[22] H. Azechi et al., Phys. Plasmas **4**, 4079(1997), and references therein.

$\dot{m}$ is the mass ablation rate per unit area, and ρ_a is the peak density at the ablation front. The β depends on the structure of the ablation surface and β~3-4 is expected in laser driven ablation. Equation 1-1-5 is called the modified Takabe formula[23] including the effect of ablative stabilization expressed as the second term in the right-hand-side of Eq. 1-1-5. Large value of the ablative stabilization term can reduce the R-T growth at the ablation surface (see Fig. 1-1-3), which corresponds to the large ablation velocity of $\dot{m}/\rho_a$. The $\dot{m}$ can be enhanced by high intensity of the drive laser. However, there is an upper limit of laser intensity in order to avoid preheating of fuel due to energetic electrons generated by laser-plasma interactions. The peak density of ρ_a can be reduced by preheating the pusher to some extent, however resulting in high entropy implosion. Actually, reduction of the R-T growth due to preheating with strong shock generated by a fast-rise laser pulse was demonstrated.[22] Also demonstrated was that experimental implosion performance in high entropy implosion mode were close to ones predicted by a simulation assuming completely symmetric compression.[24]

These three factors determining implosion non-uniformity as well as entropy should be carefully controlled. Quantification of tolerable level of implosion non-uniformity is also required by means of observation of the hot spark formation and its dynamics.

1-2 Observation of hot spark formation by x-ray spectroscopy

Figure 1-2-1 shows how x-ray spectroscopic method can give information on the pusher and fuel separately. The points are that different materials are doped in individual parts of the target and that line x rays from both materials can be resolved by the help of x-ray spectroscopy. The dopants are chosen in such a way that line x rays emitted from respective dopants have enough intensity for measurements at temperature and density of the imploded plasma. In this research, $_{18}$Ar in the fuel and $_{17}$Cl in the pusher are doped as tracers. Monochromatic x-ray images for individual lines emitted from argon and chlorine give spatial distribution of fuel and pusher, which has a great potential to observe pusher/fuel mixing directly. No studies have ever made to observe the mixing directly with spatial resolution. Moreover, since the line spectra emitted from the dopant have temperature and density information, monochromatic imaging method has also a potential to give a temperature and density mapping of the pusher and fuel separately. In this way, x-ray spectroscopic method can be applied to diagnose the imploded plasmas in order to understand the hot spark dynamics including pusher/fuel mixing.

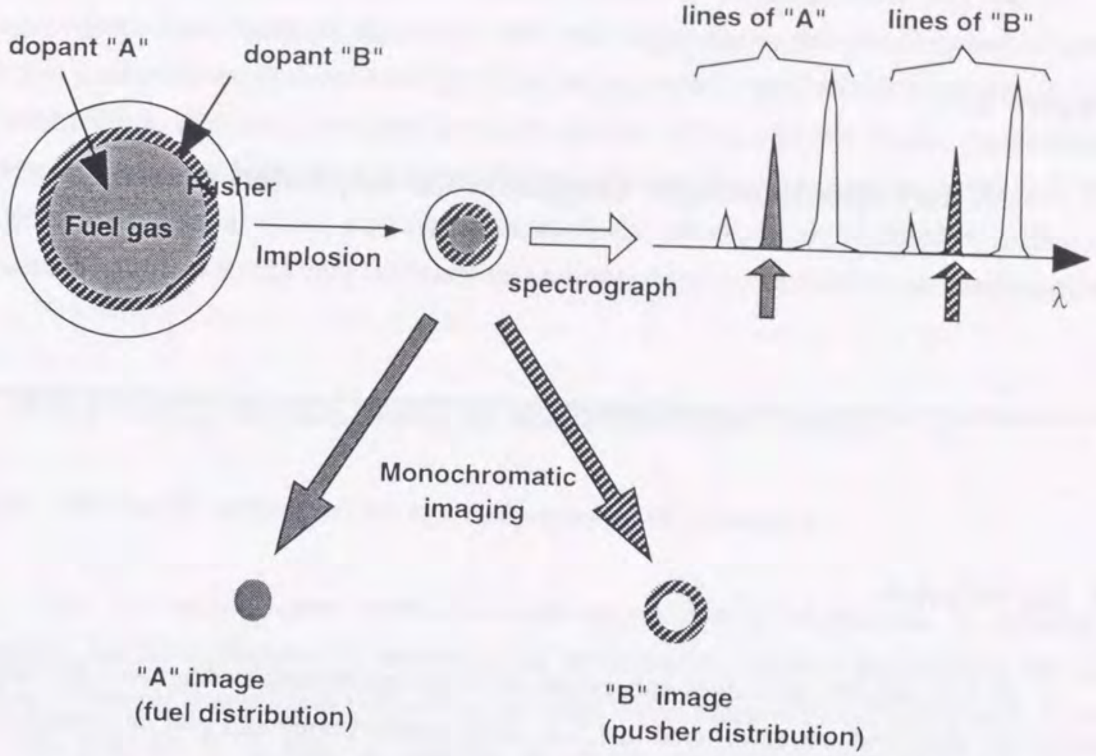

Figure 1-2-1 X-ray spectroscopic method to obtain information on pusher and fuel separately.

The objective of the present study is to investigate the implosion stability by the x-ray spectroscopic measurements. Principles and features of the x-ray spectroscopic measurements are given in Ch.2. After describing a novel method providing the temperature mapping of compressed plasma and direct observation of the mixing in Ch.3, x-ray driven implosion experiments and results to demonstrate the usefulness of the novel diagnostics are reported in Ch.4. Analyses of experimental data and comparison with hydro-code simulations in laser driven implosion are described in Ch.5. Conclusions and future prospects are given in Ch.6 as the summary of this work.

---

[23] H. Takabe et al., Phys. Fluids **28**, 3676 (1985); J. D. Kilkenny et al., Phys. Fluid **1**, 1379 (1994).

[24] K. Mima et al., Phys. Plasmas **3**, 2077 (1996).

Chapter 2

X-ray spectroscopic diagnosis for imploded plasmas

2-1 Introduction

In this chapter, principles and merits of x-ray spectroscopic diagnosis for imploded plasmas are described. As mentioned in Ch. 1, x-ray spectroscopy can give information about main fuel (pusher) and hot spark (fuel) separately, which is clarified here.

First of all, it is clarified that x-ray measurements are useful to know implosion dynamics. To diagnose imploded hot (~keV) dense ($>10^{23}$ cm^{-3}) plasmas, there are several methods which utilize nuclear reaction products or x rays emitted from the compressed plasmas.[1] The measurement of nuclear products such as neutrons can give its yield as the most basic parameter of the implosion performance, temporal variation and spatial distribution of the reaction. It is true that these measurements can give information on the hot fusion plasma, but neutrons having large kinetic energy (~MeV) is too interactive with materials to be detected with sufficient resolution for both space and time. In this respect, the use of x rays simplifies spatial and temporal resolving measurements due to lower photon energy (~ keV). This is why the x-ray measurement is commonly used to investigate dynamics of not only imploded but also imploding plasmas.

In addition, it is worthwhile to take notice of the x-ray spectra depending on temperature and density of plasmas. Using such spectra, one can investigate the process of heating, compression, cooling, and disassemble of the imploded plasma. Moreover, theoretical models enable us to estimate plasma parameters (temperature and density) from experimental spectra. Therefore appropriate models are necessary to derive relationship between spectra and the plasma parameters in the imploded plasma regime.

---

[1] H. Azechi et al., Fusion Eng. Design **34-35**, 37 (1997).

Sec. 2-2 describes x-ray line spectra depending on temperature and density. After introducing the fluid equations and energy transport in plasmas to describe behavior of plasmas, radiation transport among several energy transport processes is paid attention because it plays an important role to emit x rays outward from the plasma. Using a proper model, temperature and density dependence of line spectra emitted from a uniform plasma is shown. In sec. 2-3, spatial and temporal variation of line emission from imploded plasmas are presented. Clarified is that measurement of line x rays with sufficient resolutions can give information on spark heating.

2-2 X-ray line spectra depending on temperature and density

2-2-1 Radiation transport in hydrodynamics of plasmas

In this section, after hydrodynamical approximation of plasmas to describe the dynamics, radiation transport is introduced as an important element in modeling hot dense plasmas. Contents presented in this section are used in the numerical simulation code ILESTA-1D.[2] The ILESTA-1D is used to compare the results with the experimental one, which is discussed in the second half of this thesis.

To describe laser fusion plasma phenomena, hydrodynamical approximation of the plasma are essentially necessary. Basic fluid equations represent conservation of mass, momentum, and energy. The conservation of mass is expressed as

$$\frac{d\rho}{dt} = -\rho\nabla\cdot u, \qquad \text{Eq. 2-2-1}$$

where ρ is mass density of the plasma and u is flow velocity. The next is conservation of the momentum,

$$\rho\frac{du}{dt} = -\nabla(P+Q), \qquad \text{Eq. 2-2-2}$$

where P is the pressure consisting of electron, ion, and other pressure due to the laser light (ponderomotive force), radiation, alpha particles, etc., and Q is the numerical viscous pressure. Then the conservation of energy is described as

---

[2] H. Takabe et al., Phys. Fluids **31**, 379 (1988); H. Takabe and T. Nishikawa, J. Quant. Spectrosc. Radiat. Transfer **51**, 379 (1994).

$$\rho\frac{d\varepsilon_i}{dt} = -(P_i+Q)\nabla\cdot u - \nabla\cdot q_i + Q_{ei} + S_\alpha^i,$$
$$\rho\frac{d\varepsilon_e}{dt} = -P_e\nabla\cdot u - \nabla\cdot q_e - Q_{ei} + S_L + S_r + S_\alpha^e, \qquad \text{Eq. 2-2-3}$$

where the subscript i (e) represents ion (electron), ε is energy per unit mass, q is the heat flux, S_α is, Q_{ei} is the electron-ion energy relaxation term, S_L, S_r, and S_α are the energy source derived from laser heating, radiation, and alpha particles respectively. One can describe the behavior of the plasma by using these fluid equations, energy transport, and the equation of state (EOS).

The energy transport mechanisms consist of radiation and alpha particle transport and electron thermal conduction. The radiation transport can be expressed as

$$\frac{1}{c}\frac{dI^\nu}{dt} + \Omega\cdot\nabla I^\nu = \eta^\nu - \chi^\nu I^\nu, \qquad \text{Eq. 2-2-4}$$

where I^ν is the spectral (ν) radiation intensity, c is the speed of light, and Ω represents the unit vector of the direction of the radiation propagation. In the right hand side of Eq. 2-2-4, η^ν is the spontaneous emission rate per unit volume, unit time, unit spectral internal of ν, and unit solid angle. The absorption coefficient χ^ν consists of pure absorption minus the induced emission contribution. These η^ν and χ^ν contribute to not only energy transport in the plasma but also the spectra emitted from the plasma, which can be useful for diagnosis because they have temperature and density dependence. While spectra emitted from plasmas, in general, are determined both from the η^ν and χ^ν, emission spectra in little absorption case and absorption spectra in little emission case are commonly utilized for temperature and density determination because simple models providing spectra can be used. In this research, emission dominant case is treated for measurements of fuel and pusher. Although detail of the other energy transport mechanisms is not mentioned here, they can greatly contribute to the plasma dynamics. The alpha particle transport is very important to ignite and burn the fusion fuel, leading to high-gain design. The electron transport is also important, especially for behavior of fast (energetic) electrons which has a potential of controlling adiabatic of the compressing fuel and implosion stability.[3]

2-2-2 Temperature and density dependence of x-ray line spectra

Collisional radiative equilibrium (CRE) model is widely used to describe radiation in plasmas.[4] CRE model can be applied to wide range of plasma density because atomic processes are taken into account directly. In this research, RATION code[5] is used for spectrum analysis. RATION code produces K-shell spectra with a steady state kinetics model, taking into account Stark and electron-impact broadening.

Let us consider ion population density of argon seeded in an homogeneous hydrogen plasma corresponding to the hot spark. As mentioned in Ch. 1, doped material is chosen so that line x rays emitted from the dopant have enough intensity for measurements at temperature and density of the imploded plasmas. In this research, $_{18}$Ar in the fuel and $_{17}$Cl in the pusher are doped as tracers. Treated hereafter is the mixture plasmas of hydrogen and argon, and the concentration of argon is assumed as 0.2% in atomic number density. Figure 2-2-1 shows electron temperature dependence of ion population density of argon in the mixture plasma. The electron density is fixed at 10^{23} cm^{-3} which is a typical value in the current experiments. It is seen that dominant ion charge increases as electron temperature increases. Helium-like ion (Ar^{+16} in this case) is dominant in wide range of electron temperature because K-shell is occupied with two bound electrons. This is why lines emitted from He-like ions are often used for diagnosis. The shading indicates experimental regime where He-like and hydrogen-like (Ar^{+17}) ions dominate. Hence, lines from He- and H-like ions were chosen for diagnosis in this research. Among the lines, Heß (Ar^{+16} 1s3p-1s^2) and Lyß (Ar^{+17} 3p-1s) lines were used for diagnosis due to optically thin lines. The reason why optically thin lines are used is to obtain information on not an outer surface of the plasma but the whole one. Since the opacity problem is important to determine concentration of a tracer, it needs to be clarified. In the experiments

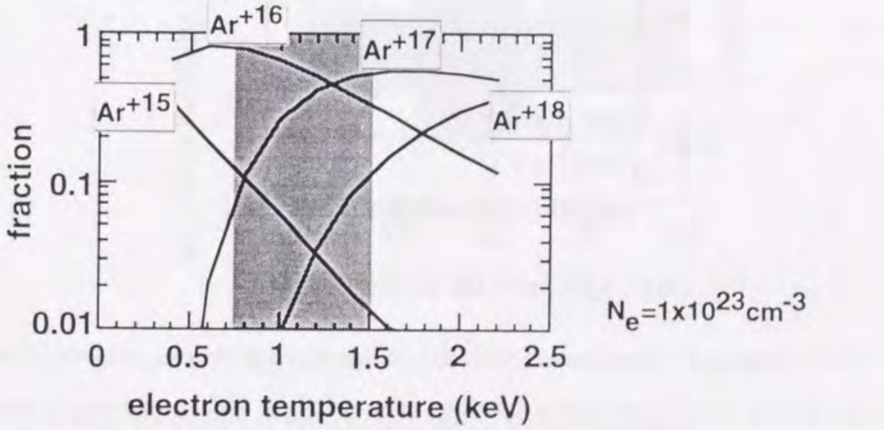

Figure 2-2-1 Temperature dependence of ion population. The electron density is 10^{23} cm^{-3}. The shading indicates an typical experimental regime.

---

[3] for example, M. Honda et al., Phys. Plasmas **3**, 3420 (1996).

[4] Plasma Diagnostic Techniques, R. H. Huddlestone and S. L. Leonard, Academic Press, N.Y., 1965.

described in Ch.4 and Ch.5, the amount of argon was minimized to insure that it has little influence on implosion dynamics and that the diagnostic line are optical thin. The optical depth of the Heβ line can be written as

$$\tau(\upsilon) = n_{He\,like}\, R_{plasma} \left(\frac{\pi e^2}{m c} \right) f_{He\beta}\, \phi(\upsilon), \qquad \text{Eq. 2-2-5}$$

where $n_{He\ like}$ is the number density of He-like ions of argon for absorption of the line, R_{plasma} is the radius of the compressed fuel plasma, $(\pi e^2/mc)$ is the absorption cross section of an electron,

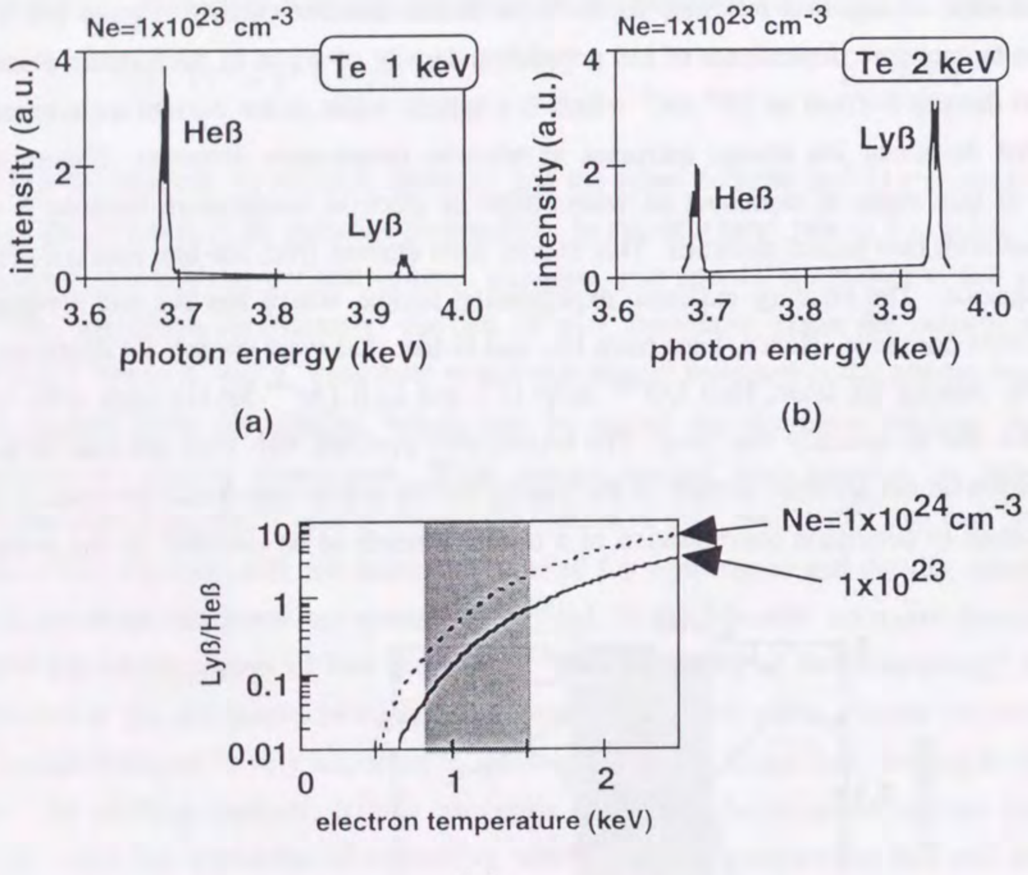

(a) (b)

(c)

Figure 2-2-2 Temperature dependence of Heβ and Lyβ line of argon. Spectra in 1 keV (a) and 2 keV (b) in electron density of 10^{23} cm^{-3}. (c) is intensity ratio of Lyβ to Heβ vs. electron temperature. The electron temperature dependence of the lines is mainly due to that of ion population shown in Fig. 2-2-1. The shading indicates experimental temperature regime.

---

[5] R. W. Lee et al., J. Quant. Spectrosc. Radiat. Transfer **32**, 91 (1984).

$f_{He\beta}$ is the oscillator strength of the Heβ line, and $\phi(\nu)$ is the line shape factor. Given the concentration of argon is 0.2%, $n_{He\ like}$ = (2-5) 10^{20} cm^{-3}, R_{plasma} = 15-20 μm, and assuming the fractions of H-like and He-like argon ions to be equal to 50%, $f_{He\beta}$ = 0.147 (Ref.6) and $\phi(\nu)$ = 1.5 10^{-16} s at the line center (corresponding to the experimental line width of 30 eV), the optical depth of the Heβ line is estimated to be 0.3-0.5. In the same manner, the optical depth of the Lyβ line is estimated to be 0.3-0.5. It is plain that the argon concentration of 0.2% satisfies optically thin condition for Heβ and Lyβ lines. Besides, this low concentration of the dopant also minimizes influence on the hydrodynamics.

Temperature dependence of line spectra can be utilized for determination of heating or

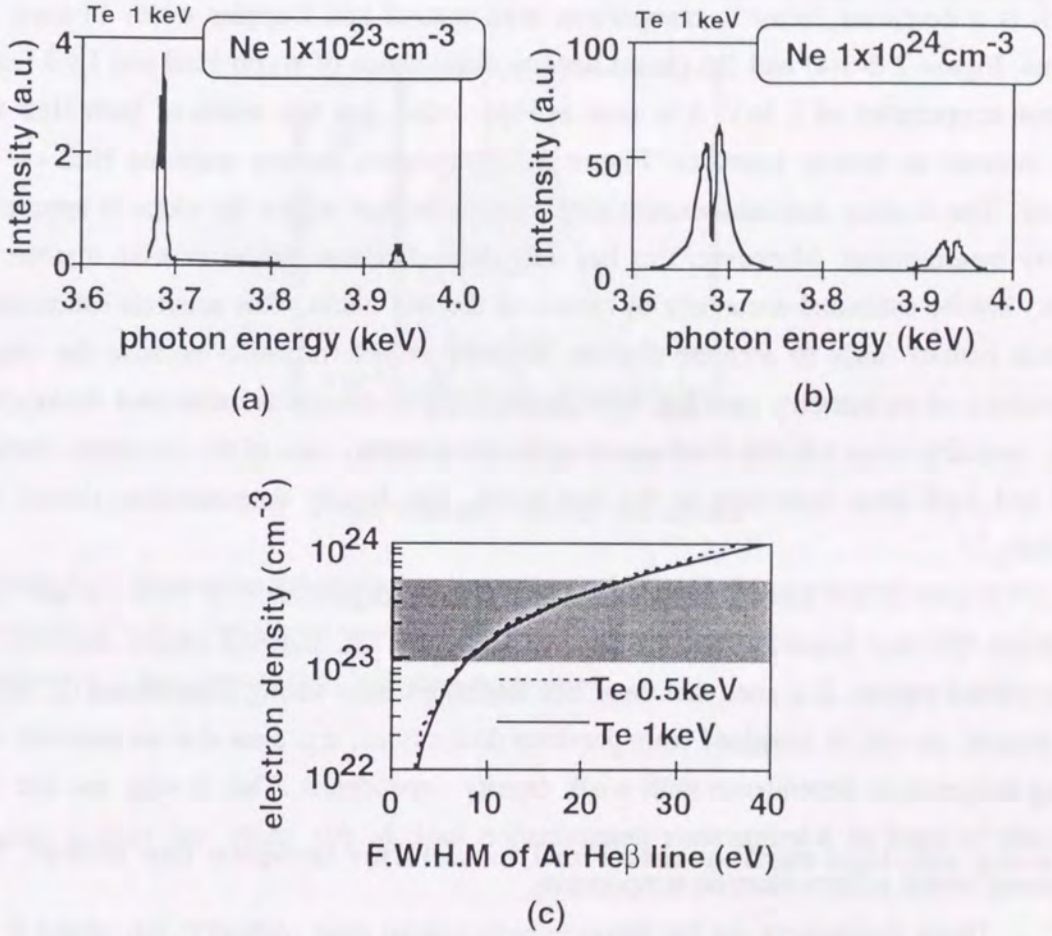

(a) (b)

(c)

Figure 2-2-3 Density dependence of Heβ and Lyβ line of argon. Spectra in 10^{23} cm^{-3} (a) and 10^{24} cm^{-3} (b) in electron temperature of 1 keV. (c) is full width at half maximum of argon Heβ line vs. electron density. Stark broadening is dominant in the line width due to high electron density. The shading indicates experimental density regime.

---

[6] D. H. Sampson et al., At. Data Nucl. Tables **21**, 467 (1983).

cooling of plasmas. As shown in Fig. 2-2-1, ion population density has temperature dependence so that line intensity from the ion has also temperature dependence. Figures 2-2-2(a) and (b) show temperature dependence of argon Heß and Lyß lines at the electron density of 10^{23} cm^{-3}. It is seen that the intensity of Lyß line is higher than that of Heß line in higher temperature, which is reflected in the intensity ratio of Lyß to Heß lines vs. electron temperature shown in Fig. 2-2-2(c). The main reason for weak dependence of the ratio on electron density is that ionization of argon ions is enhanced by electron collisions due to high electron density. The shading indicates experimental temperature regime where the slope is appropriate for temperature measurement.

Density dependence of line spectra appears in the line width due to Stark broadening which is a dominant factor in comparison with natural and Doppler width in such a dense plasma. Figure 2-2-3(a) and (b) shows density dependence of argon Heß and Lyß lines at the electron temperature of 1 keV. It is seen in Figs. 2-2-3 that line width of both Heß and Lyß lines increase as density increases. Figure 2-2-3(c) shows the line width of Heß vs. electron density. The shading indicates experimental density regime where the slope is appropriate for density measurement. Moreover, this has little dependence of temperature so that the electron density can be estimated accurately by means of the line width. This accurate estimation of the electron density leads to accurate electron temperature determination because the temperature dependence of the intensity ratio has weak dependence of density as mentioned above (Fig. 2-2-2(c)). Actually, since satellite lines appearing in lower energy side of the resonance lines such as Heß and Lyß lines contribute to the line width, the density determination should be done carefully.[7,8]

Figure 2-2-4 shows temperature and density dependence of Heß (a) and Lyß line intensities (b) and intensity ratio of Lyß to Heß (c). The hatched region indicates current experimental regime. It is seen that these line intensities have strong dependence of temperature and density. As can be imagined from previous discussions, it is clear that the intensity ratio has strong temperature dependence with weak density dependence. This is why the line intensity ratio can be used as a temperature determination tool. In this study, the ratio is utilized as a parameter which reflects electron temperature.

These discussions are for homogeneous plasma case. Actually, our object is plasmas having rapidly changing spatial gradients of temperature and density. It should be confirmed that the dependence is useful so as to obtain information on hot spark heating process, which is described in the following section.

---

[7] R. C. Mancini et al., Rev. Sci. Instrum. 63, 5119 (1992).

[8] N. Woolsey et al., J. Quant. Spectrosc. Radiat. Transfer, in press.

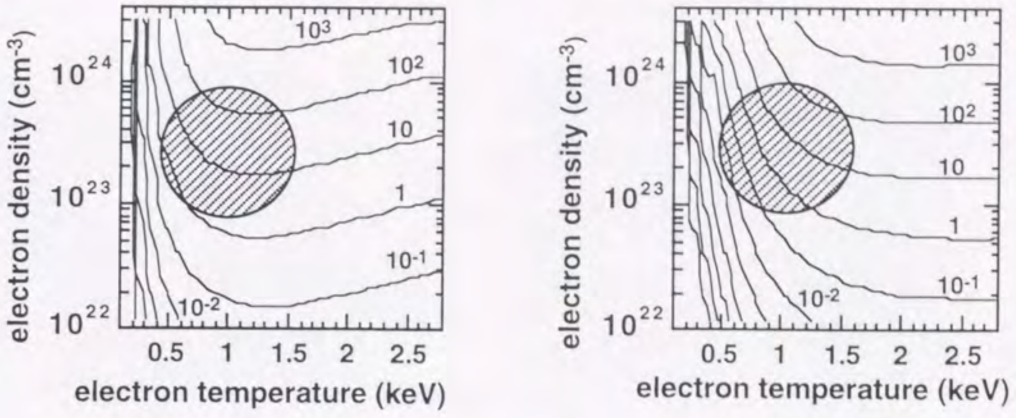

(a) Ar^{+16} 1s3p-1s^2 (Heß) line intensity

(b) Ar^{+17} 3p-1s (Lyß) line intensity

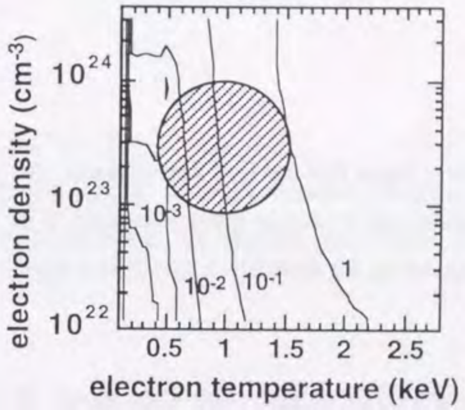

(c) intensity ratio of Lyß to Heß

Figure 2-2-4 Temperature and density dependence of argon Heß and Lyß line intensities and intensity ratio of Lyß to Heß. The hatched region indicates the current experimental region. It is seen that strong dependence of line intensity ratio on electron temperature.

2-3 Spatial and temporal variation of line emission from imploded plasma

In this section, it is clarified that line emissions from imploded plasma are useful for diagnostics, and that spectral, spatial, and temporal resolving measurement is needed.

Using ILESTA-1D and RATION, temporal variation of the line emission can be predicted. Although hydrodynamics of implosion with radiation transport are described by the ILESTA-1D that is bench-marked with experimental results, detail line x rays emitted from, for instance, argon are not described. Hence, temperature and density distribution of the imploded plasma derived from the ILESTA are replaced by the emission intensities of argon lines by the

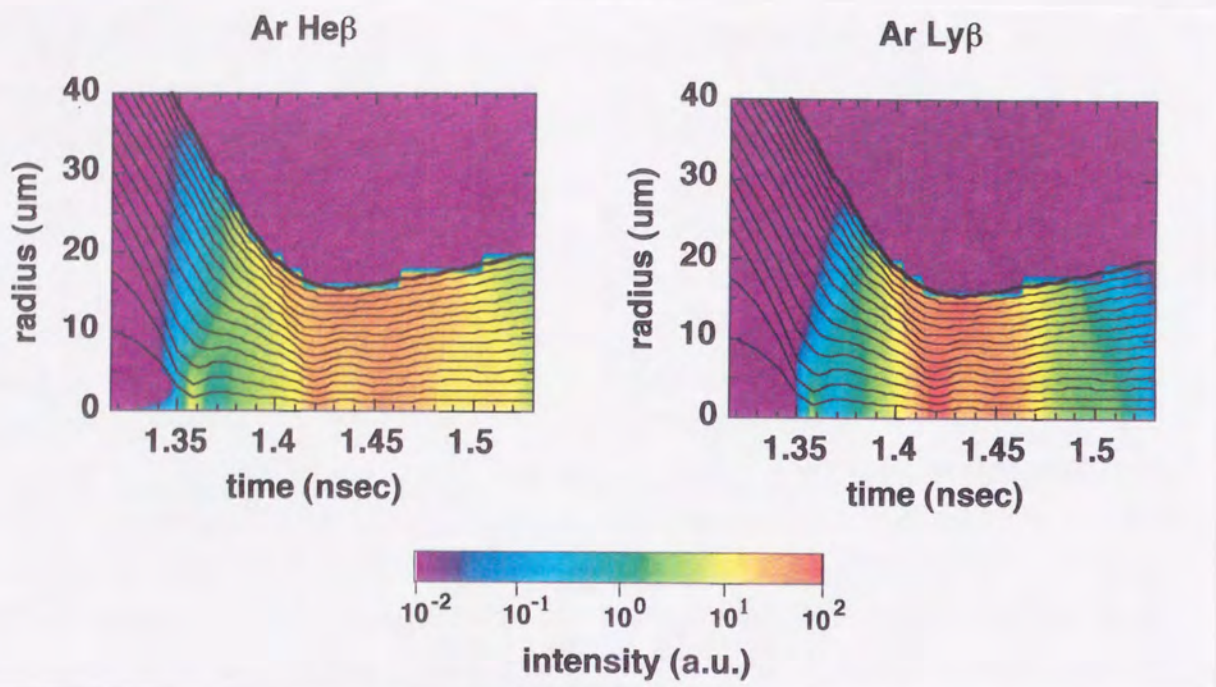

Figure 2-3-1 Temporal variation of argon Heß and Lyß line emission. As the implosion proceeds, heating and cooling process of the hot spark can be seen in marked variation of the emissions. This implies that space- and time-resolving measurements for these line x rays lead to good understanding of formation and collapse of the spark.

help of the RATION dealing with CRE model. This idea bases on condition which the plasma at each position rapidly reaches equilibrium because the plasma is so dense that 1-ps or less relaxation time of collision process is sufficiently short. Figure 2-3-1 shows temporal variation of intensities of argon lines. It is seen that the emission changes dramatically by three orders of magnitude as heating and compression proceed. Shock wave propagation reflects the intense emission. It is clear that spectral, spatial, and temporal resolving measurements of argon line emission enable to know heating (and cooling) mechanism of the hot spark.

2-4 Summary

In this chapter, principle and merits of x-ray spectroscopic diagnosis of hot dense plasmas are described. In summary,

(1) X-ray measurement is useful for evaluation of implosion performances.

- Implosion dynamics can be investigated with x-ray measurement which can resolve information of plasmas spatially and temporally at the same time.
- Spectral resolution can provide temperature and density information of plasmas.

(2) Temperature and density dependence of x-ray line spectra is so strong as to be used as diagnostic tool.

- CRE model can be applied to imploded plasmas.
- Line intensity ratio has strong dependence of electron temperature which can be used for temperature determination.
- Line width due to Stark broadening has electron density dependence which can be used for density derivation.
- These determination should be done carefully in case of plasma having spatial gradients of temperature and density.

(3) Measurement of x-ray line spectra is useful to know implosion dynamics.

- Spatial distribution of line intensity is rapidly changing, which reflects hot spark heating.
- Spectral, spatial, and temporal resolving measurement is essential to know hot spark heating and cooling mechanisms.

In the following chapter, x-ray monochromatic imaging method are introduced and X-ray Monochromatic Camera developed to realize the three resolutions simultaneously are described.

Chapter 3

Spectral, spatial, and temporal resolving measurements with flat and bent crystals

3-1 Introduction

Described in this chapter are developments, specifications, and performances of spectroscopic instruments used in the implosion experiments described in the following chapters. This section discusses three types of resolution which can be ensured by the help of spectroscopic method.

The conclusion of the Ch.2 is necessity of (1) spectral, (2) spatial, and (3) temporal resolving measurements in order to know dynamics of the spark fuel. All these types of resolutions can be obtained as follows.

(1) Spectral resolution

The spectroscopy is often utilized as a useful tool for plasma diagnostics[1]. The spectral resolution can be ensured by the use of, for instance, Bragg reflection with perfect crystal. The Bragg low is expressed as

$$2d\sin\theta_B = n\,\lambda, \quad (n = 1, 2, \ldots), \qquad \text{Eq. 3-1-1}$$

where d is the spacing of net planes of the crystal, θ_B is the Bragg angle, and λ is the wavelength of the x ray (Fig. 3-1-1). Generally speaking, the reflectivity of the first order reflection (n=1) is larger than any other ones of higher order reflections (n=2, 3, ...). That is why the first order reflection is commonly used for diagnostics. According to the Eq. 3-1-1, the wavelength of λ is in the same order of 10 Å corresponding to the spacing of d. This means that

---

[1] for example, R. H. Huddlestone and S. L. Leonard, *Plasma Diagnostic Techniques* (Academic Press, N.Y., 1965).

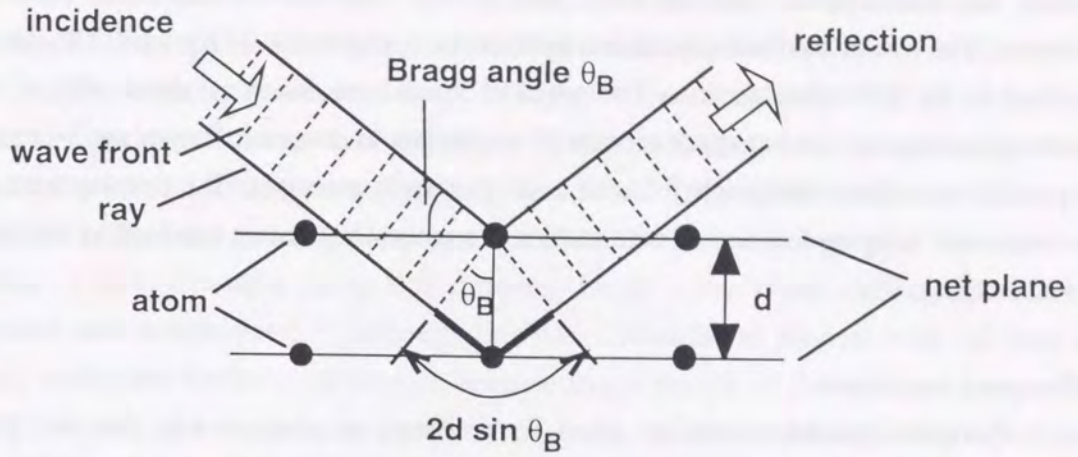

Figure 3-1-1 Bragg reflection.

the wavelength less than about 10 Å (more than 1 keV of the photon energy) can be measured with the Bragg reflection. For the longer wavelength (smaller photon energy), transmission or reflection type of diffraction grating is commonly used.

The use of the perfect crystal gives sufficient spectral resolution. The spectral resolution for the Bragg reflection is derived from Eq. 3-1-1 and its differential,

$$\frac{\lambda}{\Delta\lambda} = \frac{\tan\theta_B}{\Delta\theta_B}, \qquad \text{Eq. 3-1-2}$$

where $\Delta\theta_B$ is the width of the Rocking curve of the crystal. One of features of the perfect crystal such as germanium and silicon is small width of the Rocking curve, which is different from larger one of a mosaic crystal. Hence, with larger Bragg angle and the use of a perfect crystal, one can obtain higher spectral resolution. A typical value of $\lambda / \Delta\lambda$ for our case is about 10^4 which is large enough to resolve line width ranged from 10 to 30 eV at 3 to 4 keV of the photon energy, where the θ_B is 80 degrees and the $\Delta\theta_B$ is 100 μrad corresponding to the integrated reflectivity.

(2) Spatial resolution

Conventional methods to obtain two-dimensional (2-D) images of plasmas emitting x rays are, for instance, use of pinhole, multi-channel plate, zone plate, and total reflection optics, which yield only spectral integrated images. However, efforts were made to develop techniques for spectral resolution, especially with the help of blazed zone plate,[2] synthetical multilayer

---

[2] N. M. Ceglio, et al., Ann. N.Y. Acad. Sci., **342**, 65 (1980).

mirrors,[3] and bent crystals.[4] Among them, bent crystals were chosen due to the high spectral resolution. The use of the bent crystal can provide monochromatic 2-D image. The details are described in the following section. The required spatial resolution is about 10 μm or less because typical size of the hot spark is from 30 to 100 μm in diameter. Regarding 3-D imaging, it is possible to utilize tomography[5, 6] with bent crystals in principle. The development of 2-D monochromatic imaging techniques with sufficient temporal resolution can lead to the next step for 3-D imaging.

(3) Temporal resolution

Temporal resolution can be given by detectors in contrast with the two previous resolutions by the optics. The required temporal resolution can be estimated roughly by means of the attained spatial resolution. Given a typical implosion (shell) velocity of 10^7 cm/s, to know fluid dynamics with spatial resolution of 10 μm, temporal resolution of 100 ps is needed (10 μm is divided by 10^7 cm/s). For 1-μm resolution, 10 ps is needed. For 2-D imaging, gated x-ray framing cameras with resolution of less than 100 ps were developed and used in the

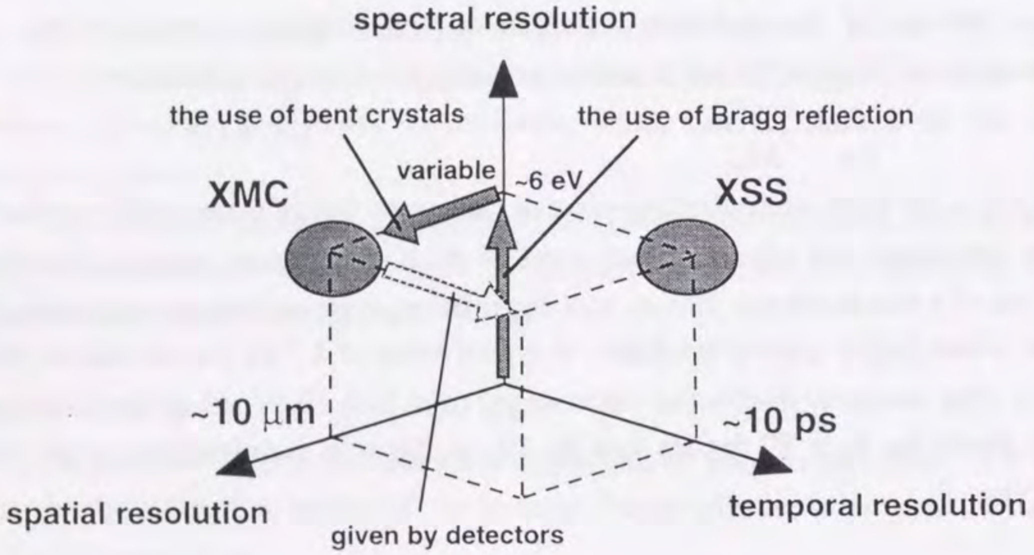

Figure 3-1-2 The three resolutions and instruments. XMC is X-ray Monochromatic Camera described in sec.3-2 and XSS is X-ray Streak Spectrometer in sec.3-3.

---

[3] D. G. Nilson et al., Laser and Particle Beams, **6**, 751 (1988).

[4] E. Förster et al., Laser and Particle Beams, **9**, 135 (1991).

[5] Y. Chen et al., Optics Comm. **71**, 249 (1989).

[6] T. Matsushita et al., Ann. Progress Report, Inst. of Laser Eng., Osaka Univ., 183 (1995).

implosion experiments.[7] Recently fast framing cameras with 35-ps resolution have been developed.[8] If the spatial resolution is about 10 μm, this temporal resolution is sufficient.

Streak cameras are used for 1-D image with the resolution of pico-second level. However, proposed was an new techniques which multi-image on the photocathode of the streak camera and 1-D image sampling can provide 2-D images with temporal resolution.[9] The technique using multi-imaging x-ray streak camera (MIXS) was improved and developed.[10] Besides, a new technique using 2-D sampling image x-ray streak camera (2D-SIXS) was proposed and demonstrated.[11] Although this has a potential to connect with the bent crystal optics, it requires further consideration because magnification of the order of one hundred is needed. As long as a streak camera used in this study, one used in the implosion experiments as not a 2-D imager but one part of a spectrometer described in sec. 3-3.

All these things make it clear that optics using bent crystals coupled with a framing camera or other imager can obtain all these three resolutions simultaneously (Fig. 3-1-2). In the following sec.3-2, development of X-ray Monochromatic Camera (XMC) using bent crystals is described. The principles and features of monochromatic imaging method are explained in 3-2-1. Design of XMC is described in 3-2-2. Development of XMC from technical point of view is described in 3-2-3. Although monochromatic imaging with temporal resolution is not mentioned here, it will be done very soon indeed. In sec.3-3, introduced is brief description of principle and performance of X-ray Streak Spectrometer (XSS) providing temporal variation of x-ray spectra. These diagnostics are used in the implosion experiments described in Chs.4 and 5.

3-2 Development of X-ray Monochromatic Camera (XMC) using bent crystal

3-2-1 Principles and features of x-ray monochromatic imaging

---

[7] M. Katayama et al., Rev. Sci. Instrum. **62**, 124 (1991), D. K. Bradley et al., ibid. **63**, 4813 (1992).

[8] K. Kondo et al., Ann. Progress Report, Inst. of Laser Eng., Osaka Univ., 173 (1995); D. K. Bradley et al., Rev. Sci. Instrum., **66**, 716 (1995).

[9] C. Deeney and P. Choi, Rev. Sci., Instrum. **60**, 3558 (1989); P. Choi and R. Aliaga, ibid. **61**, 2747 (1990).

[10] H. Shiraga et al., Rev. Sci. Instrum., **66**, 722 (1995).

[11] H. Shiraga et al., Rev. Sci. Instrum., **68**, 745 (1997).

Figure 3-2-1 shows schematic drawing of imaging by one- and two-dimensionally bent crystals. Figure 3-2-1 (a) is a scheme of the Johann type monochrometer which is commonly used for crystal structure analysis. In this scheme, 1-D image of an object on the

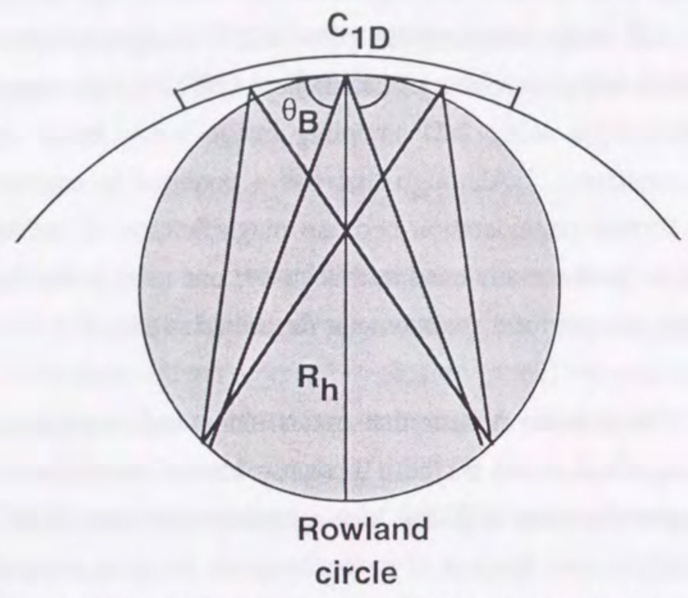

(a) 1-D monochromatic imaging by using of Johann type monochrometer.

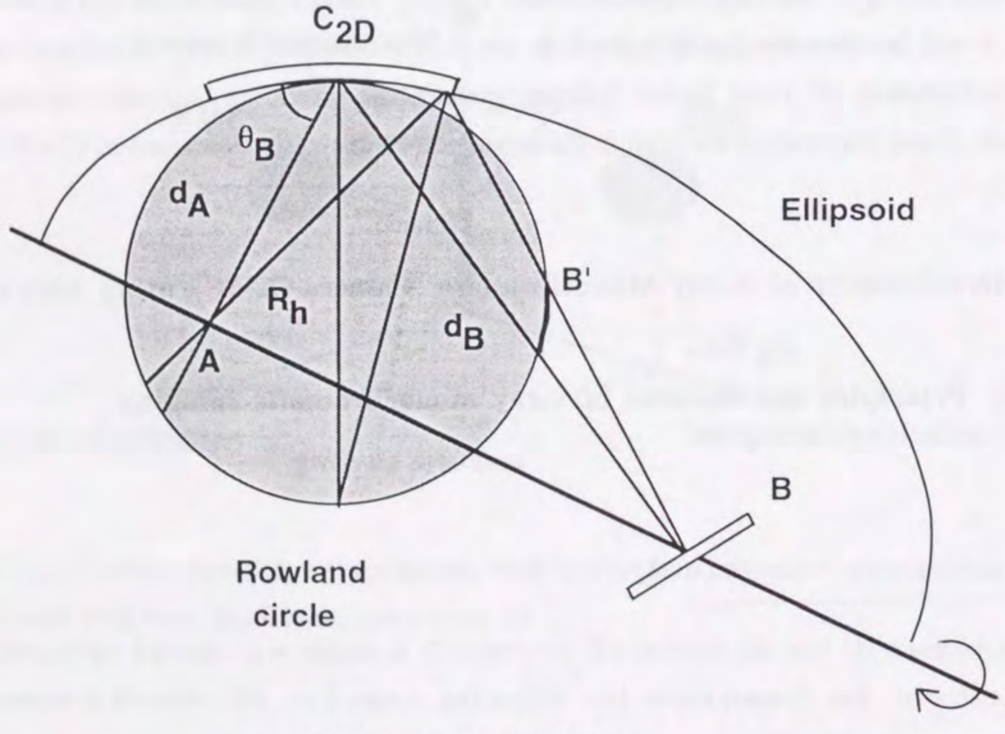

(b) 2-D monochromatic imaging

Figure 3-2-1 Principles of x-ray monochromatic imaging.

Rowland circle is transferred monochromatically to another point on the circle. For 2-D imaging, the bent crystal C_{1D} should be bent along the vertical direction. Figure 3-2-1 (b) shows a scheme of 2-D monochromatic imaging by the help of a 2-D bent crystal; bent net planes of the crystal C_{2D} approximated to an ellipse on the dispersion (horizontal) plane, a source position A, the detector position B' for spectroscopy and B for imaging, Bragg angle θ_B, distance between source and crystal d_A, crystal and detector d_B, and the magnification factor d_B/d_A. To put it exactly, the curvature of the 2-D bent crystal is that of the surface of the ellipsoid with the rotation axis through A and B. Actually, little aberration due to the use of large Bragg angle enable us to use toroidally bent crystal for the imaging. Toroidally bending means that the crystal has two bending radii perpendicular to each other. According to a lens equation,

$$\frac{1}{d_A}+\frac{1}{d_B}=\frac{1}{f_{H(V)}} \quad , \qquad \text{Eq. 3-2-1}$$

where f is the focal length and the subscript H and V mean horizontal (dispersion) and vertical directions respectively. The focal lengths can be expressed as

$$f_H=\frac{R_H\sin\theta_B}{2}, \quad f_V=\frac{R_V}{2\sin\theta_B}, \qquad \text{Eq. 3-2-2}$$

where R_H and R_V are horizontal and vertical bending radii respectively. The relationship between the bending radii is determined from a condition to eliminate astigmatism. Namely, the condition

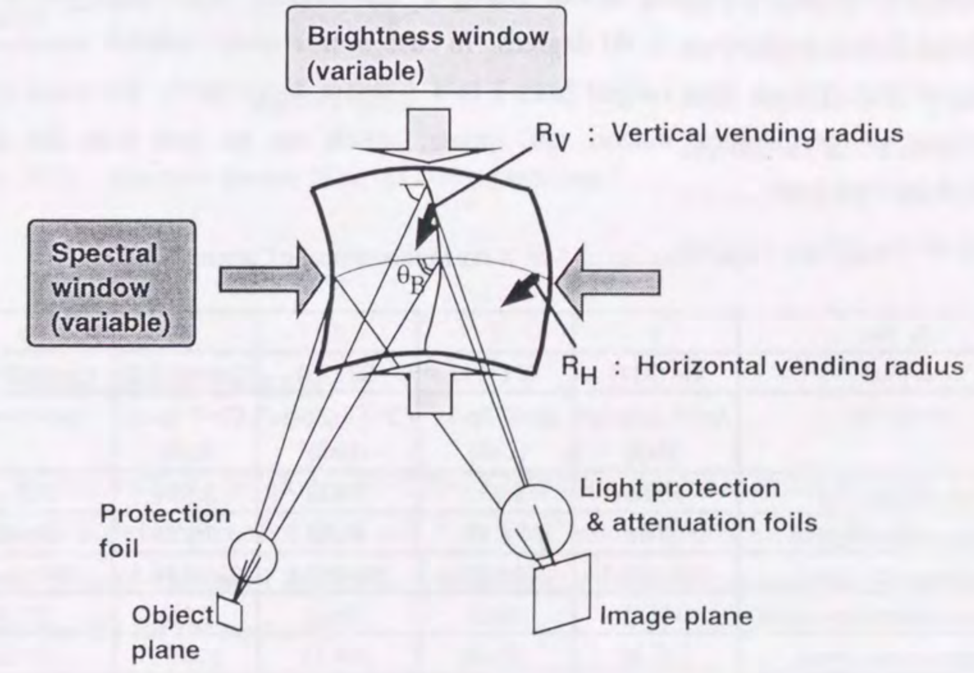

Figure 3-2-2 Structure and features of XMC.

of $f_H = f_V$ can be reduced by Eq. 3-2-2 to

$$\frac{R_V}{R_H} = \sin^2\theta_B \,. \qquad \text{Eq. 3-2-3}$$

This means that the Bragg angle determined from the interest wavelength and the crystal (Eq. 3-1-1) determines the ratio of the bending radii. A crystal should be prepared for an interest wavelength.

Features of the monochromatic imaging method with bent crystals are that bright images can be obtained due to large aperture and that the spectral range and brightness control can be done by changing the aperture (Fig. 3-2-2).

3-2-2 Design of XMC

There are two steps to determine specification of the bent crystal. The first step is to select a crystal for the interest wavelength and the second is to determine the bending radii. After these determinations, polished thin perfect crystals were bent elasticaly. Table 3-2-1 shows specifications of XMC for the experiments descried in sec.4-3.

The first step is selection of the crystal. This corresponds to determination of '2d' in the formula of the Bragg reflection (Eq. 3-1-1). As has been pointed out, larger Bragg angle leads to less aberration. According to Eq. 3-1-1, a '2d' slightly larger than wavelength 'λ' provides large Bragg angle close to 90 degrees. In case of this study, interest wavelengths are those of argon and chlorine lines ranged from 3 to 4 Å (from 3 to 4 keV). The main candidates of the crystals are germanium, silicon, and quartz, which can be bent with the developed techniques described later.

Table 3-2-1 Specifications of 5-ch X-ray Monochromatic Camera (XMC).

ch. No.	1	2	3	4	5
crystal	Ge (311)	Si (311)	Si(220)	Quartz(11.2)	Quartz(10.-1)
x-ray line	Ar^{+16} 1s3p-$1s^2$ (Heß)	Ar^{+17} 3p-1s (Lyß)	Cl^{+16} 1s3p-$1s^2$ (Heß)	Cl^{+17} 3p-1s (Lyß)	continuum
wavelength (Å)	3.366	3.151	3.800	3.534	3.294
Bragg angle (degree)	80.62	74.19	81.70	76.73	80.62
bending radii (mm)	200/194.7	200/185.1	200/195.8	200/189.5	200/194.7
integrated reflectivity (mrad)	316.0	80.8	356.0	82.9	77.6
target-crystal (mm)	107.82	105.02	108.15	106.29	107.82
crystal-detector (mm)	1161.53	1147.99	1163.20	1154.02	1161.53

The second step is to determine the bending radii of the crystal. These are determined from three factors: distance between the plasma and the crystal, detector position, and the Bragg angle. Since the distance and the position fix the image magnification, one should consider the magnification desired simultaneously. To begin with the distance 'd_A' (Fig. 3-2-1), the lower limitations of the distance are to protect the crystal from plasma and to avoid interference with the other diagnostic instruments in an experimental chamber. The distance, however, should be as small as possible for high magnification so that spatial resolution of the imaging system combined that of crystal optics with that of the detector is not limited by that of the detector. In this case, the distance was determined to be about 100 mm. Then, the detector position was determined from the distance d_A and the magnification so that it is outside of the 900 mm-diameter chamber. Next, one can determine one of bending radii, and the other can be fixed by means of Eq. 3-2-3 with the Bragg angle. The bending radii of the crystal were about 200 mm.

It is useful to quote excellent technique of crystal bending which was developed at Jena, Germany.[4] The schematics drawing is shown in Fig. 3-2-3. Convex glass forms with toroidal surfaces can be produced by optical manufacturing with an accuracy of fractions of the wavelength of visible light. Between this form and the thin crystal plate, an optical contact without Newton fringes must be achieved by very clean surfaces. A crystal holder is glued with a specially developed epoxy glue, on the reverse of the crystal plate for fixing the curved crystal form. After separation of glass form and crystal, which is now fixed to the crystal holder, the crystal is a concave replica of the glass form.

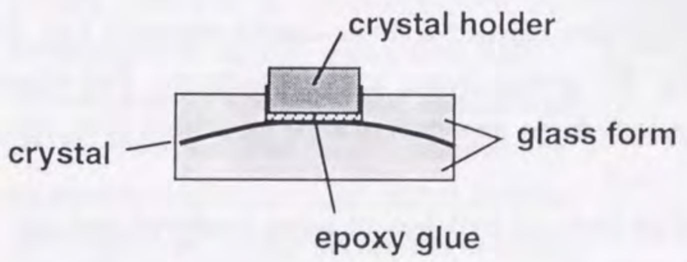

Figure 3-2-3 Schematic drawing of crystal bending technique.[4]

3-2-3 Development of XMC

In this section, development of the XMC from technical points of view is described. Main content is development of 2-ch and 5-ch XMC realizing precise adjustment mechanism of the crystal. A new scheme of the use of double bent crystals improving the spatial resolution is mentioned briefly for the next step.

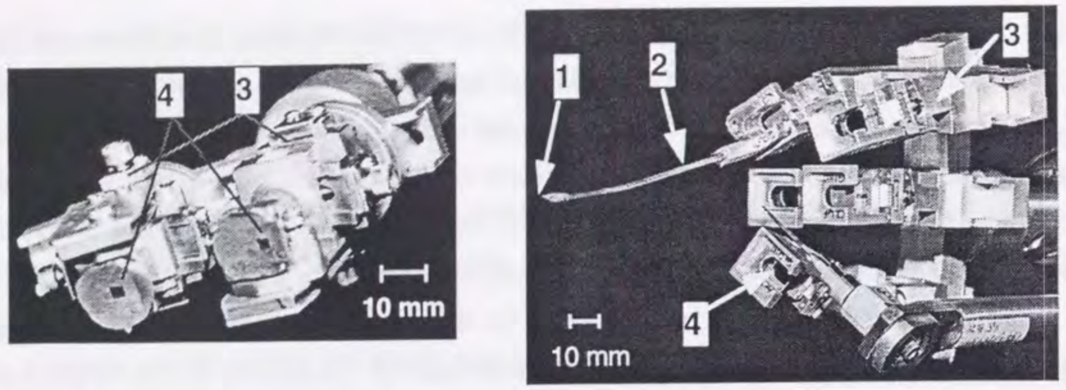

(a) Two-channel X-ray Monochromatic Camera (1993)

(b) Five-channel X-ray Monochromatic Camera (1996)

Figure 3-2-4 2ch-XMC and 5ch-XMC developed and used in the implosion experiments.
1. target position, 2. needle for crystal alignment, 3. miniature goniometer, 4. bent crystal.

Precise adjustment mechanism of the crystal is very important to obtain monochromatic images successfully. The accuracy of the Bragg angle adjustment is needed within 0.1 degrees, which is calculated by raytracing code.[4] In addition, alignment of the toroidally bent crystal should be done with the accuracy for six freedom consisting of three orthogonal axes and three rotation along each axis. These demands were satisfied with the camera shown in Fig. 3-2-4, and miniature goniometers were used for precise Bragg angle adjustment. The alignment procedures and configuration of the crystals are so important as to be introduced in an appendix of this report.

Figure 3-2-4(a) is 2ch-XMC for Heß and Lyß lines of argon seeded in fuel gas. This camera was introduced to diagnosis of hot spark created by x-ray driven implosion.[12] The specification was the same as two argon channels in Table 3-2-1 except the bent crystal size. The crystal size was 14 mm in diameter. Detectors not shown here were calibrated x-ray films (Fuji MI-FX).[13] Two individual films were exposed and developed for the two images shot by shot. The results and discussion of the data are described in sec. 4-2.[14]

Figure 3-2-4 (b) is 5ch-XMC for Heß and Lyß lines of chlorine and continuum (at wavelength without line) in addition to the two argon lines.[15] The objects of the addition of chlorine and continuum channels are to measure pusher/fuel mixing directly and to subtract contribution of continuum x rays to the other monochro-images as background. The

---

[12] I. Uschmann et al., Rev. Sci. Instrum. **66**, 734 (1995).

[13] K. Kondo et al., J. Appl. Phys. **67**, 2693 (1990).

[14] K. Fujita et al., J. Electron Spectroscopy and Related Phenomena **80**, 291 (1996).

[15] M. Vollbrecht et al., J. Quant. Spectrosc. Radiat. Transfer, in press.

specifications of 5ch-XMC are described in Table 3-2-1. Geometry of the 5ch-XMC is basically the same as in the previous version of the 2-ch XMC. Major improvements are four as follows.

(1) Down-sizing of the crystal and its mounts was done so as to avoid mechanical interference with neighboring diagnostic instruments in the experimental chamber. The size of the new crystal was 6 mm in diameter.

(2) A x-ray CCD (charge coupled devise) camera was used as a detector instead of films. The CCD camera system[16] is useful to see and analyze obtained images quickly after a shot. Moreover, the relative sensitivity and linear-dynamic range are much larger than those of the film by 1-3 and one order of magnitude respectively.[6]

(3) The crystal alignment procedure with which one can easily set all images within a detectable area avoiding image overlapping. The use of miniature goniometers as crystal mounts and needles for the alignment satisfied the demands by the help of improved mechanism and optimized configuration of the crystals.

(4) Accuracy of optics alignment using visible light was improved. Since the bent crystal is manufactured so as to make the lattice surface parallel to its physical surface, the crystals can be aligned with visible light.[17] To ensure the crystal alignment, orientations of the two surfaces were evaluated by measuring displacement of optical (visible light) and x-ray image points. An example is shown in Fig. 3-2-5. Figure 3-2-5(a) is an x-ray backlit image of a 100 μm/pitch grid recorded with x-ray film and (b) is the corresponding visible image. A metallic needle was set to point the image origin. A small displacement is seen. The measured angular difference of 1 mrad is small enough to attain the image pointing with 1 mm accuracy at the detector plane of x-ray CCD (27.9 x 25.9 mm). It is important to know the displacements especially when smaller detectable area such as 5 mm-wide microstrip line of a framing camera is used.

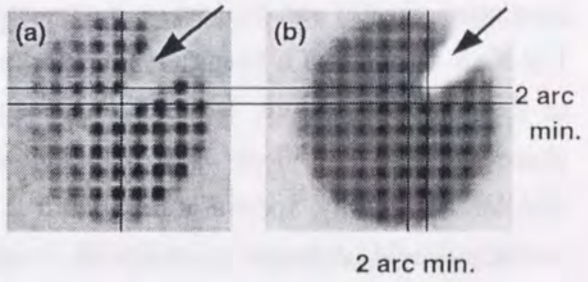

Figure 3-2-5 (a) visible light and (b) x-ray backlit image of a 100 μm/pitch grid with a shadow of a needle (an arrow). The displacement is 2 arc min. for horizontal and vertical directions in this case.

The 5-ch XMC developed was used in a x-ray driven implosion experiments. The

---

[16] produced by Princeton Instruments.

[17] E.Förster et al., J. Quant. Spectrosc. Radiat. Transfer. **51**, 101 (1994).

results are mentioned in sec.4-3. These developments can contribute to next step of installation of temporal resolution on going.

Further development of XMC is to improve spatial resolution. Proposed was the use of double bent crystals to reduce spherical and coma aberration.[18] In the Ref.18, 3-μm resolution is achieved and the raytracing code predicts resolution of less than 1 μm. Another merit of the double crystal scheme is to use only one diagnostic port at the experimental chamber in contrast with two port needed in the current one-crystal scheme. This can reduce difficulty of the precise alignment procedures.

3-3 X-ray Streak Spectrometer (XSS) using flat crystal

In this section, X-ray Streak Spectrometer using a flat crystal is mentioned. It has been developed already and is used as a standard diagnostic instrument in implosion experiments. The XSS consists of a Bragg crystal spectrometer coupled with a compact x-ray streak camera as illustrated in Figure 3-3-1. To detect tiny emission from seeded materials, the streak photocathode is set 50 cm apart from the plasma. The spectral dispersion crystal is set at the middle. An energy spectral range from 2.8 to 4.5 keV is covered by the use of RbAP (Rubidium acid phthalate) crystal (100) having 26.121 Å of 2d[19] to observe hydrogen-like and helium-like resonance and lithium-like satellite lines from argon and chlorine.

Time-resolution of this instrument is given mainly by two factors: time spread due to finite slit-cathode width (Δt_1) and velocity spread of photo electrons given as a function of acceleration voltage (Δt_2).[20] Assuming a Gaussian spread function, the overall resolution is given as

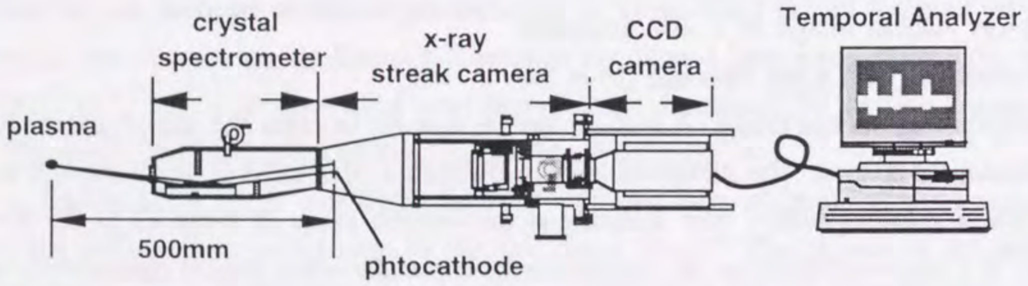

Figure 3-3-1 The x-ray spectrograph system having 10-ps time resolution. Energy spectral range from 2.8 to 4.5 keV is covered by RbAP crystal.

$$\Delta t = \sqrt{(\Delta t_1)^2 + (\Delta t_2)^2}. \qquad \text{Eq. 3-3-1}$$

For a 100-μm slit-cathode, we may expect $\Delta t \sim 10$ ps for an acceleration voltage of 5 kV and a gold cathode.[21]

Energy-resolution is given by three factors: energy resolutions defined by an integral-refractivity of the Bragg crystal ($\varepsilon_1/\Delta\varepsilon$), source size ($\varepsilon_2/\Delta\varepsilon$), and spatial-resolution power of the detector ($\varepsilon_3/\Delta\varepsilon$) will give the total resolution as

$$\frac{\varepsilon}{\Delta\varepsilon} = \sqrt{\left(\frac{\varepsilon_1}{\Delta\varepsilon}\right)^2 + \left(\frac{\varepsilon_2}{\Delta\varepsilon}\right)^2 + \left(\frac{\varepsilon_3}{\Delta\varepsilon}\right)^2}. \qquad \text{Eq. 3-3-2}$$

One can obtain $\varepsilon_3/\Delta\varepsilon \sim 220$ for RbAP crystal, 50 μm source extent, and 100 μm on the photocathode slit.

This instrument is used for implosion experiments described in the following chapters.

3-4 Summary

In this chapter, spectral, spatial, and temporal resolving measurement method was described. X-ray Monochromatic Camera (XMC) and X-ray Streak Spectrometer (XSS) are developed for diagnosis of imploded plasmas. In summary,

(1) X -ray monochromatic imaging method can give three kinds of resolution of spectral, spatial, and temporal ones simultaneously.

- Spectral resolution is sufficiently obtained by the use of perfect crystal.
- Spatial resolution is sufficiently obtained by toroidally bent crystal.
- Temporal resolution is sufficiently obtained by a fast imager such as the framing camera developed.

(2) XMC based on the monochromatic imaging method by the help of crystal bending techniques was developed.

- The Johann type monochrometer was applied to 2-dimensional (D) monochromatic imaging.
- Toroidally bent crystal can provide 2-D image suppressed astigmatism.

---

[18] E. Förster et al., SPIE **2523**, 140 (1995).

[19] A. Burek, Space Science Instrumentation **2**, 53 (1976).

---

[20] V. V. Korobkin et al., J. Photogr. Sci. **17**, 179 (1969).

[21] B. L. Henke et al., J. Appl. Phys. **52**, 1509 (1981).

- Bright image of the plasma can be obtained due to the large aperture.
- Spectral range and brightness of image are variable.
- 2-ch XMC for Heß and Lyß lines of argon was developed.
- 5-ch XMC for Heß and Lyß of chlorine and continuum added to the argon lines was developed.

(3) XSS can provide spectra of argon and chlorine lines with sufficient temporal resolution.

Described in the following chapters are implosion experiments by the use of these spectroscopic instruments for diagnosis of imploded plasmas.

Chapter 4

Fuel temperature mapping and pusher/fuel distribution measurements in x-ray driven implosion experiments

4-1 Introduction

In this chapter, described are that the XMC were applied to x-ray driven implosion experiments, and analysis and discussions of the obtained data. Clarified is that usefulness of the XMC for direct measurements of pusher/fuel mixing was demonstrated.

It is of great importance to understand influence of hydrodynamic instabilities occurring during spherical convergence of the fusion pellet which may result in discrepancies in neutron yields and spectroscopic measurement results between the experiments and model predictions.[1, 2] It was deduced from this study that the implosion proceeds safely until the beginning of the deceleration phase but further compression at the stagnation phase collapses due to fluid mixing occurring at the contact surface of the pusher/spark fuel. Further study, therefore, has been needed to know the detailed structure of the compressed fuel. For this purpose, x-ray monochromatic cameras (XMC) using toroidally bent crystals were developed (Ch.3). They can provide two-dimensionally (2-D) space-resolved not only hot spark and pusher distributions but also electron temperature distributions of them as a novel diagnosis.[3]

---

[1] H. Nishimura et al., *Proceedings of 14th Int. Conf. on Plasma Physics and Controlled Fusion Research*, Würzburg, Vol. 3, IAEA, Vienna, 1993, p. 97.

[2] H. Nishimura et al., Phys. Plasmas **2**, 2063 (1995).

[3] I. Uschmann et al., Rev. Sci. Instrum. **66**, 7344 (1995).

Table 4-2-1 Specifications of the 2-ch XMC used in the experiments.

	Si (311)	Ge (311)
Observation line	Ar^{+17} Lyß	Ar^{+16} Heß
Photon energy /keV	3.930	3.678
Bragg angle /degree	74.2	80.6
Horizontal bending radius /mm	198.7	199.8
Vertical bending radius /mm	185.9	194.5
Magnification	11.9	12.0
Spectral window $\Delta\lambda/\lambda$ of the crystal	4.6×10^{-3}	3.0×10^{-3}

In sec.4-2, temperature mapping of the hot spark with monochromatic images for argon lines are described. The 2-ch XMC was used in the x-ray driven implosion experiments. Consistency of the experimental data obtained with the 2-ch XMC and a calibrated spectrometer was confirmed. In addition to discussion for the obtained images, comparison with simulation results is described (sec.4-2-2). In sec.4-3, Pusher/fuel distribution measurements with monochro-images for Ar and Cl lines are briefly mentioned. In this x-ray driven experiment, the 5-ch XMC was used to record distributions of both pusher and fuel simultaneously.

4-2 Fuel temperature mapping with monochro-images for Ar lines

4-2-1 Experiments and results

In this section, demonstration of temperature mapping of hot spark with monochromatic images for argon lines are described. To obtain the monochro-images, the 2-ch XMC developed was used in the x-ray driven implosion experiments.

Experiments were performed using the GEKKO XII Nd:glass laser. A laser pulse of 5 kJ energy and 351-nm wavelength was focused with a two-bundle illumination system. The pulse waveform was an Gaussian with a full width at half maximum (FWHM) duration of 0.75 nsec. Figure 4-2-1 shows the configuration of the x-ray-driven fusion target and laser beams. The geometry was chosen to minimize asymmetries with 3D illumination calculation code.[4]

---

[4] M. Nakamura et al., Laser and Particle Beams **10**, 421 (1992).

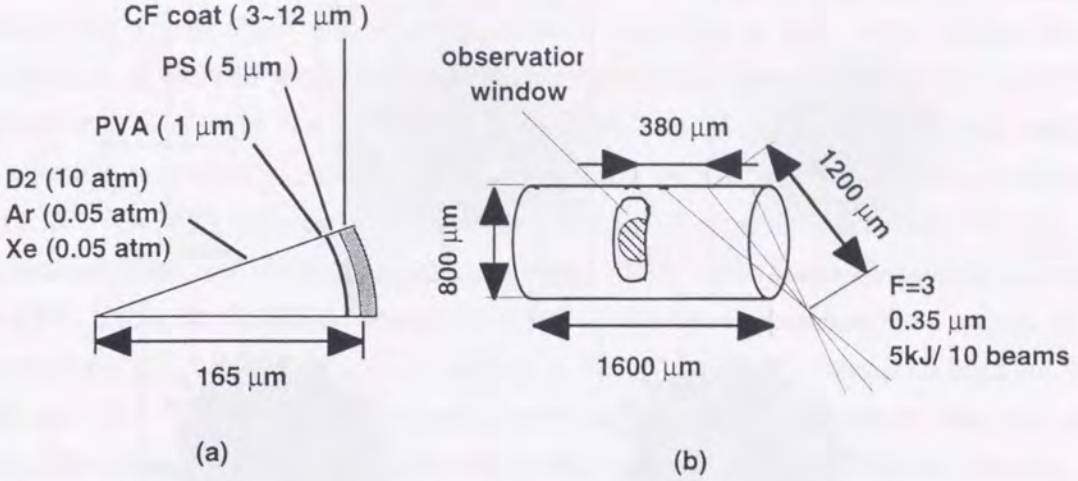

Figure 4-2-1 The configuration of the x-ray-driven fusion target and laser beams: (a) CF-coated PS PVA shell; (b) cylindrical cavity made of gold.

Cylindrical Cannonball targets were used. The cylindrical Cannonball target consisted of a cylindrical cavity made of gold to convert laser to x rays and confine them in it, and a fuel capsule. The inner diameter and the length of the cylinder were 800 and 1600 μm respectively, and wall thickness of the cylinder was 10 μm. The cylinder had an observation window on the side wall. The window was covered with polystyrene film to keep gold plasmas away from line of the observation. The fuel capsule was set at the center of the cylinder cavity. Plastic shells were used as the fuel capsule. A typical capsule shell had a 160 μm inside diameter, 9 to 18 μm wall, and consisted of three layers. The inner layer is 1-μm thick polyvinylalcohl (PVA) to contain deuterium fuel, argon and xenon gas. Xenon gas was test in this experiment. The middle layer was 6-μm thick polystyrene (PS). The outer layer was 3 to 12-μm thick polytetrafluoroethylene (so called Teflon $CF_{1.3}$) as an x-ray absorber and ablator. The variation of the CF coat thickness control implosion behavior from a stagnation-free mode to a high compression mode with high radial convergence at the stagnation phase.

Imploded core plasmas were diagnosed by x-ray spectroscopic method. 2-ch X-ray monochromatic camera (2-ch XMC) to obtain two-dimensional space-resolved monochro-

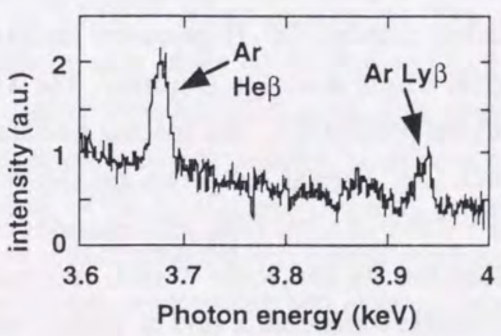

Figure 4-2-2 Typical space-averaged Ar spectra from the compressed core.

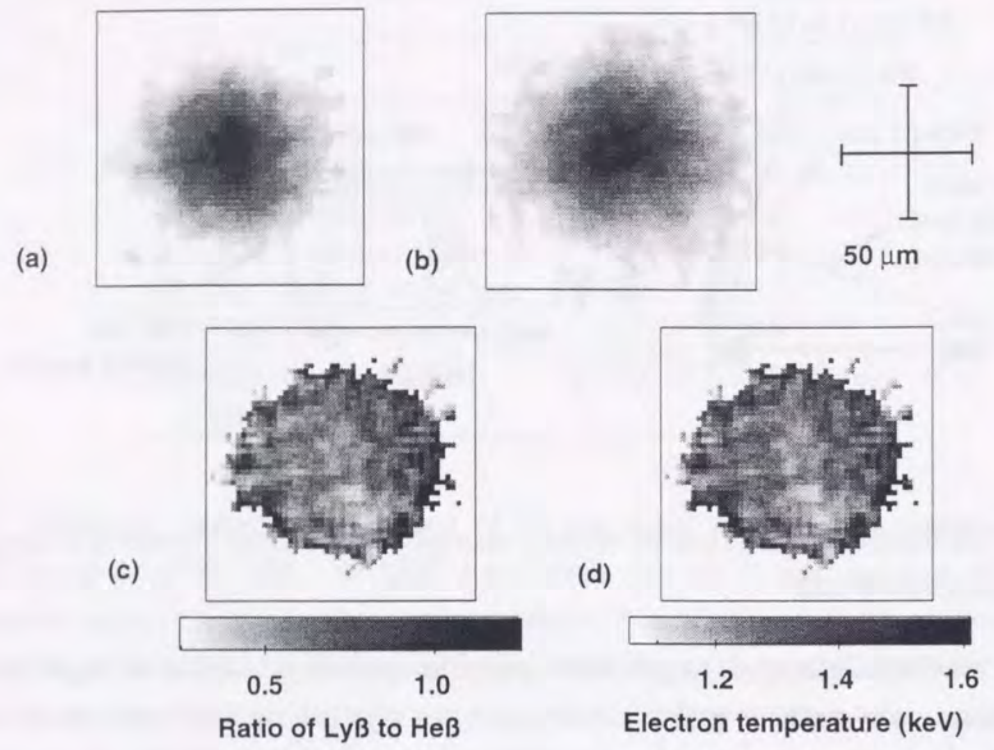

Figure 4-2-3 Typical experimental results:(a) monochromatic images of Ar Heβ line, (b) Lyβ line, (c) intensity ratio of Lyβ/Heβ and (d) electron temperature.

matic images at Ar Heβ and Lyβ lines respectively and x-ray flat-crystal spectrometer (XCS) to obtain spatial integrated Ar spectra were used simultaneously. They were measured in a time-integrated manner with absolutely calibrated Fuji MI-FX films[5]. The XMC utilizes Bragg reflections of toroidally bent crystals: Ge(311) for Ar Heβ line and Si(311) for Lyβ line. The specifications are listed in Table. The spectral window is about 300. High quality toroidally bent crystals have been produced with the results of grate efforts at Jena in Germany. The XCS also utilizes Bragg reflections of flat crystal pentaerythritol (PET(002)). The spectral resolution $\varepsilon/\Delta\varepsilon$ at Lyβ line is about 3000 mainly due to finite source size. Typical Ar spectra are shown in Fig. 4-2-2. The images can be absolutely calibrated by γ-curve of x-ray film, transmissions of filters, aperture angle of XMC, reflectivities of the crystals and the line width of each spectrum.[3] The calibrated monochromatic images, however, still contain continuum x rays as background. This background was subtracted, assuming that the intensity ratio of line to continuum is constant at all spatial positions by referring experimental data from XCS. The typical monochromatic

---

[5] K. Kondo et al., J. Appl. Phys. **67**, 2693 (1990).

images after this correction are shown in Fig. 4-2-3(a) Heβ line and (b) Lyβ line. Figure 4-2-3 (c)shows the spatial distributions of line intensity ratio Lyβ to Heβ, which reflect the spatial distributions of electron temperature. It was confirmed that space-averaged line intensity ratio obtained with XMC and that with XCS for the same laser shot are consistent with each other. The electron temperature and density were extracted by the help of spectrum analysis code RATION[6]. RATION code produces K-shell spectra with a steady state kinetics model, taking into account Stark and electron-impact broadening under LTE (Local Thermal Equilibrium) or non-LTE. Using the RATION, the space-averaged electron temperature for a typical shot was estimated about 1.3 keV. The electron density of 3×10^{23} cm^{-3} was determined from Ar Heβ line width and used in the electron temperature estimation because the intensity ratio has not only strong dependence of electron temperature but also weak dependence of electron density. Using this density, a temperature map (Fig. 4-2-3 (d)) of core plasma was obtained from the ratio distribution (Fig. 4-2-3 (c)). It is seen in Fig. 4-2-3 (d) that four cooler spots looking like a four-leaf clover of nearly 25 μm diameter near the center of the core. Such a mode number of 4 asymmetry structure may be resulted from the illumination asymmetry caused from the present capsule irradiation geometry.

4-2-2 Comparison with 1-D simulation results

Postprocessing outputs from one dimensional implosion code ILESTA-1D[7] by the help of RATION[6] was made in order to compare the experimental data with the simulation results directly and accurately. In the experiments, two-dimensional space-resolved monochromatic images of Ar Heβ and Lyβ lines and spatial integrated Ar spectra were measured in a time-integrated manner. To compare them with the simulation results, postprocessing ILESTA-1D by the help of RATION which consists of three steps were made and used. The first step is to make intensity data tables of Ar Heβ and Lyβ line as a function of electron temperature and electron density with RATION code. This table is shown in Ch.2. In use of RATION, plasma size is set to minimum as possible so as to assume the core plasma is optical thin. In fact, the optical depth of the Ar Heβ and Lyβ lines for imploded core plasmas were estimated 0.3~0.5.[2] Next is to obtain temporal and spatial evolution of the Ar line emission. That was made by replacing electron temperature and electron density at each time and zone from ILESTA-1D to

---

[6] R. W. Lee et al., J.Quant.Spectrosc.Radiat.Transfer **32**, 91 (1984).

[7] H. Takabe et al., Phys. Fluids **31**, 379 (1988); H. Takabe and T. Nishikawa, J.Quant.Spectrosc.Radiat.Transfer **51**, 379 (1994).

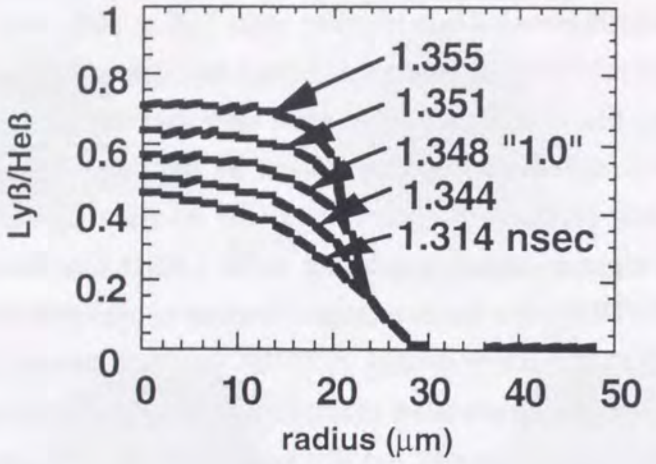

Figure 4-2-4 One of the postprocessed simulation results. Intensity ratio is rapidly changing at around the time marked "1.0" corresponding to the beginning of the deceleration phase.

the Ar line emission with the intensity data tables. Final is to take ray-trace and temporal resolution of the instrument into account. The ray-trace is simple summation of the intensities along the sight because of optical thin core plasma for the Ar lines described above. As XMC used in the experiments has no temporal resolution due to use of films, the expected monochromatic images are produced by time-integrated images after ray-trace.

According to these temporal evolution of expected monochromatic images, the intensities are stronger and stronger till maximum compression because intensities of Ar line emission are strong functions as electron temperature. Hence the experimental images may reflect achieved maximum electron temperature although the images were measured in time-integrated manner. Furthermore, temporal evolution of the ratio Lyβ to Heβ are rapidly changing at around final phase of implosion (Fig. 4-2-4), which is useful for evaluating the implosion performance.

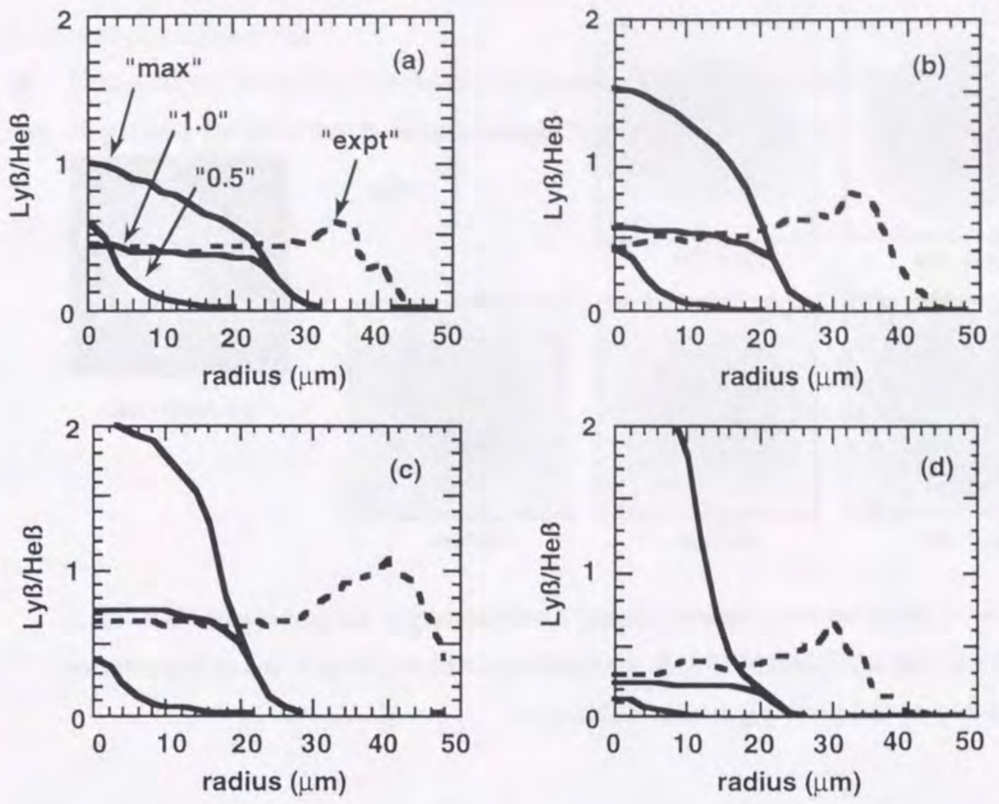

Figure 4-2-5 Ratio distributions experiments(dashed line) vs. simulations (solid lines). (a)Initial areal density of the shell is 1.37 mg/cm^2,(b) 1.94, (c)2.45 and (d) 3.40.

Figure 4-2-5 shows distributions of the line ratios averaged over azimuthal direction around the center of the core which is measured in the experiments and simulation, for four different initial areal densities of the shells corresponding to different ablator thickness. The experimental results have remarkable profiles for all shots that are relatively flat in the inner region of the profiles but higher in outer region than in inner. On the other hand, the simulation results are shown as three profiles for each shot : one is marked "0.5" which is a time-integrated value till the time that the convergent shock wave front first comes to the center of the fuel, the other is "1.0" till first bounce and the other is "max" till maximum compression respectively. The experimental results in inner region correspond to this label "1.0" of the simulation results. If the implosion process is assumed to be terminated at a moment, this comparison suggests one possibility that the fuel is stably compressed until the beginning of pusher deceleration marked "1.0". In outer region, the experimental profiles are very different to the simulated one. One possibility of the existence of the higher region is that shock waves reflected from the center core (at "0.5") propagate into perturbed contact surface region ("1.0") and the temperature increases locally due to numerous local reflections of shock waves. This mechanism should be researched experimentally and theoretically. But the results depend also upon how to subtract continuum x-ray component. Their intensity distribution should be measured experimentally. For this purpose, another channel of XMC for slightly different wavelength including no line was added in the 5-ch XMC.

4-3 Pusher/fuel distribution measurements with monochro-images for Ar and Cl lines

A new series of indirectly driven fusion experiments have been done. The GEKKO

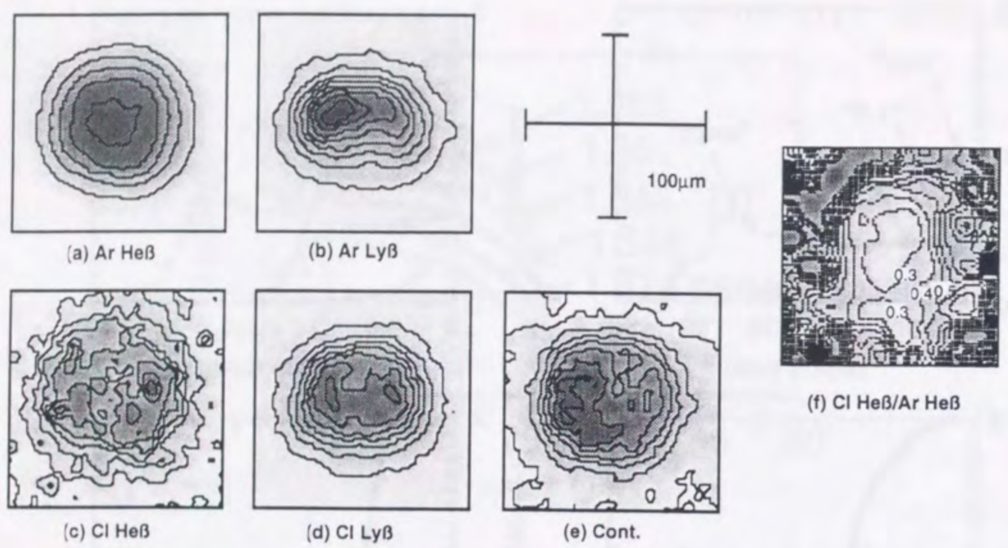

(a) Ar Heß (b) Ar Lyß (c) Cl Heß (d) Cl Lyß (e) Cont. (f) Cl Heß/Ar Heß

Figure 4-3-1 Monochromatic images measured simultaneously by the five-channel XMC. (a) Ar Heβ, (b) Ar Lyβ, (c) Cl Heß,(d) Cl Lyβ, (e) continuum at hv = 3.76 keV, and (f) intensity ratio of Cl Heß to Ar Heß providing material distribution.

XII Nd:glass laser was used as well as the previous experiments. A laser pulse of 5 kJ energy and 351-nm wavelength was focused with a two-bundle illumination system. The pulse waveform was an near-square with a full width at half maximum (FWHM) duration of 0.8 ns and rising time of 0.2 ns. The imploded target was a CH shell of 354 μm in diameter and 4.7 μm in thickness. This was overcoated with 5.95 μm-thick C_2H_3F as an ablator and 0.03 μm-thick aluminum as a seal for the fuel gas. The shell retained a deuterium-argon mixture gas and chlorine (3 at%) in the inner most side of pusher as dopants. Other experimental conditions are similar to those in the previous experiments. Figure 4-3-1(a-e) show an example of five images taken simultaneously in a time-integrated manner and (f) shows the intensity ratio of Cl Heß to Ar Heß to provide material distribution. The monochromatic images reflect low-mode nonuniformities (ℓ = 2 and 4) of the x-ray drive. Material distribution was obtained from the intensity ratio of Cl Heß to Ar Heß. Figure 4-3-1(f) represents the Ar rich region at the core center surrounded by the Cl rich region.

4-4 Summary

In this chapter, demonstration of x-ray monochromatic imaging method with the XMC for the imploded plasmas are described. In summary, usefulness of XMC for imploded plasma

diagnostic was demonstrated.

- Consistency with other calibrated measurements was conformed.
- Separated measurements of pusher and fuel became possible.

Chapter 5

Stability investigation in direct-driven implosion experiments

5-1-1 Introduction

In this chapter, stability investigation in direct-driven implosion experiments. Since the amplified perturbations due to instabilities finally degrades hot spark formation via pusher-fuel mixing, for instance, dependence of the performances (measured by neutron yield, density and temperature of the compressed core) on surface roughness of the pellet were investigated for x-ray driven implosion experiments,[1,2] in which the implosion performances were evaluated by time-resolved x-ray spectroscopic measurements of dopants such as argon in fuel gas and chlorine or titanium at the inner most layer of pusher. However, little study has been made to investigate dependence of the performance on irradiation non-uniformity despite that it is another important factor for the stable compression.

Described here are a dependence of the implosion performance on low modal irradiation non-uniformity (sec.5-2) and investigation of implosion stability for uniform irradiation case (sec.5-3) by means of time- and space-resolving x-ray spectroscopic measurements.

5-2 Dependence of implosion stability on low modal irradiation non-uniformity

In this section, after describing a dependence of the implosion performance on low modal irradiation non-uniformity, experimental data are compared with predictions by a hydro-mix model.[3] A brief description of the mix model can also be found in Ref. 4. The model consists of 1-dimensional (1-D) radiation hydrodynamic code simulations, analysis of hydrodynamic instabilities, and postprocessing by an atomic code to provide synthetic argon K-shell line emissions.

5-2-1 Experiments

The Nd:glass laser system GEKKO XII[5] was used as a driver for the direct-drive implosion experiments. High irradiation-uniformity on a fusion pellet has been achieved by the use of partially coherent light (PCL) generated by fiber optics, precise controllers for power balance among twelve beams, and improved random phase plates.[5] The waveform of the drive pulse has a flat-top shape with 50-ps rise and 1.6-ns duration. Stable implosion was attained with the sharp rise pulse at the acceptable expense of implosion performance.[4]

To investigate dependence of the implosion performance on low modal drive non-uniformity, experiments were made under two different irradiation conditions : one is power-balanced irradiation (estimated irradiation non-uniformity σ_{rms}= 1.9%). The other is imbalanced irradiation where power of two opposing beams from the twelve beams was increased by 20% with respect to the average power of remaining ten beams so as to produce a mode $\ell = 2$ irradiation non-uniformity (σ_{rms}= 10.2%). The former is called balanced case and the latter is imbalanced case hereafter. In both cases, all the PCL beams were focused onto a spherical target by focusing lenses of f-number 3.2 through the random phase plates.[6] The focal condition was set to be d/R= -4 where d is the distance between the target center and the light focal point, R is the radius of the target, and the minus sign means that the focus point is set beyond the target center. Total energy of laser beams at the second harmonic wavelength (526 nm) was about 1.62 kJ on target, yielding incident laser intensity of 1×10^{14} W/cm^2.

Polystyrene shell targets having a very smooth surface were used.[7] Diameter of the shell was 500 μm and its thickness was typically 8 μm. Deuterium gas of 30 atm was filled in the shell with argon dopant of 0.075 atm for the spectroscopic measurement.

The x-ray streak spectrometer was used to detect time-resolved argon spectra. This spectrometer consisted of a flat rubidium acid phthalate (RbAP) Bragg crystal spectrometer coupled with a compact x-ray streak camera (see Ch.4). The temporal resolution was about 10

---

[1] T. R. Dittrich et al., Phys. Rev. Lett. **73**, 2324 (1995).

[2] B. A. Hammel et al., J. Quant. Spectrosc. Radiat. Transfer **51**, 113 (1994).

[3] H. Azechi et al., Annual Progress Report of 1995, Inst. of Laser Eng. Osaka Univ., 157 (1996).

[4] K. Mima et al., Phys. Plasmas **3**, 2077 (1996).

[5] M. Nakatsuka et al., *proceedings of 12th Int. Conf. on Laser Interaction and Related Plasma Phenomena*, (AIP Press, New York, 1996), **2**, 963.

[6] Y. Kato et al., Phys. Rev. Lett. **53**, 1057 (1984).

[7] M. Takagi et al., J. Vac. Sci. Technol. A **9**, 2145 (1991).

ps and energy resolution was 6 eV. The photocathode of the streak camera was made of gold for the balanced case and CuI for the imbalanced case. The latter cathode has four times higher quantum efficiency than the gold cathode for the energy range covered by the spectrometer.[8]

Figure 5-2-1 (a) shows the observation results for the balanced drive case and (b) for the imbalanced drive case. For both cases, we could observe Ar $^{+17}$ Lyβ (3p-1s), Ar $^{+16}$ Heβ (1s3p-1s^2), Ar $^{+16}$ Heγ (1s4p-1s^2) lines, and Li-like satellite lines (1s2l3l'-1s^{2}2l) at slightly lower energy side of Heβ. In addition to temporal variation of these line emissions, discussed here are the intensity ratio of Lyβ to Heβ and that of the satellites to Heβ which also have

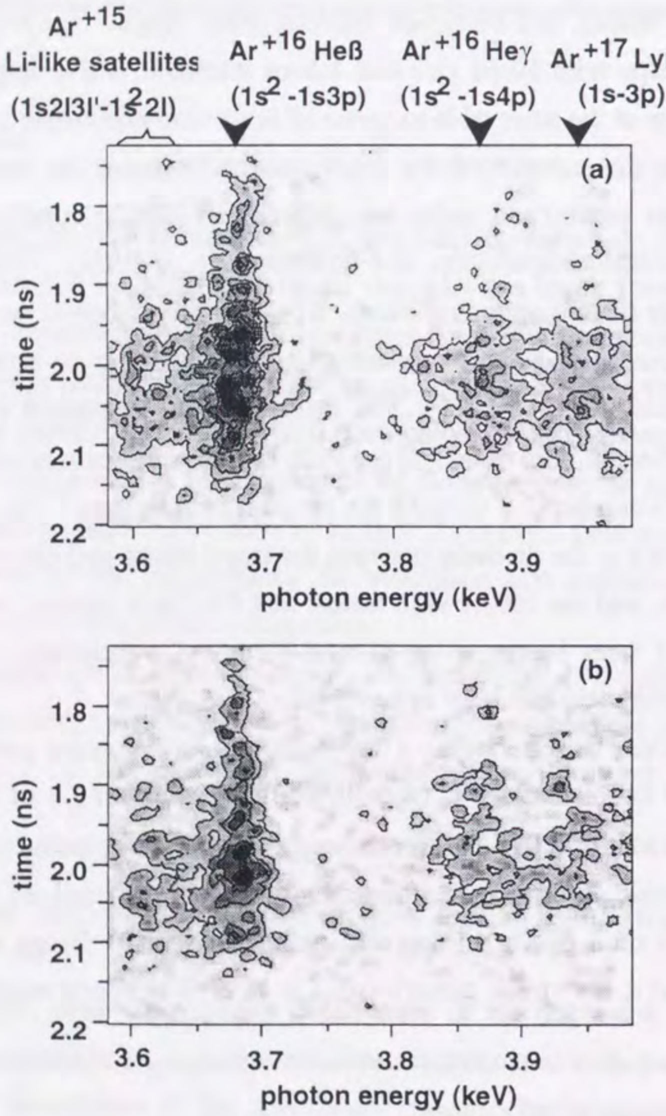

Figure 5-2-1 Streaked images of argon lines. (a) Balanced drive case and (b) imbalanced drive case.

---

[8] B. L. Henke et al., J. Appl. Phys. 52, 1509 (1981).

dependence on electron temperature and density.

Temporal variation of the line intensities and their intensity ratios are shown in Fig. 5-2-2. Also given are calculated trajectories of the pusher-fuel contact surface and the front of shock wave propagating through the compressed fuel. The simulation was made by a non-LTE

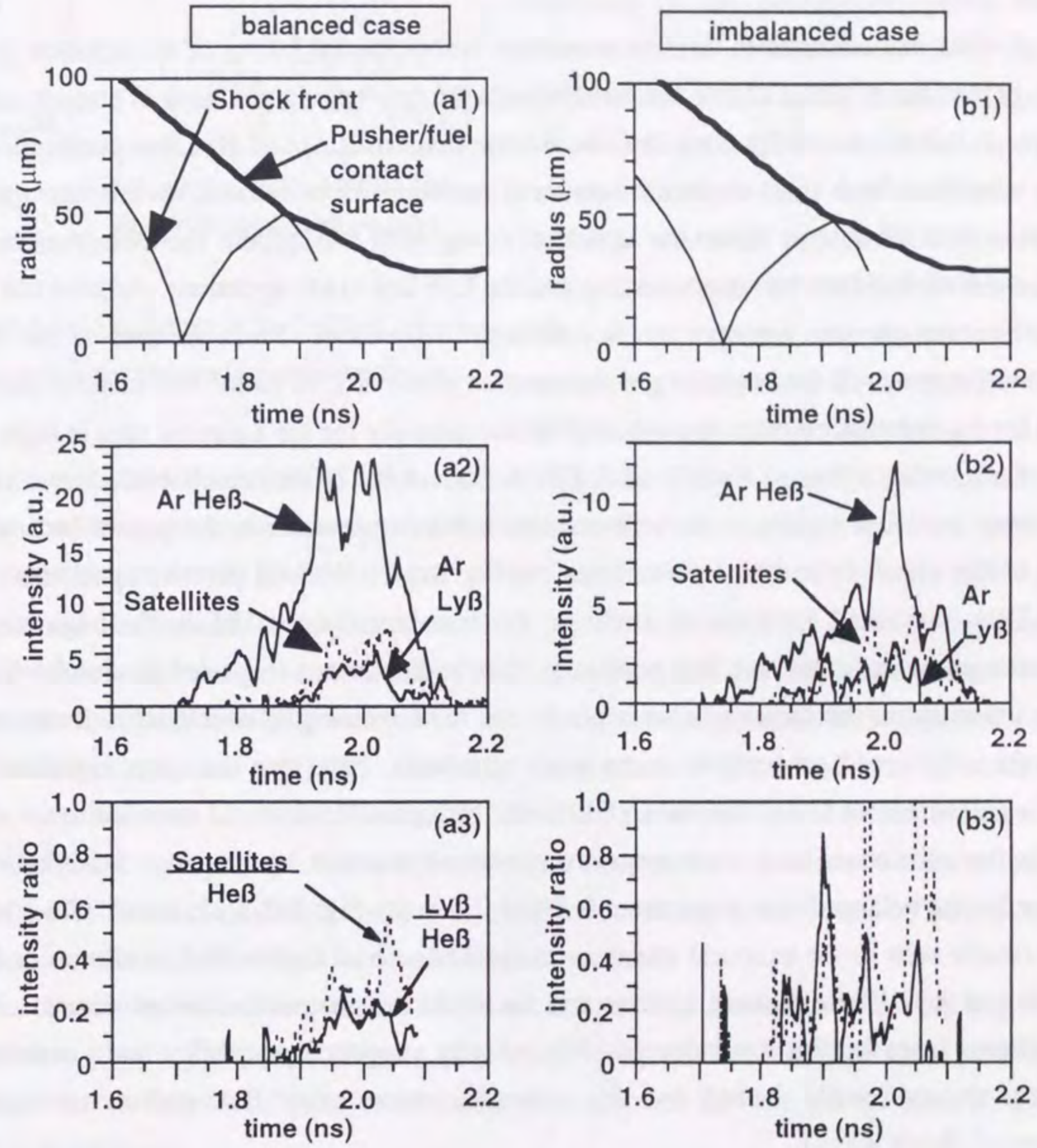

Figure 5-2-2 Temporal evolution of line intensities and line intensity ratios. (a1-a3) Balanced drive case and (b1-b3) imbalanced drive case. (a1, b1) Trajectories of pusher-fuel contact surface and the front of shock wave propagating through fuel region. Both are predicted by non-LTE radiation hydrodynamic 1D code ILESTA. (a2, b2) Temporal evolution of experimental line intensities. (a3, b3) Temporal evolution of line experimental intensity ratios.

(local thermodynamic equilibrium), 1D radiation hydrodynamic code ILESTA-1D[9] in which perfect spherical compression is assumed. Among the observed lines the Heß line has the most intense signal in both balanced and imbalanced cases. This means that the core plasma is kept in a temperature circumstance in which ionic population is dominated by He-like argon. This is confirmed by the ILESTA-1D simulation and consequent postprocessing by the atomic code RATION.[10]

Let us pay attention to the line intensities before the beginning of deceleration phase, namely, before the reflected shock wave encounters the converging pusher-fuel contact surface (see Figs. 5-2-2(a2) and (b2)). One can see that the first small rise of Heß line corresponds to the time when the shock front reaches the center of the target for both cases. At this time the fuel temperature was too low to detect the Lyß line. Along with subsequent fuel compression and heating, the Heß line becomes more intense and the Lyß line starts appearing. Around this time some differences are seen between the two different drive cases. From the time of the shock collision at the center till the beginning of deceleration phase at 1.90 ns for the balanced case and 1.92 ns for the imbalanced case, growth of Heß line intensity for the balanced case is lager than that for the imbalanced case. Results of ILESTA-1D and RATION calculations show that the line intensity increases rapidly as the reflected shock front approaches to the pusher because the volume of the shock heated region becomes rapidly larger. We will discuss again this point below. Thus the small increase of Heß for the imbalanced case before the beginning of deceleration phase indicates that fuel portion at outer radius is not so heated as simulated. The Lyß line intensity for the balanced case is weak until the beginning of deceleration phase, while that for the imbalanced case shows some spiky structures. Note that the spiky signal is well above the measurement noise. (for the Lyß line, the background noise and statistical error of the signal for the imbalanced case were respectively about 0.6 and 0.3 in the Fig. 5-2-2(b2) scale and those for the balanced case were about 0.3 and 0.5 in the Fig. 5-2-2(a2) scale). This feature is more clearly seen in the temporal variation of the line ratio of Lyß to Heß as shown in Figs. 5-2-2(a3) and (b3). These features indicate that the implosion process for the imbalanced case is quite different from that for the balanced case and may suggest a possibility that a number of small regions are locally heated by, for example, some spiky fluid-pistons or multiple reflections of shock waves.

Next, let us inspect the experimental result for the balanced case during the deceleration phase. The Heß line intensity reaches the maximum intensity and keeps its value for about 100 ps. From the broadening of the Heß line, the electron density at this time is estimated to be 3 $\times$ 10^{23} cm^{-3}. The intensity of Lyß and satellite (1s2l3l'-1s^{2}2l) lines also increases after the beginning of deceleration phase. As shown in Fig.5-2-2(a3), the intensity ratios of Lyß/Heß and satellites/Heß start increasing after the beginning of the deceleration phase and then become almost constant till 2.02 ns. The satellites/Heß ratio rapidly increases again after 2.02 ns. Contrastly the Lyß/Heß ratio is still constant till 2.04 ns and decreases rapidly thereafter. Since the satellite/Heß ratio increases during the constant Lyß/Heß ratio between 2.02 and 2.04 ns, plasma temperature and density may change drastically even though the time difference is only 20 ps. According to a contour map of ratio Lyß/Heß vs electron temperature and density derived from RATION (see Fig. 5-2-3), the constant ratio Lyß/Heß of ~ 0.2 indicates the electron temperature of ~ 1 keV for the measured electron density of 3 × 10^{23} cm^{-3}. Therefore the temporally constant line ratio Lyß/Heß and increase of satellite/Heß may suggest that a point characterized by a set of temperature and density is moving along the contour of 0.2. Hence, there are two possible cases of the movement: the electron density increases while the electron temperature decreases and vice-visa. The detailed atomic code analysis [17] shows that an increase of electron density at around 1 keV results in an increase of satellite/Heß ratio. Therefore the experimental results indicate that, in the compressed core plasma, electron temperature decreases while electron density increases. This is provably due to hydrodynamical instabilities occurring at the boundary between pusher (as a source of cold dense electrons) and fuel (hot material).

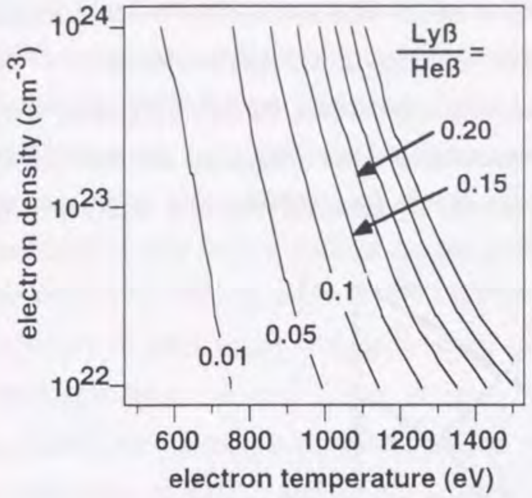

Figure 5-2-3 Dependence of the Lyß/Heß ratio on electron temperature and density calculated by RATION

In the imbalanced case, the Heß line immediately decreases after the beginning of deceleration phase. Temporal behavior of the Lyß/Heß and satellites/Heß ratios shows larger fluctuations than those for the balanced case, suggesting that the core plasma is no longer under stable convergence.

5-2-2 Comparison with a hydro-mix model for the uniform irradiation case

---

[9] H. Takabe et al., Phys. Fluids 3 1, 2884 (1988).

[10] R. W. Lee et al., J. Quant. Spectrosc. Radiat. Transfer 3 2, 91 (1984).

The experimental results were compared with a hydro-mix model. The model predicts time evolution of pusher-fuel mixing region due to growth of perturbations by the hydrodynamic instabilities. First, hydrodynamic parameters necessary for the prediction were obtained with ILESTA-1D. The initial perturbations considered were irradiation non-uniformity of PCL beams and target surface roughness. Initial imprint by time varying non-uniformity of

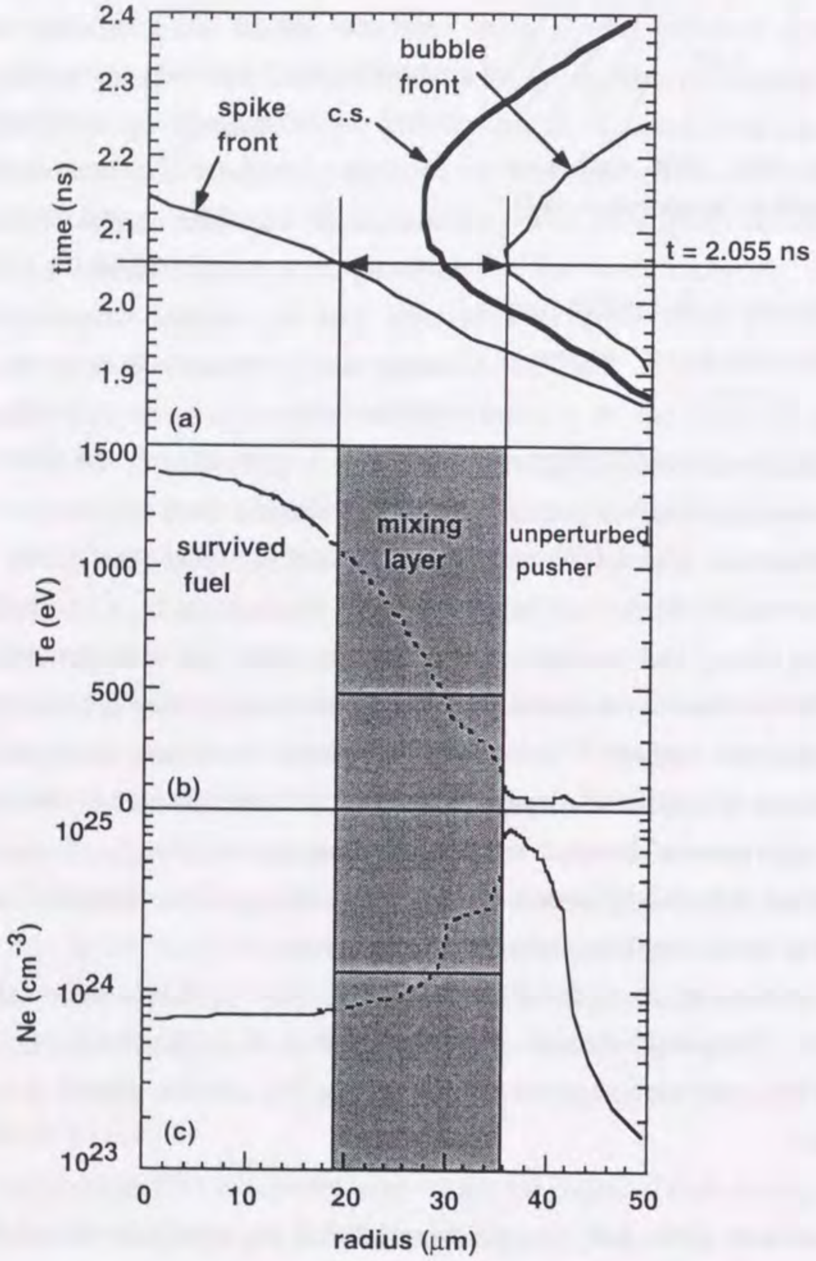

Figure 5-2-4 (a) Temporal evolution of the pusher-fuel contact surface (c.s.), penetration front of the bubble, and that of the spike. (b) temperature and (c) density distributions at around the maximum compression.

the PCL beams and the rippled shock propagation[11] were properly included. After the first shock-breakout through the pusher, perturbation growth at the ablation front due to RT instability, perturbation feed-through to the inner surface, Richtmyer-Meshkov (RM) and RT instabilities at the inner surface, and nonlinear saturation of the perturbation with Haan's model[12] were subsequently calculated. The calculation finally provides time evolution of the pusher-fuel mix region defined by the spike and bubble amplitudes. Figure 5-2-4(a) indicates the calculated mixing layer in the case of σ_{rms} = 1.9% irradiation non-uniformity. Predicted trajectory of the contact surface between pusher and fuel is also shown. To calculate x-ray line emissions from the mix layer, electron temperature and density of the mix layer must be estimated. One example of the calculation results for degradation of experimental neutron yield is presented in Refs.3 and 4. We attempt here to apply the mix model for evaluation of x-ray line emissions.

The electron temperature and density of the mix layer were calculated by assuming that the pusher and fuel completely mix in atomic level so that temperature and density distributions are spatially uniform in the mix layer as illustrated in Figs. 5-2-4(b) and (c). This assumption of the mixing in atomic level may be applicable for the situation that the wavelength of each modal perturbation is comparable or smaller than the depth of the mix region. Thus treatment for extremely lower modal perturbations such as ℓ = 1 and 2 may not be properly included in the present model.

The temperature in the mix layer was estimated with thermal (internal) and kinetic energies of the pusher and fuel in the mix layer. The thermal and kinetic energies of the mix layer are respectively given by

$$E_{thermal\_mix}(t)=\int_{r_{spike}(t)}^{r_{bubble}(t)}\left(\frac{3}{2}T_i(t,r)\cdot n_i(t,r)+\frac{3}{2}T_e(t,r)\cdot n_e(t,r)\right)\cdot 4\pi r^2 dr, \quad \text{Eq. 5-2-1}$$

$$E_{kinetic\_mix}(t)=\int_{r_{spike}(t)}^{r_{bubble}(t)}\frac{1}{2}\rho(t,r)\left[U(t,r)\right]^2\cdot 4\pi r^2 dr, \qquad \text{Eq. 5-2-2}$$

where T is the temperature, n is the number density, subscripts "i" and "e" represent respectively ions and electrons, $r_{bubble}(t)$ and $r_{spike}(t)$ are the radii of the calculated bubble front and the spike front at time "t" respectively, ρ is the mass density, and U is the fluid velocity.

Let us consider two cases to estimate electron temperature of the mix layer on the assumption that these energies are re-distributed evenly over the mix layer. One case is that kinetic energy (i.e., fluid velocity) of the mix layer is not converted to its thermal energy, that is,

---

[11] T. Endo et al., Phys. Rev. Lett. **74**, 3608 (1995).

[12] S. W. Haan, Phys. Rev. A. **39**, 5812 (1989).

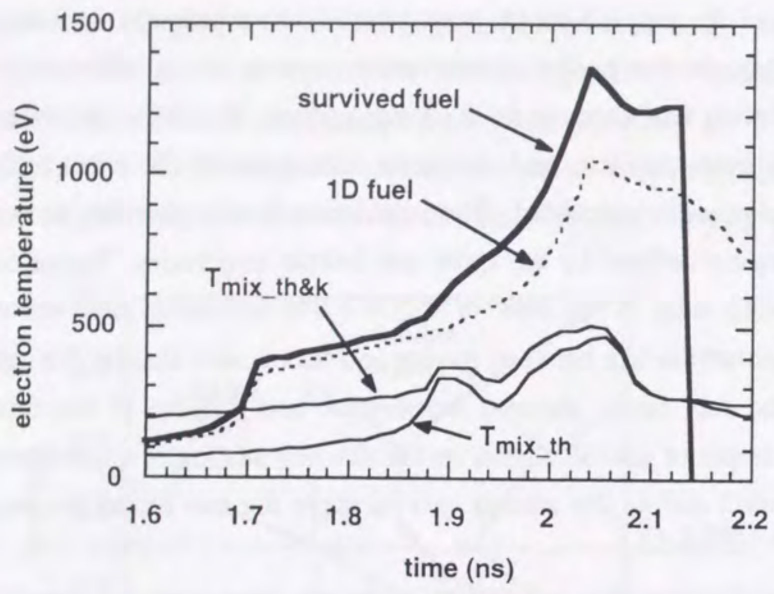

Figure 5-2-5 Temporal variations of electron temperature obtained by the 1D simulation and the mix model.

the $E_{thermal\_mix}$ only contributes to the temperature determination;

$$T_{mix\_th}(t) = \frac{2}{3}\frac{E_{thermal\_mix}(t)}{N_{mix}(t)}, \qquad \text{Eq. 5-2-3}$$

where N_{mix} is the total number of particles (ions and electrons) in the mix layer,

$$N_{mix}(t) = \int_{r_{spike}(t)}^{r_{bubble}(t)} \left[n_i(t,r) + n_e(t,r)\right]\cdot 4\pi r^2 dr. \qquad \text{Eq. 5-2-4}$$

Second case is that kinetic energies of both pusher and fuel in the mix layer are converted completely to thermal energy,

$$T_{mix\_th\&k}(t) = \frac{2}{3}\frac{E_{thermal\_mix}(t) + E_{kinetic\_mix}(t)}{N_{mix}(t)} \qquad \text{Eq. 5-2-5}$$

Figure 5-2-5 shows the temporal evolution of T_{mix_th} , $T_{mix\_th\&k}$, the electron temperature averaged over the survived fuel at the pellet center, and the averaged fuel temperature for pure 1D compression. Calculated temperature of the mix region is higher than that of the pure 1D case because temperature becomes monotonically higher from the outer eroded fuel to the target center as can be seen in Fig. 5-2-4(b). However, it must be noted that thermal conduction from the survived fuel toward the surrounding colder region is not taken into consideration. Therefore, it would be possible that the estimated temperature of the survived fuel is reduced due to the cooling. The temperatures T_{mix_th} and $T_{mix\_th\&k}$ are much

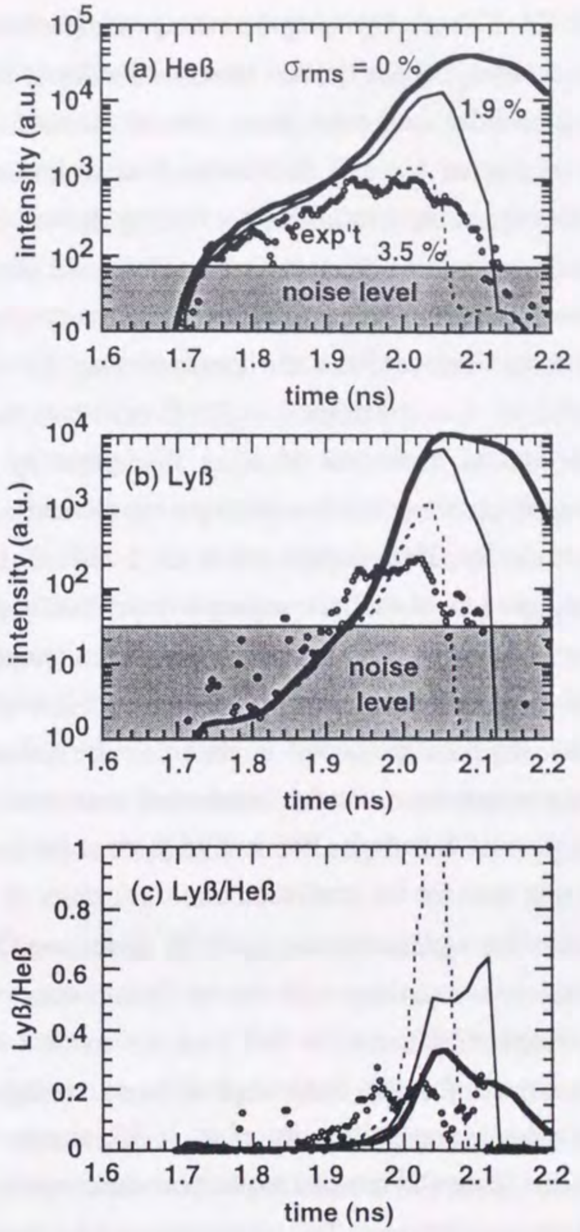

Figure 5-2-6 Comparison of the model calculations with the experiments. The experimental data represented by open circles are the same as shown in Fig. 2 (a). The model calculations are presented for the no-mix (thick solid line), the mix case of σ_{rms}= 1.9% (thin solid line), and that of σ_{rms}= 3.5% (dashed line).

lower than that of the survived fuel and, therefore, Ar line emissions from the cold mix layer are negligible since emissivity of the line is strongly reduced for lower electron temperatures.

Electron density in the mix layer was estimated with electrons provided by both deuterium (fuel) and CH (pusher) in the mix layer. While the deuterium is fully ionized, the CH is partially ionized for the temperatures estimated by the Eqs. 5-2-3 and 5-2-5. Therefore the effective ionization charge of CH involved in the mix layer was derived from the results of non-

LTE calculation with ILESTA-1D code by using the average temperatures T_{mix_th} or $T_{mix\_th\&k}$ and the averaged ion density. Although the estimated electron density is not completely consistent with the n_e in Eq. 5-2-4, we did not make more precise estimations. This is because the temperatures of the mix region are too low to emanate intense line emissions comparable to those from the survived hot region. As a result precise density derivation was unnecessary.

After these determinations, line intensities of Ar Heß and Lyß were calculated by using RATION. The spatial distributions of the temperature and density shown in Fig. 5-2-4 were taken into account for the calculation. Since the measurements have been done in a space-integrated manner and optically thin treatment is valid for the two lines,[13] the intensities are integrated over the whole plasma. Influence of x-ray absorption by the surrounding pusher regions was taken into account by using the simulated pusher thickness. Spectral dependence of the absorption leads to typically 20% higher ratios of Lyß/Heß lines than those for no absorption case. However, growth of the mix region will practically make the pusher thin so that the ratio will be somewhat lower. To avoid such a problem temperature derivation by the use of Li-like-satellite/Heß ratio will be important.[14,15] Figure 5-2-6 shows comparison of the calculated results with the experiments (open circles) for the balanced case. Because the temporal variations of the spectral lines for the imbalanced case was found to be very much bumpy, we did not make the mix calculation for it. The thick solid lines represent the no-mix case and the thin lines the mix case for the irradiation non-uniformity of σ_{rms}= 1.9%. In addition, we made the mix calculation for a plausible non-uniform drive case. Namely absorption non-uniformity will be enhanced in comparison with the irradiation non-uniformity due to oblique incidence of laser light on spherical target. In this case the mode ℓ = 6 non-uniformity is a dominant non-uniformity source for the dodecahedral beam configuration.[16] Therefore we imposed an assumed mode ℓ = 6 non-uniformity of σ_6 = 3% simply onto the standard case, giving σ_{rms}= 3.5% despite that there still remains a question about applicability of the hydro-mix model for such low mode non-uniformity. This is represented by broken lines in Fig. 5-2-6. The vertical axes of Figs.5-2-6(a) and (b) are given in arbitrary units but with same scale so that we can compare these two graphs directly. Experimental data are so plotted along the horizontal and vertical axes that the experimental and calculated Heß line intensities match each other at

---

[13] H. Nishimura et al., Phys. Plasmas **2**, 2063 (1995).

[14] R. C. Mancini et al., *Rev. Sci. Instrum.* **63**, 5119 (1992).

[15] N. Woolsey et al., "Spectroscopic line shape measurements at high densities", 7th International workshop on Radiative Properties of Hot Dense Matter, Santa Barbara, 4-8 Nov. 1996, and to appear in J. Quant. Spectrosc. Radiat. Transfer.

[16] K. Nishihara et al., Phys. Plasmas **1**, 1653 (1994).

their first steep rises. This is because relative intensity measurements were made at the absence of time origin with respect to the drive laser onset. It is seen that, before the beginning of the deceleration phase (1.90 ns), the model predictions for the no-mix and the mix cases agree reasonably with the experiments for the Heß line. From 1.90 to 2.05 ns, the prediction for the σ_{rms} = 3.5% case show better agreement with the experimental Heß line intensity. In contrast, Lyß intensity of the experiment from 1.90 ns to 1.98 ns is larger than that of the three model calculations, and after 1.98 ns they do not agree with the experiments anymore. These disagreements led to a discrepancy in the line ratio as seen in Fig. 5-2-6(c). Since the electron temperature of the calculated core is hotter at the pellet center than that at its outer region, the intensity ratio tends to be higher for a larger amplitude of the mix layer. However, this possibility will be denied because the experimental Lyß intensity from 1.90 to 1.98 ns is larger than those of the calculations. To confirm the experimental results, temperature derivation from the Li-like satellite lines will be necessary. Time- and space-resolved spectroscopic measurements will also provide further information on the perturbation growth and temperature distribution of the mix region (see next section). More sophisticated mixing analysis with multi-dimensional code simulations[17] are underway by taking account of not only low-mode non-uniformities caused by drive power imbalance and drive beam overlapping on the target but also higher-mode non-uniformities caused by the PCL light and laser-light shinethrough[18,19] as an initial stage problem.

In summary, Dependence of implosion stability on low modal irradiation non-uniformity has been investigated by x-ray spectroscopic measurements. K-shell emissions from doped argon and intensity ratios of the Lyß/Heß and satellite/Heß lines have shown the sensitive dependence on the drive uniformity. The hydro-mix model can replicate the temporal variations of the line emissions to some extent. However, the line ratio and the temporally fluctuated structures observed in the imbalanced irradiation experiment could not be convincingly interpreted by the present mix model based on the 1D code. Further study with multi-dimensional simulation codes will be necessary. Besides, analysis on Li-like satellite lines will be important to confirm the electron temperature and density derived from the spectroscopic data.

---

[17] A. Sunahara and H. Takabe, "Two Dimensional Simulation of Implosion in Stagnation Phase", Annual Progress Report of 1996, Inst. of Laser Eng. Osaka Univ., (1997).

[18] D. K. Bradley et al., *Laser Interaction and Related Plasma Phenomena*, (Plenum Press, New York, 1991), **9**, 323.

[19] H. Nishimura et al., *proceedings of 1996 Int. Conf. on Plasma Physics*, to appear in a special issue of Plasma Physics and Controlled Fusion (1997).

5-3 Stability investigation for the uniform irradiation case

Line emissions from Ar doped fusion capsules were observed to investigate implosion stability. A fusion capsule was directly irradiated with twelve beams of partially coherent green light. Imploded core plasmas were diagnosed by observing spatial distribution and time history of the Ar line emissions under high entropy implosion. The experimental result was compared with both one and two dimensional fluid simulations post-processed with an x-ray spectrum analysis code. Drive uniformity and associated perturbation growth at the pusher-fuel boundary are discussed as a plausible reason for the observation.

5-3-1 Experiments

A fusion capsule was directly irradiated with twelve beams of partially coherent light (PCL) extracted from GEKKO XII glass laser facility. The laser wavelength was 526 nm with a bandwidth of 0.6 nm. The drive laser was composed of a 1.6 ns square pulse with a 0.2 ns picket pulse. The rise time was 0.05 ns and time interval of these pulses was 0.4 ns. Such a wave form was chosen to suppress the Rayleigh-Taylor instability at the acceptable expense of implosion efficiency. The rms. value of the irradiation non-uniformity is σ_{rms}= 1.8% assuming that perfect power balance among the twelve beams is obtained.

The fusion capsule was a polystyrene shell of 500μm in diameter and 7.2 ±1 μm in thickness. The capsule was filled with a mixture gas of H_2: D_2: T_2 (5.98: 4.00: 0.02 in atmosphere). In addition, argon gas of 0.024 atm was mixed as a tracer. The capsule was overcoated with 300 Å aluminum to seal the mixture gas at room temperature.

The imploding and imploded plasmas were diagnosed by means of x-ray spectroscopy. Two dimensional images of the imploding plasmas were obtained with an x-ray framing camera (XFC) in order to estimate uniformity of the converging pellet which influences formation of hot spark. The argon line x rays emitted from the imploded core plasmas were recorded by an x-ray monochromatic camera (XMC) and an x-ray streak spectrograph (XSS) in order to know heating and cooling dynamics of the hot spark.

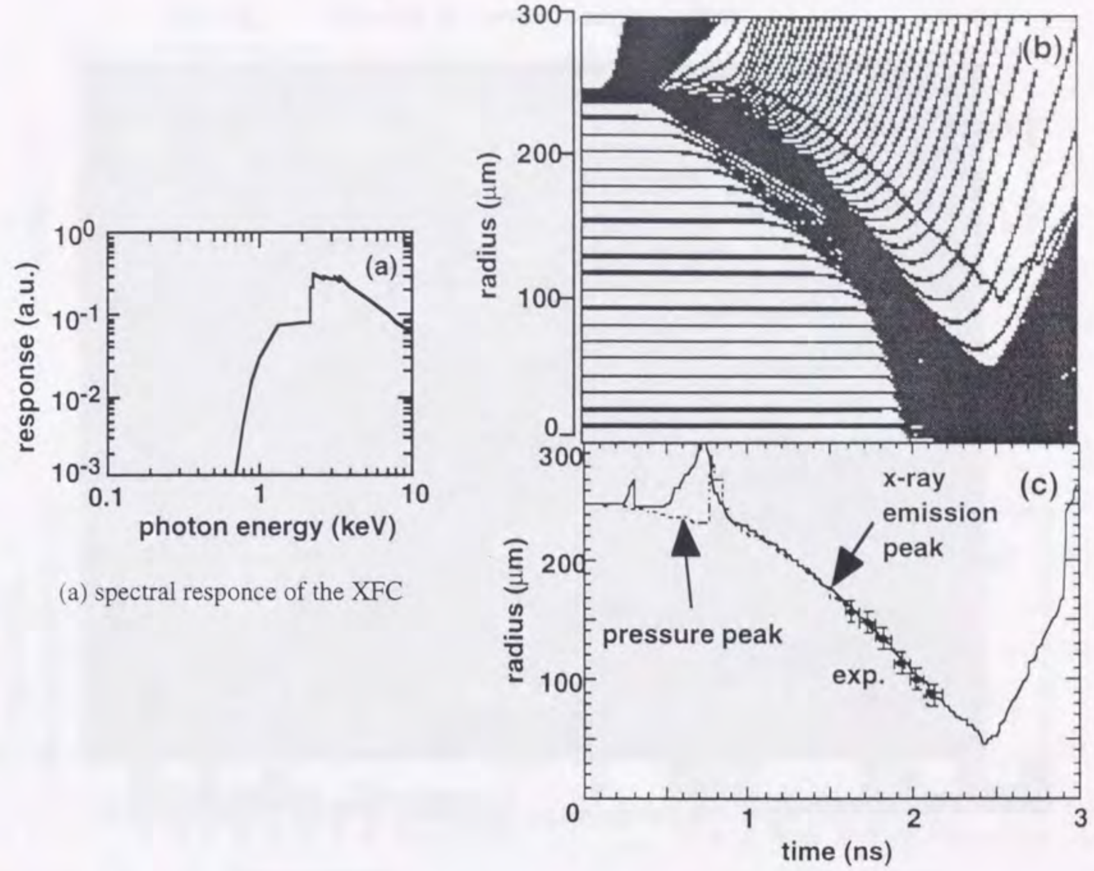

(a) spectral responce of the XFC

Figure 5-3-1 Spectral response of the x-ray framing camera (XFC) (a), a flow diagram simulated by ILESTA-1D (b), and trajectories of pressure and x-ray emission peak positions (c). The peak positions of x-ray emission correspond to those of pressure close to ablation surface.

During acceleration phase, it is worthwhile to pay attention to spatial distribution of the ablation surface where the Rayleigh-Taylor (R-T) instability amplifies perturbation, resulting in influence on stability of pusher/fuel contact surface where the R-T occurs during deceleration phase. To obtain the positions of the ablation surface, the XFC coupled with a pinhole camera providing six images was used. The temporal and spatial resolution was 80 ps and 18 μm respectively.[20] Figure 5-3-1(a) shows spectral response of the XFC which is determined from that of gold used as a cathode[21] and that of 20-μm thick beryllium as a filter. It is seen that the spectral window is from 2 to 4 keV. Figures 5-3-1(b) and (c) show a flow diagram and trajectories of positions of maximum pressure and x-ray emission peak near ablation surface respectively, which were simulated with ILESTA-1D for the experimental condition. Although a

---

[20] H. Honda, Thesis, Osaka Univ. (1998).

[21] B. L. Henke et al., J. Appl. Phys. 52, 1509 (1981).

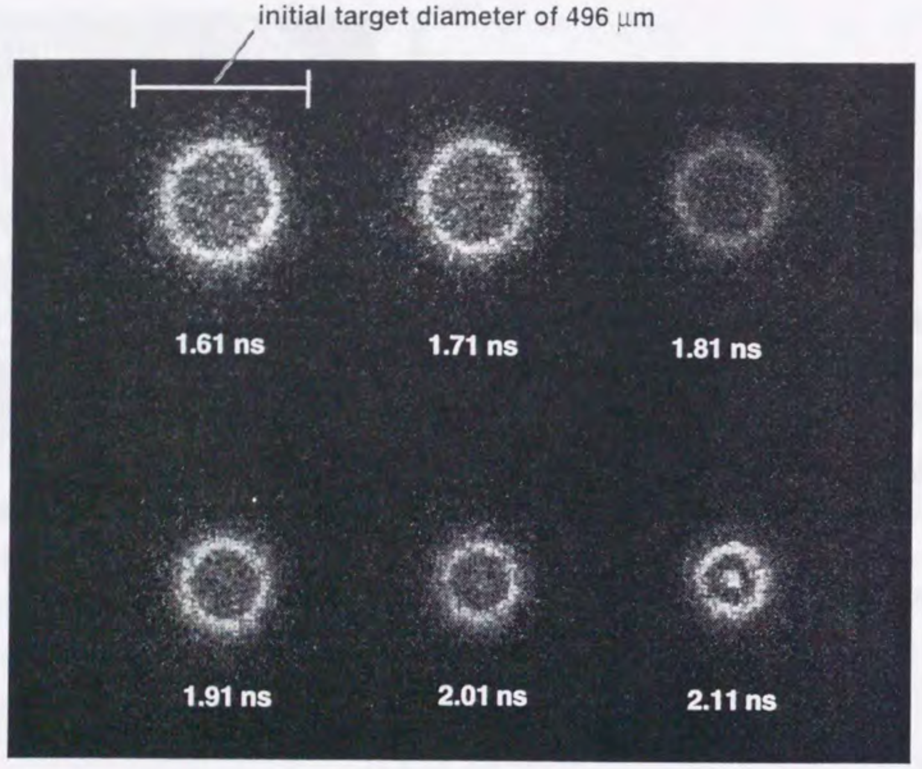

Figure 5-3-2 Imploding plasma images obtained by the x-ray framing camera

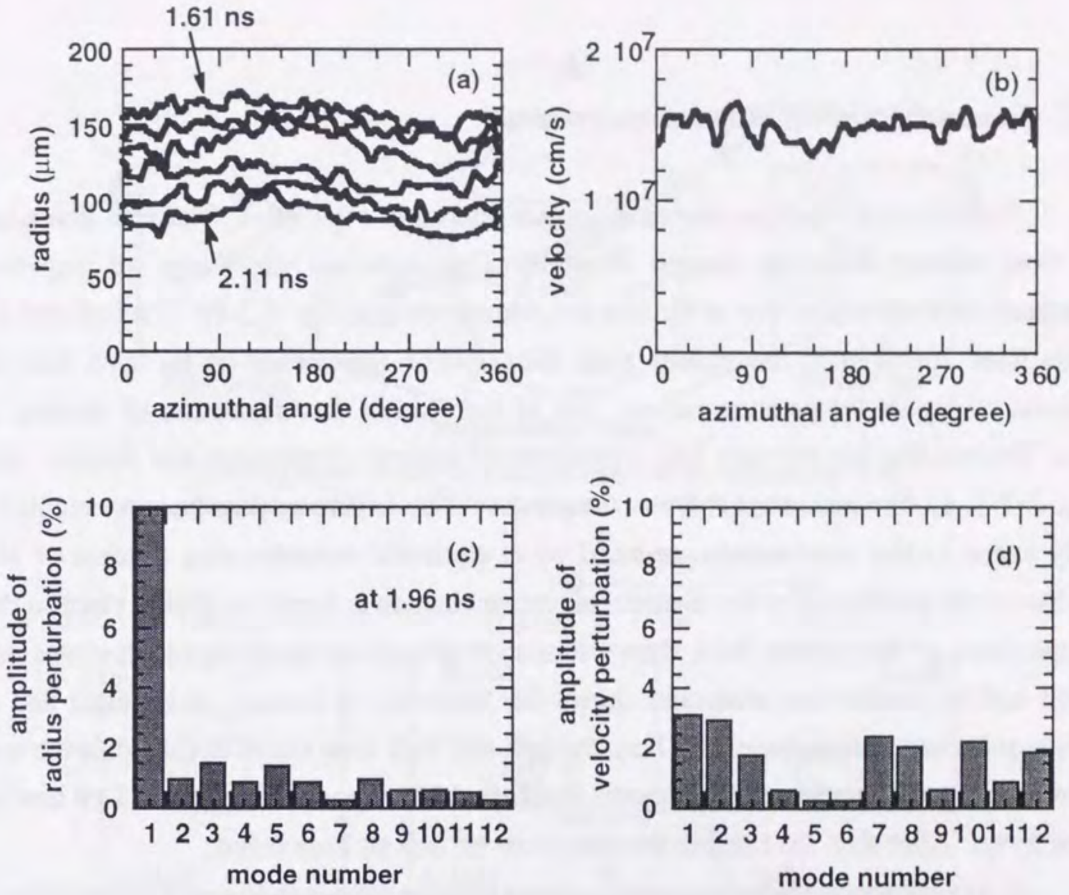

Figure 5-3-3 Position and velocity perturbations of x-ray emission peaks of XFC images (Fig. 5-3-2). (a) Radial positions of the x-ray emission peaks, (b) velocity of the position determined from the positions (a), (c) Fourier amplitude of radial position at 1.96 ns derived from (a) and (b), and (d) Fourier amplitude of velocity of the positions (b).

trajectory of the ablation surface is not drawn, it is confirmed that the maximum pressure point is close to the ablation surface by a few microns. As shown in Fig. 5-3-1(c), the maximum pressure positions fit the x-ray emission peak ones which were obtained with the spectral response of the XFC after ray-tracing along one direction of the sight, taking radiation transfer[22] into account. It is clear that measurements of x-ray emission peak position with the XFC can give information on two-dimensional distribution of the ablation surface which is useful to estimate non-uniformity of the imploding plasmas.

Figure 5-3-2 shows imploding plasma images obtained by the XFC. The converging plasmas can be seen. To estimate the non-uniformity of the compression, distribution of radial peak intensity position was obtained as a function of lateral (azimuthal) angle for the individual images (Fig. 5-3-3(a)). Figure 5-3-3(b) shows velocity of the x-ray peak position as a function of azimuthal angle which was determined from linear fitting of the data in Fig. 5-3-3(a). A spectra shown in Fig. 5-3-3(c) is reduced from Fourier transform of the distribution at 1.96 ns derived from Figs. 5-3-3(a) and (b). The time of 1.96 ns corresponds to the beginning of the deceleration phase. Figure 5-3-3(d) shows Fourier amplitude of the velocity perturbation shown in Fig. 5-3-3(b). The velocity perturbations and position perturbations at 1.96 ns are used as initial conditions for a 2D simulation which starts from the 1.96 ns.

An x-ray streak spectrograph (XSS) with a Rubidium acid phthalate (100) crystal was used to obtain energy and temporal resolutions (they were respectively 120 and 60 ps). The 2D spatial but time-integrated x-ray monochromatic images were also obtained with an x-ray monochromatic camera (XMC). The spatial resolution was 10 μm on the capsule and the integrated spectral width for the Ar Lyβ and Heβ were respectively 13.2 eV and 8.8 eV. These were narrower than broadened width of the spectra for the present experimental condition. Both instruments were calibrated against a crystal spectrograph consisting of a PET (002) crystal and absolutely calibrated x-ray film[23].

---

[22] See Eq. 2-2-4 in Ch.2.

[23] K. Kondo, et al., J. Appl. Phys., **67**, 2693 (1990).

5-3-2 Comparison with simulation results

Time history of argon line emission are shown in Fig. 5-3-4. The Heβ line emission was most intense with the longest duration. This indicates that range of experimental temperature corresponds to that of He-like ion dominance (see Fig. 2-2-1). The Lyβ and Li-like satellite lines appeared at the almost same time. While appearance of the Lyβ line shows formation of higher temperature region, that of the satellite line formation of cooling dense region. The satellite line intensity has dependence of electron temperature and density. As seen in Fig. 2-2-1, Li-like ions exist at lower temperature. The Li-like satellite lines are emitted from doubly exited Li-like ions mainly produced by di-electronic recombination process of He-like ions. Since rate coefficient of the di-electronic recombination is larger for higher electron density, the appearance of the satellite lines shows formation of cooling dense region. Increase of both the Lyβ and the satellite line intensities shows that formation of heating, and cooling and dense region is enhanced simultaneously. Then, the Lyβ and Heβ lines began to fall while the satellite line intensities were increasing. This means that heated hot region which emitted Lyβ line begins to cool down. After that, the satellite lines began to fall and all lines faded.

X-ray monochromatic images of Lyβ and Heβ are shown in Fig. 5-3-4. Intensity

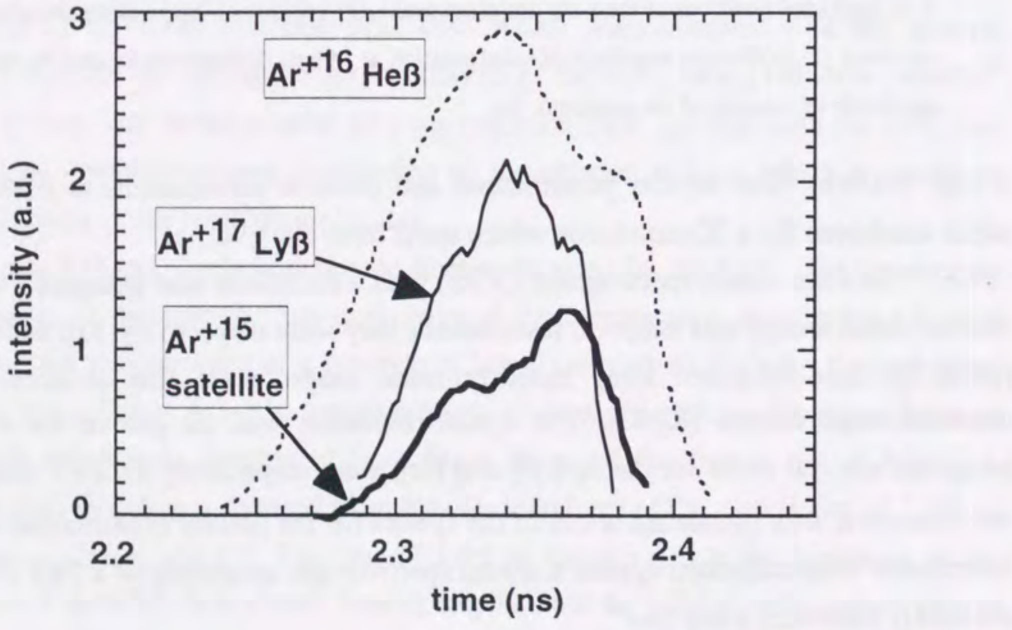

Figure 5-3-4 Time history of argon lines emission.

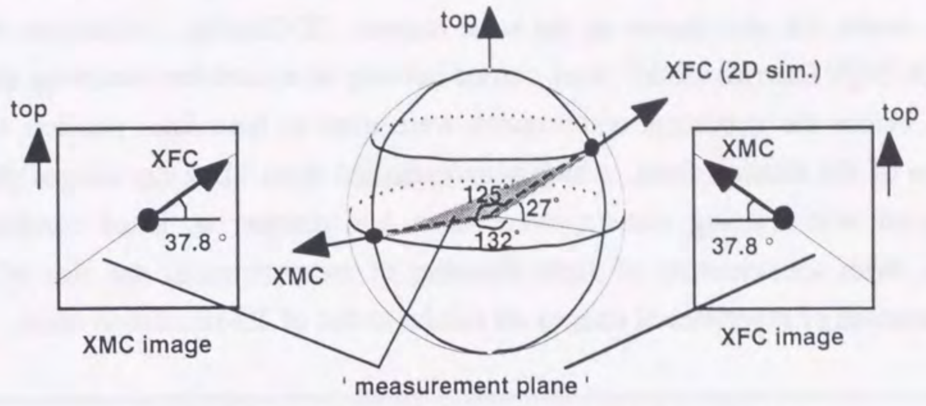

(a) configuration of XMC providing Ar images of the hot spark and XFC providing experimental implosion non-uniformity for 2-D simulation.

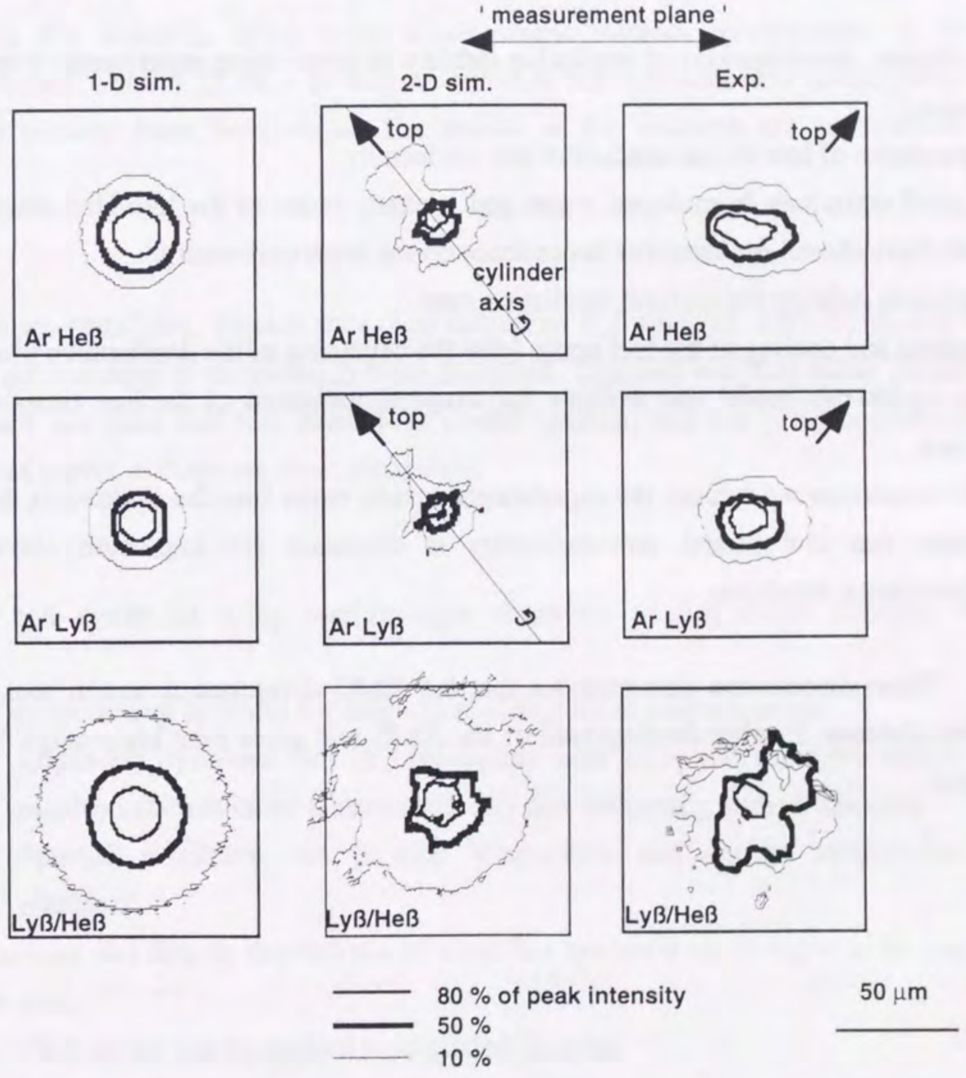

(b) monochromatic images and intensity ratio distribution of experimental and simulation results (1-D and 2-D).

Figure 5-3-5 Comparison of x-ray monochromatic images.

contours of 10%, 50%, and 80% of the peak intensity are drawn. One and two dimensional simulation results are also shown as the same manner. 2D Eulerian simulations with second order GODUNOV Eulerian Code[17] were carried out only at around the maximum compression. 1D results before the maximum compression were used as base line, position and velocity perturbation of the ablation front, which were estimated from 2D x-ray images of imploding shell obtained with framing camera, were taken into account as initial conditions of 2D simulation. With consideration of sight direction of measurements, the size of 50% peak intensity contours of experimental images are similar to that of 2D-simulation ones.

5-4 Summary

In this chapter, investigations of implosion stability in direct-drive experiments were described. In summary,

(1) Dependence of low modal irradiation non-uniformity.

- K-shell emissions from doped argon and intensity ratios of the Lyß/Heß and satellite/Heß lines have shown the sensitive dependence on the drive uniformity.

(2) Implosion stability for uniform irradiation case.

- Heating and cooling of the fuel occur from the beginning of the deceleration phase.
- The hydro-mix model can replicate the temporal variations of the line emissions to some extent.
- 2-D simulation reproduces the experimental results better than the hydro-mix model, which means that low modal non-uniformity is dominant for implosion stability in this experimental condition.

These discussions demonstrates that the XMC developed is useful tool to diagnose imploded plasmas. Further development of the XMC will gives new knowledge on implosion dynamics.

Chapter 6

Conclusion

In this research, using x-ray spectroscopic method, development of X-ray Monochromatic Camera (XMC) to diagnose pusher/fuel behavior and investigation of implosion stability have been made. The results in this research are summarized as follows.

Ch.1

The objective, principles, present state, and subject of ICF research were mentioned and objective and meaning of the research were described. Clarified was that stable formation of hot spark and main fuel was needed for central ignition, and that x-ray spectroscopic method was useful to diagnose them separately.

Ch.2

Principle and merits of x-ray spectroscopic diagnosis of hot dense plasmas were described.

(1) X-ray measurement is useful for evaluation of implosion performances.

- Implosion dynamics can be investigated with x-ray measurement which can resolve information of plasmas spatially and temporally at the same time.
- Spectral resolution can provide temperature and density information of plasmas.

(2) Temperature and density dependence of x-ray line spectra is so strong as to be used as diagnostic tool.

- CRE model can be applied to imploded plasmas.
- Line intensity ratio has strong dependence of electron temperature which can be used for temperature determination.
- Line width due to Stark broadening has electron density dependence which can

be used for density derivation.

- These determination should be done carefully in case of plasma having spatial gradients of temperature and density.

(3) Measurement of x-ray line spectra is useful to know implosion dynamics.

- Spatial distribution of line intensity is rapidly changing, which reflects hot spark heating.
- Spectral, spatial, and temporal resolving measurement is essential to know hot spark heating and cooling mechanisms.

Clarified was that measurements with spectral, spatial, and temporal resolution lead to good understanding of implosion dynamics.

Ch.3

Spectral, spatial, and temporal resolving measurement method was described. X-ray Monochromatic Camera (XMC) and X-ray Streak Spectrometer (XSS) are developed for diagnosis of imploded plasmas.

(1) X -ray monochromatic imaging method can give three kinds of resolution of spectral, spatial, and temporal ones simultaneously.

- Spectral resolution is sufficiently obtained by the use of perfect crystal.
- Spatial resolution is sufficiently obtained by toroidally bent crystal.
- Temporal resolution is sufficiently obtained by a fast imager such as the framing camera developed.

(2) XMC based on the monochromatic imaging method by the help of crystal bending techniques was developed.

- The Johann type monochrometer was applied to 2-dimensional (D) monochromatic imaging.
- Toroidally bent crystal can provide 2-D image suppressed astigmatism.
- Bright image of the plasma can be obtained due to the large aperture.
- Spectral range and brightness of image are variable.
- 2-ch XMC for Heß and Lyß lines of argon was developed.
- 5-ch XMC for Heß and Lyß of chlorine and continuum added to the argon lines was developed.

(3) XSS can provide spectra of argon and chlorine lines with sufficient temporal resolution.

Clarified was that three types of resolution can be ensured by the help of x-ray monochromatic imaging method.

Ch.4

Demonstration of x-ray monochromatic imaging method with the XMC for the imploded plasmas were described.

- Consistency with other calibrated measurements was confirmed.
- Separated measurements of pusher and fuel became possible.

Clarified was that usefulness of the XMC for direct measurements of pusher/fuel mixing was demonstrated

Ch.5

Investigations of implosion stability in direct-drive experiments were described.

(1) Dependence of low modal irradiation non-uniformity.

- K-shell emissions from doped argon and intensity ratios of the Lyß/Heß and satellite/Heß lines have shown the sensitive dependence on the drive uniformity.

(2) Implosion stability for uniform irradiation case.

- Heating and cooling of the fuel occur from the beginning of the deceleration phase.
- The hydro-mix model can replicate the temporal variations of the line emissions to some extent.
- 2-D simulation reproduces the experimental results better than the hydro-mix model, which means that low modal non-uniformity is dominant for implosion stability in this experimental condition.

In conclusion, these discussions demonstrates that the XMC is useful tool to diagnose imploded plasmas. Further development of the XMC (described in Ch.2) will gives new knowledge on implosion dynamics and can contribute to ignition and high-gain design.

Acknowledgments

I would like to express my gratitude to Professor Tatsuhiko Yamanaka and Professor Yoshiaki Kato for helpful advice.

I would like to thank Professor Kunioki Mima and Professor Sadao Nakai for providing me with opportunity to work at Institute of Laser Engineering (ILE) in Osaka University.

Thanks are due to Professor Takatomo Sasaki, Professor Masahiro Nakatsuka, and Professor Katsunobu Nishihara for reading the manuscript and making a number of helpful suggestions. I would like to thank Professor Kenji Matsu-ura, Professor Sadatoshi Kumagai, and Professor Ki-ichiro Tsuji for helpful suggestions in making the thesis.

I greatly acknowledge helpful suggestions and valuable advice with Associate Professor Hiroaki Nishimura.

I would like to thank Professor Eckhart Förster, Dr. Ingo Uschmann, and Dr. Markus Vollbrecht for valuable suggestions in collaboration on x-ray monochromatic imaging.

Thanks are also due to scientists in ILE for helpful advice. Among them are Associate Professor Hiroshi Azechi, Associate Professor Noriaki Miyanaga, Associate Professor Shuji Miyamoto, Assistant Professor Hiroyuki Shiraga, and Assistant Professor Mitsuo Nakai for thoughtful suggestions and advice mainly on the experimental research. I would like to thank Professor Hideaki Takabe for valuable comments on analysis with fluid simulation.

I am indebted to technical staffs of the GEKKO laser facilities for technical support. Among them are Mr. Osamu Maekawa, Mr. Masaki Saito, Ms. Kyoko Shimada, Mr. Masahiro Miyamoto, Mr. Toru Urano, Mr. Tomohiro Matsushita, Mr. Tatsuya Sonomoto, Mr. Toshiya Shozaki, Mr. Hiroyuki Azuma, Mr. Shinji Urushihara, Mr. Noboru Morio, Mr. Tetsuji Kawasaki, Dr. Masaru Takagi, and Ms. Motoko Kimura.

I wish to thank all my colleagues for helpful discussions. Among them are Dr. Nobuhiko Izumi, Mr. Hiroshi Honda, Mr. Keisuke Shigemori, Mr. Manabu Heya, Mr. Yoshihiro Ochi, Mr. Mikio Nakasuji, Mr. Keiji Hariki, Mr. Katsuaki Kondo, Mr. Daisuke Ohnuki, Mr. Hajime Miki, Mr. Isamu Niki, Mr. Jiro Funakura, Dr. Atsushi Sunahara, Mr. Toru Kawamura, and Mr. Shuji Naruo.

I would like to thank Japan Society for the Promotion of Science for their financial support. I wish to express my thanks to all taxpayers in Japan for their support.

Finally, my special thanks are due to my father Mr. Tadahiro Fujita, my mother Ms. Kimiko Fujita, and my wife Ms. Emi Fujita for their warm support for my own way.

Publication list

Publications

1. "Two dimensionally space-resolved electron temperature measurement of laser created fusion plasmas,"
K.Fujita, H.Nishimura, I.Uschmann, E.Förster, H.Takabe, Y.Kato, S.Nakai, and K.Mima,
Journal of Electron Spectroscopy and Related Phenomena **80**, 291 (1996).

2. "Time- and Space-resolved X-ray Spectroscopic Measurements of Hot Dense Plasma Created with Laser Driven Implosions,"
K.Fujita, Y.Ochi, H.Nishimura, H.Azechi, N.Miyanaga, H.Shiraga, I.Uschmann, M.Vollbrecht, E.Förster, A.Sunahara, H.Takabe, and K.Mima,
Journal of Quantitative Spectroscopy & Radiative Transfer (1997), in press.

3. "Pusher-fuel mixing measurements of laser fusion plasmas with x-ray monochromatic imaging,"
K.Fujita, H.Honda, Y.Ochi, H.Nishimura, I.Uschmann, M.Vollbrecht, E.Förster, A.Sunahara, S.Naruo, H.Takabe, and K.Mima, to be submitted.

4. "Investigation of implosion stability in direct drive implosion experiments with the GEKKO XII,"
K.Fujita, H.Honda, Y.Ochi, I.Niki, H.Nishimura, I.Uschmann, M.Vollbrecht, E.Förster, A.Sunahara, S.Naruo, H.Takabe, and K.Mima, to be submitted.

5. "Damage problem to fusion target caused by foot pulse of drive laser,"
K.Fujita, M.Nishikino, I.Niki, Y.Ochi, H.Nishimura, H.Shiraga, N.Miyanaga, H.Azechi, I.Uschmann, M.Vollbrecht, E.Förster, A.Sunahara, S.Naruo, H.Takabe, and K.Mima, to be written.

6. "Study of indirectly-driven implosion by x-ray spectroscopic measurements,"
H.Nishimura, T.Kiso, H.Shiraga, T.Endo, K.Fujita, A.Sunahara, H.Takabe, Y.Kato, and S.Nakai,
Phys. Plasmas **2**, 2063 (1995).

7. "Temperature mapping of compressed fusion pellets obtained by monochromatic imaging"
I.Uschmann, E.Förster, H.Nishimura, K.Fujita, Y.Kato, and S.Nakai,
Rev. Sci. Instrum. **66**, 734 (1995).

8. "High-convergence uniform implosion of fusion pellets with the new GEKKO laser,"
H.Nishimura, H.Azechi, H.Shiraga, M.Nakai, N.Miyanaga, H.Takabe, T.Norimatsu, H.Fujita, K.Shigemori, M.Heya, S.Izumi, H.Honda, K.Fujita, A.Sunahara, M.Honda, T.Kanabe, T.Jitsuno, M.Takagi, R.Kodama, K.A.Tanaka, M.Nakatsuka, K.Nishihara, Y.Kato, T.Yamanaka, S.Nakai, and K.Mima,
Plasma Physics and Controlled Fusion **39**, A401 (1997).

9. "Five channel x-ray imaging of laser fusion plasmas,"
M.Vollbrecht, I.Uschmann, M.Dirksmöller, E.Förster, K.Fujita, Y.Ochi, H.Nishimura, and K.Mima,
Journal of Quantitative Spectroscopy & Radiative Transfer(1997), in press.

10. 「多チャンネルＸ線単色カメラの開発」
藤田和久、西村博明、M.Vollbrecht, I.Uschmann, E.Förster、高部英明、三間圀興
信学技報、vol. 96, No.105, p1(1996)、電子情報通信学会

International conferences

1. "Imploded core diagnostics by x-ray monochromatic imaging,"
K.Fujita, H.Nishimura, I.Uschmann, E.Förster, H.Takabe, Y.Kato, and S.Nakai,
12th Laser Interaction and Related Plasma Phenomena, Osaka, Japan, April 27,1995.

2. "Two dimensionally space-resolved electron temperature measurement of laser created fusion plasmas,"
K.Fujita, H.Nishimura, I.Uschmann, E.Förster, H.Takabe, Y.Kato, S.Nakai, and K.Mima
11th International Conference on Vacuum Ultraviolet Radiation Physics, Tokyo, Japan, August 31, 1995.

3. "Temperature distribution measurement of inertially confined fusion plasmas by x-ray monochromatic imaging method,"
7th international conference on Plasma Physics and Nuclear Fusion "Fusion Plasma Diagnostics", Toki, Japan, November 30, 1995.

4. "Time- and space-resolved x-ray spectroscopic measurements of hot and dense core plasma created by laser driven fusion,"
K.Fujita, Y.Ochi, H.Miki, H.Nishimura, H.Azechi, N.Miyanaga, H.Shiraga, A.Sunahara, H.Takabe, and K.Mima,
1996 International Conference on Plasma Physics, Nagoya, Japan, September 12, 1996.

5. "Pusher and fuel temperature distribution measurements in laser fusion by the use of Multi-Channel X-ray Monochromatic Camera,"
K.Fujita, H.Honda, Y.Ochi, D.Ohnuki, S.Miyamoto, H.Nishimura, M.Vollbrecht, I.Uschmann, E.Förster, A.Sunahara, H.Takabe, and K.Mima,
The 38th Annual Meeting of Division of Plasma Physics, Denver, CO, USA, November 15, 1996.

Domestic conferences (first author only)

1. Ｘ線爆縮核融合 III　Ｘ線分光によるコアプラズマ診断
日本物理学会　第48回年会　1993年3月30日

2. Ｘ線モノクロ画像計測による爆縮コアプラズマ診断
日本物理学会　第49回年会　1994年3月28日

3. Ｘ線モノクロ画像計測を用いた電子温度マッピングと爆縮コアプラズマ診断
日本物理学会　秋の分科会　1994年9月2日

4. Ｘ線分光を用いたレーザー爆縮プラズマ診断
日本物理学会　第50回年会　1995年3月30日

5. 新激光XIIによる直接照射爆縮実験
Ｘ線分光画像観測によるコアプラズマの電子温度分布
日本物理学会　秋の分科会　1995年9月29日

6. 新激光XII直接照射爆縮におけるホットスパークＸ線分光診断
プラズマ・核融合学会　第13回年会　1996年3月21日

7. 間接照射爆縮の研究　X線分光計測によるホットスパークの診断
日本物理学会　第51回年会　1996年4月3日

8. X線単色画像法を用いた輻射駆動爆縮の観測
日本物理学会　秋の分科会　1996年10月4日

9. X線単色画像法によるホットスパーク構造の観測
日本物理学会　第52回年会　1997年3月30日

10. X線輻射駆動爆縮における爆縮コアプラズマのダイナミクス
日本物理学会　秋の分科会　1997年10月5日

11. X線輻射駆動方式における爆縮安定性の解析
プラズマ・核融合学会　第14回年会　1997年11月28日

Topical conferences

1. 二次元弯曲結晶を用いたX線モノクロカメラとこれを用いた爆縮コアプラズマ診断
文部省核融合科学研究所共同研究研究会　1994年12月9日

2. X線モノクロ画像計測による爆縮コアプラズマ診断
レーザー研シンポジウム　1995年7月15日

3. 新激光XII直接照射爆縮におけるホットスパークX線分光診断
レーザー研シンポジウム　1996年3月18日

4. 多チャンネルX線単色カメラの開発
電子ディスプレイ研究会 -画像変換技術合同研究会-　1996年6月20日

5. X線分光計測によるレーザー爆縮の安定性評価
核融合科学研究所研究企画情報センター素過程データ作業会 1997年1月30日

Appendix

Configuration and alignment procedure of X-ray Monochromatic Camera (XMC)

Described are technical points necessary for determination of XMC configuration, alignment procedure, and tools for the alignment.

Contents

1. Definition of "Alignment triangle"

To design configuration of XMC at a target chamber, it is useful to use an "alignment triangle" formed by an object (O), a bent crystal (C), and an imaging point (D) as shown in Fig. 1. The bent crystal is set for a given Bragg angle by fixing the two points O and D. Namely, the crystal should be set on a circle around the rotational axis formed by O and D. The radius of the circle is CC'.

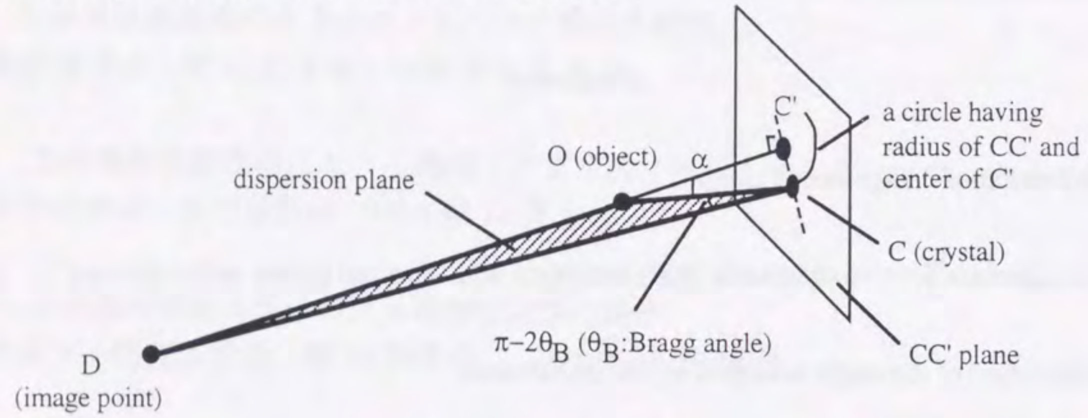

Fig. 1. "Alignment triangle"

Two fundamental equations for imaging are introduced here. One is the lens equation,

$$\frac{1}{OC}+\frac{1}{CD}=\frac{1}{f}\,, \qquad \textbf{Eq. 1}$$

where f is a focal length for the bent crystal, and

$$f=\frac{R_h \sin\theta_B}{2}, \qquad \textbf{Eq. 2}$$

where R_h is the horizontal (dispersion direction) bending radius of the bent crystal.

Suppose we will use the bent crystals kept at ILE so that bending radii and Bragg angles of the crystals are given. This determines the focal length by Eq. 2. Besides, assuming that the distance of OD is 2000 mm, the triangle can be uniquely determined. Table 1 lists up the geometrical parameters for the three channels (Ar Heß, Ar Lyß, and Ti Heß) proposed for example. We will proceed discussions by using these values hereafter.

Table 1 Parameters for 3-ch X-ray Monochromatic Camera

Channel	X-ray line	Wavelength (nm)	Crystal	Bragg angle (degree)	Bending radii * (h/v) (mm)	Focal length (mm)	Image magnificatio	Distance of OC (mm)	Distance of CD	Alpha (degree)
1	Ar Heß	0.3366	Ge (311)	80.622	200/197.32	98.66	20.26	103.5	2097.5	19.76
2	Ar Lyß	0.3151	Si (311)	74.187	200/185.14	96.22	20.67	100.9	2085.1	33.14
3	Ti Heß	0.26097	Si (400)	73.99	200/185.14	96.12	20.68	100.8	2085	33.56

- * "h" and "v" means horizontal and vertical direction. The dispersion direction corresponds to the horizontal one.
- The focal lengths f for the bent crystal are calculated by $f = R_h \sin(\theta_B)/2$, where R_h is the horizontal bending radius and θ_B is the Bragg angle.
- The image magnifications are determined from the distance of CD divided by that of OC. (See Fig. 1.)
- The "O", "C", and "D" show the positions of the object, the crystal, and the detector respectively.
- The angle of the alpha is shown in Fig. 1.

2. Requirement for two diagnostic ports equipped with a crystal holder and a detector

Using a set of geometrical parameters listed in Table 1, the condition limits freedom of choice of two particular diagnostic ports for installation of the crystal holder and the detector. The angle α in Fig. 1 and Table 1 is useful to find proper combination.

3. Estimation of the angle occupied by the instruments

In principle, the occupation angle is determined by two factors. One is a difference of Bragg angles between different channels, and the other is the size of each crystal holder. In case of using more than two channels, estimation is needed for angular spread perpendicular to the dispersion plane. Described below is the case for the parameters in Table 1.

(a) Bragg angles among different crystals

Since the angle α depends on the Bragg angle, the angular difference Δα between the α' s of plural channels determines the occupation angle. In case of Ti Heß and Ar Lyß, we obtain Δα = 33.56°- 19.76°= 13.8°. In principle, this value is the minimum angle occupied in a target chamber.

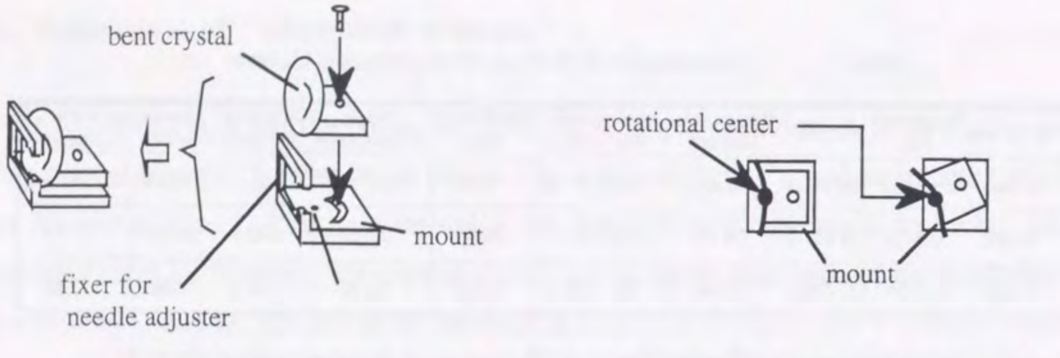

(a) schematic crystal mount

(b) the crystal can be rotated on the mount.

Fig. 2 Crystal mount

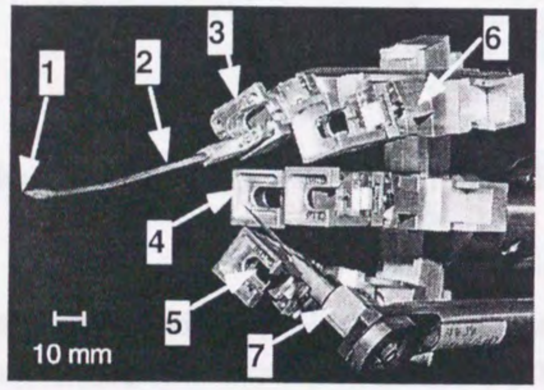

Fig. 3 Five-channel x-ray monochromatic camera

1. target position
2. local needle for crystal alignment
3. needle adjuster
4. crystal mount
5. bent crystal
6. mini-gonio
7. main needle for all the crystal alignment

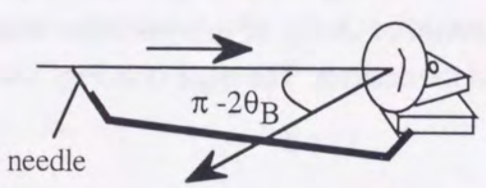

Fig. 4 aligned "crystal-needle unit"

(b) Size of each crystal mount

We use a metallic needle to align the crystal (we call this local needle hereafter) . The needle is mounted closely to the crystal. The local crystal mount has removable adjuster for the needle, and the crystal is mounted on a separate adjuster on which the needle adjuster is mounted (see Figs. 2-5). In the present scheme, the needle adjuster set in front of the bent crystal determines the angle occupied in a chamber, too. Assuming that the width of the needle adjuster is 16 mm and the depth is 8 mm, a half of the occupied angle is 4.9°. (The underline shows the value taken in the ILE case.) Including $\Delta\alpha$, the total occupation angle will be 23.2° (= 13.8°+ 4.9°*2).

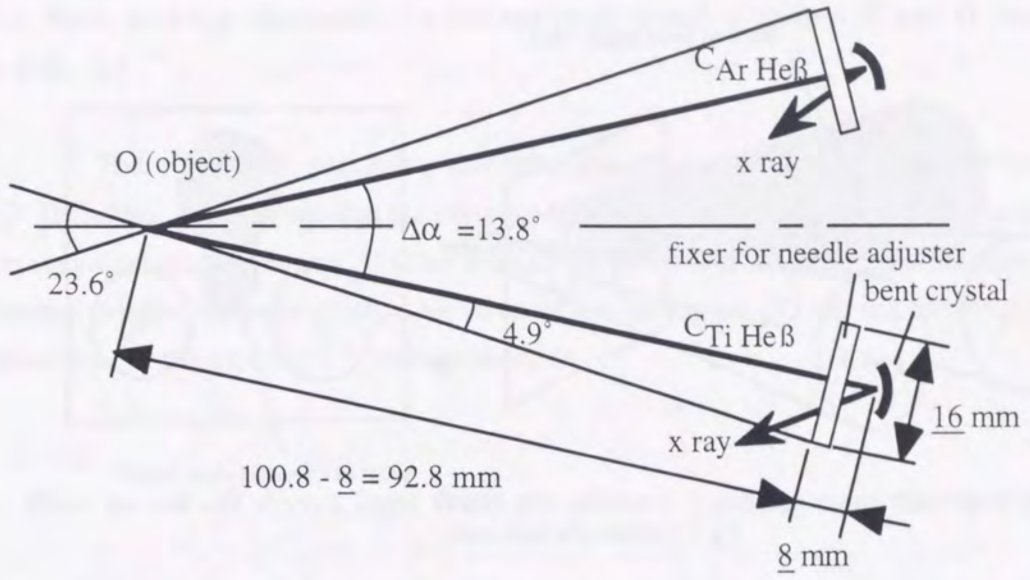

Fig. 5 Schematic geometry for Ar Heß and Ti Heß channels

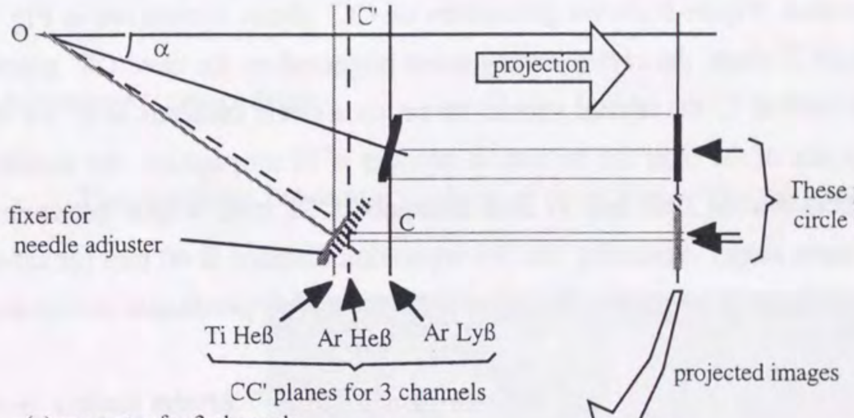

(a) geometry for 3 channels

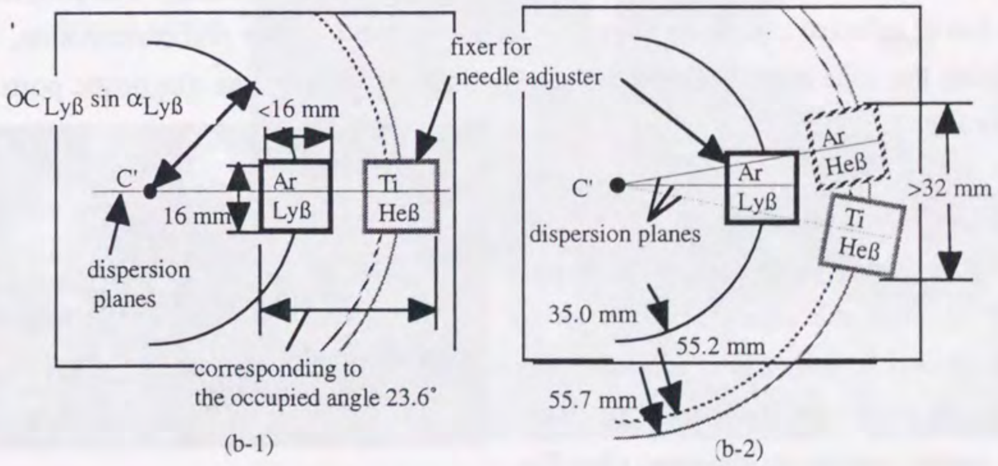

(b-1)

(b-2)

Fig. 6 Geometry at CC' plane for 3 channels

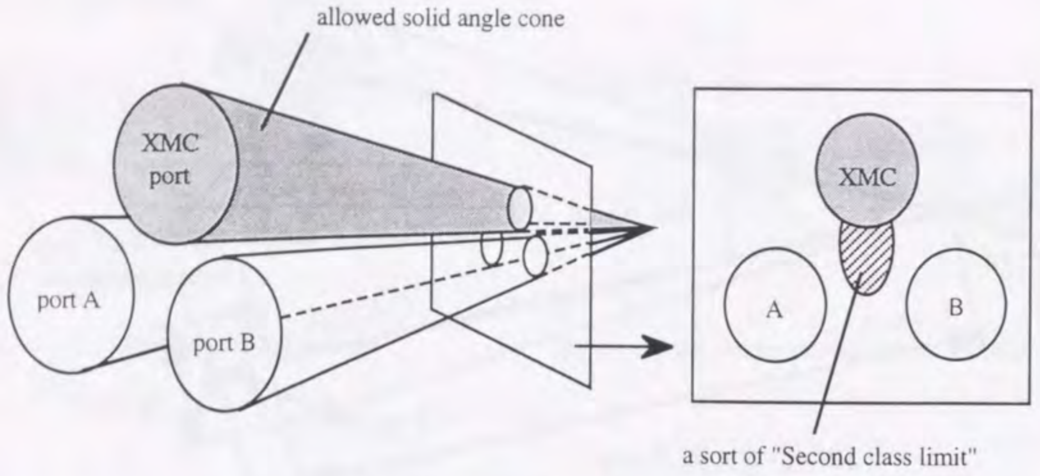

Fig. 7 Adjacent solid angle cones

This occupation angle discussed above is the case on the dispersion plane. When we use more than two channels, another occupation angle perpendicular to the dispersion plane should be estimated. Figure 6 shows geometries on CC' planes introduced in Fig. 1. Figures. 6 (b-1) and (b-2) show the crystal arrangement projected on the three CC' planes. As mentioned in the section 1, the crystal should be set on a circle centered at C' on the CC' plane. Since the size of the fixer for the needle adjuster is 16 mm square, the smallest separation distance between Ar Heß and Ti Heß channels is 32 mm, which determines perpendicular occupation angle. Assuming that the separation distance is 40 mm for safety and the distance from the position O is 100 mm, we obtain the perpendicular occupation angle of 21.8°.

These angles are sufficiently smaller than the angle 37° of the largest port. However, we must look for another diagnostic port for image recording. The port must be on a line of reflected ray. If we should be unable to find a proper port combination, we must violate the solid angle policy if we can find a room between the diagnostic ports as shown in Fig. 7.

(c) Clearance outside the chamber

Removable guide rails of 1 m long are used so that the crystal holder can be installed smoothly into the diagnostic port. Space for the guide rails length and installation work is needed outside the chamber. (See Fig. 8.)

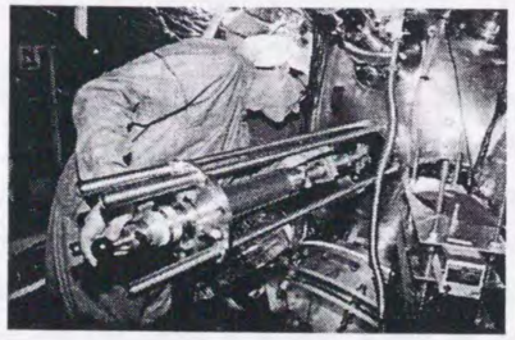

Fig. 8 Dr. Ingo Uschmann installs the crystal holder with guide rails.

4. How to keep clearance for the ray pass crossing points C and D (defined in Fig. 1)

There may be a possibility that other diagnostic instruments block the ray pass CD. It should be also noted that the ray pass CD has an angle from the line of observation for a nominal diagnostic axis. If there is an obstacle, such as a vacuum seal window of an framing camera, the holder might be centered for the ray of OD not for the ray CD. All clearances for the ray pass CD must be ensured.

5. How to cut off direct light from the plasma incident onto the detector

A thick metallic plate must be placed on the line OD to cut off the direct light from the object. (See Fig. 10.)

6. Alignment procedure

The alignment procedure consists of three steps. The first step is that the Bragg

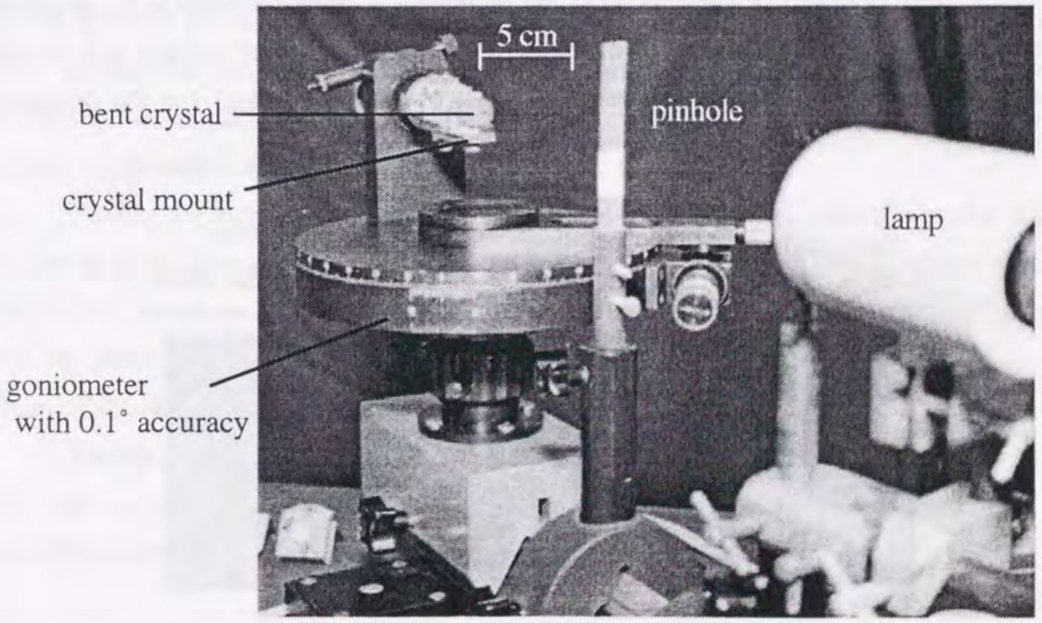

Fig. 9 Goniometer

angle and the distance of OC are fixed for each crystal. The second step is that the alignment triangle for each channel is defined outside the target chamber. At the third step, the aligned set of the crystal holder and the detector is brought to the target chamber, and finally whole alignment is confirmed with a diagnostic laser shot.

I. Bragg angle and the distance OC

A bent crystal can be fixed on a crystal mount. This has a mechanism so as to rotate the crystal around the crystal surface. After the azimuth alignment of the toroidally bent crystal, the crystal is so set that the angle between the incident and reflected light is $\pi-2\theta_B$ by using of a goniometer shown in Fig. 9. This goniometer is one of essential tools for the alignment.

Next step is that a local needle adjuster is put on the crystal mount to fix the angular relationship between the crystal surface and incident ray pass. Besides, the distance of OC can be fixed by the position of the needle top. We call the set of them "crystal-needle unit" hereafter (See Fig. 4). One must repeat this process for each crystal.

II. alignment of all the channels outside the target chamber

In this step, the configuration of the XMC is realized at the outside of the target chamber because the in-situ alignment is hard to be done in a big target chamber. To begin with, the "diagnostic triangle" formed by the target and two diagnostic ports should be reproduced very precisely at the outside of the chamber. A large tolerance in the angle and distance may results in misalignment of image on the detector. (The angular and distance precision necessary will be given lately.) A skeleton has been used for the diagnostic triangle alignment in ILE (Fig. 10). Figure 11 shows a proposed fixer for the joint experiment. This has a merit that some additional tools such as telescopes can be fixed stably to provide the more precise alignment. Two ports of the skeleton have rotatable flanges around the diagnostic axis to reproduce any combination of diagnostics ports. After fixing the diagnostic triangle carefully, the crystal holder and the detector (or its imitation) are installed on the two ports.

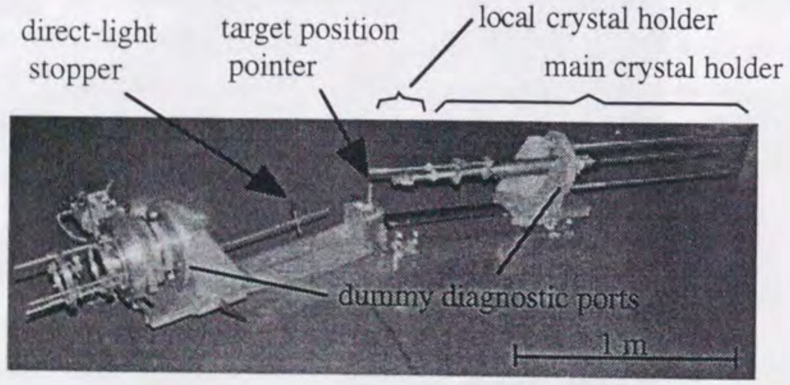

Fig. 10 Skeleton to align outside the target chamber in ILE

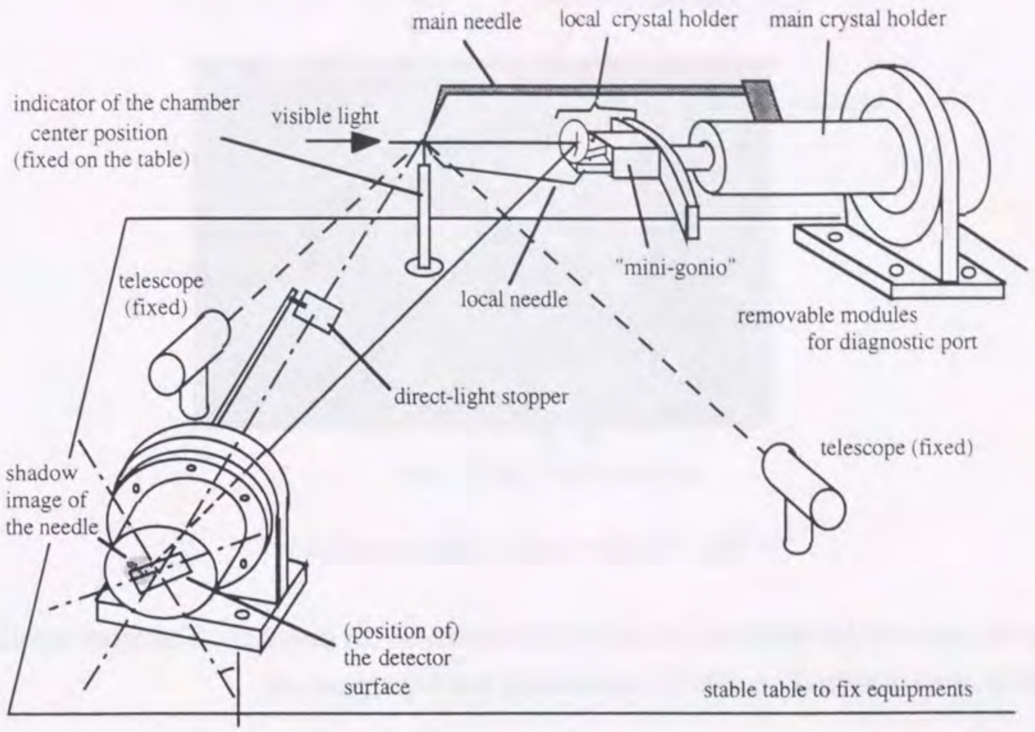

Fig. 11 Alignment outside the chamber

Putting the crystal-needle unit on the local crystal holder, one aligns the whole unit so as to place the top of the needle at the same point. For this purpose optical shadow image of the needle is taken at the position equivalent to the detector place. This step would be taken iteratively so that all images from every channels are located at proper position of the detection area. All the channels should be aligned in turn.

Finally, the "main needle" connected to the large crystal holder is aligned to the needle top at the object position. This main needle is necessary to memorize the relationship between the object position and the crystals.

III. installation to the target chamber

The large crystal holder has 3 freedoms of positioning with the precision of 30 μm (see Fig. 12). The crystals mounted on the large crystal holder are finally adjusted by

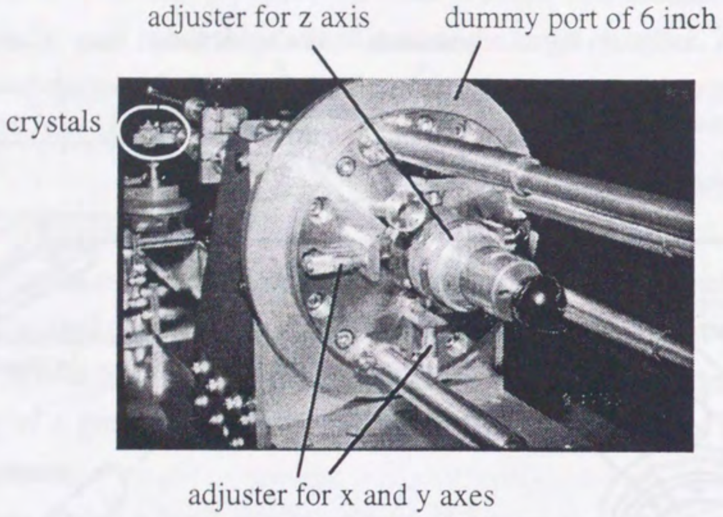

Fig. 12 Adjusters of the main crystal holder

using the main needle when the whole set is mounted on the chamber . Therefore the main needle is removable and capable of reproducing the target position.

Tools necessary for the crystal alignment

1. Goniometer including a lamp and optical telescopes (Fig. 9).
2. Alignment fixer (optical table, dummy flanges, target pointer, telescopes, alignment laser light, and optical lamp).